Automatic processing of induced seismicity at the geothermal reservoirs Landau and Insheim

Dissertation
zur Erlangung des Doktorgrades
der Mathematisch-Naturwissenschaftlichen Fakultät
der Christian-Albrechts-Universität zu Kiel

vorgelegt von
Kai Friedrich Martin Olbert

Kiel 2017

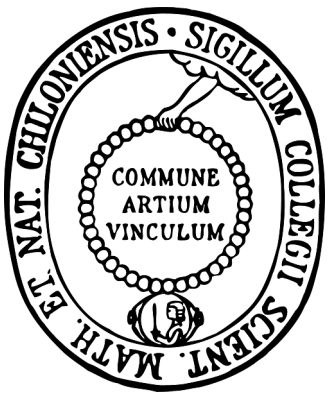

Referent: Prof. Dr. Thomas Meier
Korreferent: Prof. Dr. Wolfgang Rabbel

Tag der mündlichen Prüfung: 08. August 2017

Es ist eigentlich ganz einfach, sich einen Quadratmeter des Dimensionslochraums vorzustellen, vorausgesetzt, man hat mindestens sieben Gehirne:

Stellen Sie sich einfach einen Zug vor, der mit einer Kerze auf dem Dach durch ein schwarzes Loch fährt, während Sie selbst mit einer Kerze auf dem Kopf auf einem Glockenturm auf dem Mars stehend eine Uhr aufziehen, die genau einen Quadratmeter groß ist, und ein Uhu, der übrigens auch eine Kerze auf dem Kopf trägt, in entgegengesetzter Richtung zum Zug und mit Lichtgeschwindigkeit durch einen Tunnel fliegt, welcher gerade von einem anderen schwarzen Loch verschluckt wird, das ebenfalls eine Kerze auf dem Kopf trägt (sofern Sie sich ein schwarzes Loch mit einer Kerze auf dem Kopf vorstellen können, dazu benötigen Sie mindestens vier Gehirne). Verbinden Sie die vier Punkte, an denen die Kerzen brennen mit einem Buntstift, und Sie haben einen Quadratmeter des Dimensionslochraums.

Auf der Uhr können Sie übrigens nachsehen, wie spät es auf dem Mars ist, sogar im Dunkeln, denn Sie haben ja eine Kerze auf dem Kopf.

[Aus dem Lexikon der erklärungsbedürftigen Wunder, Daseinsformen und Phänomene Zamoniens und Umgebung von Prof. Dr. Abdul Nachtigaller]

Zusammenfassung

Obwohl die geothermiebasierte Energieerzeugung ein hohes Potenzial als erneuerbare Energiequelle besitzt, ist dieser Industriezweig in Deutschland noch nicht weit entwickelt. Neben politischer Unsicherheit und der Fündigkeit ist vor allem die induzierte Seismizität ein fundamentales Risiko für den Erfolg geothermischer Projekte. Die geothermischen Reservoire Landau und Insheim befinden sich im Oberrheingraben, wo die höchsten Reservoirtemperaturen in Deutschland gemessen werden. Allerdings bietet der Oberrheingraben mit seiner komplexen tektonischen Struktur auch eine Herausforderung als geophysikalisches Untersuchungsgebiet. Systematisches Prozessieren seismologischer Daten seit 2010 zeigt, dass an beiden Reservoiren nahezu kontinuierlich induzierte Ereignisse auftreten. Aufgrund des Mangels an komplementären geophysikalischen Studien ist eine Interpretation der induzierten Erdbeben problematisch.

In dieser Arbeit werden automatische Prozessiermethoden weiterentwickelt und angewendet mit dem Ziel, Charakteristiken der Seismizität in den Reservoiren zu identifizieren. Die Hauptziele liegen dabei auf dem Komplettieren existierender Erdbebenkataloge, die Zuverlässigkeit der automatischen Methoden zu evaluieren und Informationen über die auftretende Seismizität zu gewinnen, die in Zukunft mit Produktionsparameter der geothermischen Kraftwerke verknüpft werden können.

Um die Vollständigkeit der existierenden Erdbebenkataloge zu untersuchen, wird ein offline Ähnlichkeitsdetektor verwendet. Zu diesem Zweck werden mehrere Musterereignisse pro Reservoir ausgewählt. Der Algorithmus verwendet eine partiell normierte Kreuzkorrelationsfunktion, die schnelles Prozessieren möglich macht, auch wenn alle verfügbaren Daten berücksichtigt werden. 20/12 Erdbebengruppen (Cluster) mit 575/838 detektierten Ereignissen finden sich im Insheim/Landau Reservoir von 2007/2012 bis 2016. Im Vergleich zu den Erdbebenkatalogen (2010-2016) des Landeserdbebendienstes Rheinland-Pfalz und des Betreibers Bestec GmbH, 60 %/50 % der Katalogereignisse werden erneut detektiert, während 90/680 neue Ereignisse identifiziert werden. Aufgrund der hohen Anzahl an neu detektierten Ereignissen und der integrierten Clusteranalyse ist der Detektionsalgorithmus eine sinnvolle Methode zur Untersuchung induzierter Seismizität.

Des Weiteren wird ein Algorithmus basierend auf Autoregressiver Vorhersage (AR), dem Akaike-Information-Kriterium (AIC) und einer Kostenfunktion zum Bestimmen der Ankunftszeiten seismischer Wellen vorgestellt. Dieser Algorithmus bestimmt zuverlässig P- und S-Phasen Ankunftszeiten auf Einzel- sowie Mehrkomponentendaten. Die Parameter lassen sich für Datensätze auf unterschiedlichen Skalen einfach optimieren.

Zusätzlich wird eine automatische Qualitätskontrolle basierend auf Wellenformeigenschaften der Ankunftszeiten durchgeführt. Die Verteilungen der Residuen zwischen den automatisch und den manuell bestimmten Phasenankunftszeiten weisen niedrige Standardabweichungen auf: 0,49 s/ 4,36 s für Mantel - P/S-Phasen sowie 0,02-0,03 s/0,07-0,08 s für induzierte P/S-Phasen. Einsatzzeiten, die in unterschiedlichen Frequenzbändern bestimmt werden, bieten die Möglichkeit, frequenzabhängige Laufzeiten mittels des Algorithmus zu untersuchen.

Die automatisch bestimmten Phasenankunftszeiten werden verwendet, um ca. 400 induzierte Ereignisse des Insheim Reservoirs zu relokalisieren. Der Vergleich dieser Hypozentren zu Relokalisierungen mit manuellen Phasenankunftszeiten ergibt eine Offsetstandardabweichung von ca. 1 km horizontal und vertikal. Werden die manuellen Einsatzzeiten durch automatisch bestimmte ergänzt, verringert sich die Varianz der Hypozentren, während einzelne Ausreißer

auftreten. Daraus folgt, dass das zeiteffiziente automatische Bestimmen der Einsatzzeiten zuverlässige Lokalisierungen ergibt, während sich die Arbeitsbelastung der manuellen Prozessierer reduzieren lässt.

Anhand von Relativrelokalisierungen der Insheim-Ereignisse lässt sich eine räumliche Aufteilung der Cluster, die mittels des Ähnlichkeitsdetektors identifiziert wurden, erkennen. Ein Cluster, welches an der Produktionsbohrung lokalisiert ist, könnte ein Indikator für lokale Fluidkonzentrationen auf dem Weg zum Bohrloch sein, was zum Anstieg des Porendrucks und damit verbunden zum Auftreten von Erdbeben führt. Die geringen räumlichen Abstände zwischen den Clustern deuten auf variierende Mechanismen über geringe Distanzen hin. Anhand der Seismizität lassen sich zwei grobe Strukturrichtungen erkennen, die mit den ungefähren Richtungen der Spannungsregime übereinstimmen: eine Südost- zu Nordwest-Orientierung, die parallel zur Extensionsrichtung des Oberrheingrabens liegt und eine Süd- zu Nord-Orientierung, die dem jüngeren Spannungsregime der alpinen Hebung entspricht. Die zwei seismischen Orientierungen in dem Reservoir können sich kreuzende Verwerfungssysteme aufzeigen. Ein Vergleich der Stillstandszeiten des Insheim Kraftwerks mit dem Auftreten induzierter Ereignisse ergibt, dass das Reservoir zwischen 2 und 10 Tagen nach Produktionsstarts seismisch aktiv wird. Die Variation ergibt sich daraus, ob die Produktion zuvor kontrolliert heruntergefahren oder unbeabsichtigt spontan abgeschaltet wird.

Die Ergebnisse zeigen, dass die vorgestellten Prozessieralgorithmen wirksame und robuste Methoden sind, um Information aus induzierten seismischen Signalen aufzulösen. Die Interpretationen der seismischen Verteilung, der induzierten Mechanismen sowie der Reservoirgeometrie bilden eine Basis für zukünftige Analysen und für das Verständnis zukünftig auftretender Ereignisse und ergeben eine wissenschaftliche Grundlage zum Treffen von operativen Entscheidungen.

Abstract

Although geothermal heat energy production provides a large potential as substitute to fossil fuel resources, the industry is still at its beginning in Germany. Besides political and striking uncertainty, induced seismicity is a fundamental risk to the success of geothermal projects. The geothermal reservoirs Landau and Insheim are located on the western rim of the Upper Rhine Graben where the highest fluid temperatures in Germany provide a good foundation for geothermal energy production while the complex tectonic structure provides a difficult set-up for geophysical investigations. Systematic processing of seismic recordings since 2010 revealed continuously occurring seismicity at the geothermal reservoirs. Lacking complementary studies providing information on structures and reservoir characteristics makes the interpretation of the occurring events a challenging task.

In this thesis I advance automatic processing algorithms and apply them to assess characteristics of induced seismicity at the two geothermal reservoirs. Key objectives are to complete existing detection catalogs, determine the reliability of automatic processing results and to identify characteristics of induced earthquakes at the geothermal reservoirs which in future may be linked to operational parameters of the power plants.

Challenging the completeness of existing catalogs a complementary offline similarity detection approach which considers multiple master events per reservoir is proposed. It utilizes a partial normalization of the cross-correlation function, which enables fast processing, while still incorporating all available data. 20/12 event clusters are identified at the Insheim/Landau reservoir including 575/838 detected earthquakes from 2007 to 2016. Compared to the earthquake catalogs (2010-2016) by the state earthquake monitoring agency and the local monitoring company, 60%/50% of the catalogs are re-detected and in addition 90/680 new earthquakes are identified. Low number of false alarms, high numbers of additional detected earthquakes and the integrated cluster differentiation make it a useful tool to analyze induced seismicity.

The second algorithm is an autoregressive prediction (AR)-Akaike Information Criterion (AIC)-cost-function arrival time determination approach which is straightforward trainable for different datasets on different scales and able to reliably pick robust seismic P- and S-phase arrival times on single- and multi-component data. In addition, an automatic quality evaluation of arrival times based on waveform characteristics is performed. Comparison to manual reference datasets indicate low residuals standard deviations of 0.49 s/4.36 s for mantle P-/S-phase arrival times and 0.02-0.03 s/0.07-0.08 s for induced P-/S-phase arrival times. A comparison of different filtering frequency bands furthermore reveals a possible future application for frequency dependent travel time studies.

These determined automatic arrival times are applied to relocate about 400 induced earthquakes at the Insheim reservoir and the hypocenters are compared to relocations from manual arrival times. The resulting hypocenter offsets standard deviations are approximately 1 km horizontally as well as vertically. Complementing manually read arrival times with automatic picks provides lower hypocenter variance than using manual picks only, while accepting individual outliers. Thus, including automatically derived arrival times into routine processing increases time-efficiency, provides reliable locations while decreasing the manual processors workload.

Finally from hypocenter relative relocations, I am able to identify a spatial separation of the Insheim earthquake clusters retrieved by the similarity detection algorithm. An identified cluster at the production well of the Insheim reservoir may be an indicator for local back-logs of

fluids, leading to enhanced pore-pressure and earthquake nucleation. The identified low spatial separations of clusters between production and injection well in Insheim show that source mechanisms are differing over small distances. Two orientations of seismicity are found to coincide with the stress regimes, firstly a south-east to north-west orientation during graben activity, and secondly a rather south-to-north orientation of the recently more dominant stress regime from Alpine denudation. This likely indicates the existence of crossing faults in this area. Comparing detected seismicity to the offline times of the Insheim power plant, the reservoir response times between production start and the majority of earthquake nucleations amounts to 2 to 10 days. It is however noteworthy that the response times vary depending on whether the shut-down was controlled or sudden, i.e. an accidental shut-in.

Thus, results indicate that the automatic processing algorithms proposed here are valid, robust tools to increase the information gain from induced seismic signals. Interpretations of the seismicity distribution, induced mechanisms and the reservoir geometry provide a basis for analyzing and understanding future seismicity occurrences at the Insheim reservoir while providing a scientific foundation for decision making processes.

Contents

1. Introduction

1.1. Geothermal energy in Germany

The 21^{st} century is the age of changing global energy sources. Ever faster growing global population, vast pollution of oceans and countrysides, deforestation and global warming have become the major challenges for current and future generations. Global warming is triggered by the so-called greenhouse-effect, which describes the reflection of infrared radiation from the earth by trace gases in the atmosphere. Such gases are for example nitrous oxide (N_2O), methane (CH_4), carbon monoxide (CO) and the most popular carbon-dioxide (CO_2) (Lashof and Ahuja, 1990). Since CO_2 plays a big role (Matthews et al., 2009), global incentives (e.g. The Paris Agreement, Jayaraman and Kanitkar, 2016) aim to reduce anthropological sources of emission, e.g. fossil fuels for automotives or fossil fuel energy production.

However, besides reduction, capturing and storage of emitted CO_2 the development of substitute energy resources is a key quest for the success of such incentives. Furthermore, limited resources and highly variable supply stability of oil, gas and coal which are influenced by political conflicts, enhanced the search for alternative energy sources. Consequently, several renewable energy production schemes are becoming increasingly popular worldwide and especially in Germany. Following the Fukushima nuclear disaster and a public debate, an update to the German Federal government energy concept has been issued in 2011 (BMU/BMWi, 2011). This update includes the phase-out of all 22 nuclear power plants in Germany until 2022. Consequently, the pressure on renewable energy systems to replace well established energy resources is extreme.

The major renewable production sources in Germany are biofuels, wind energy and photovoltaic systems (Fig. 1.1 and 1.2). Deep geothermal energy production plays a minor role in the electrical as well as the heat sections for three reasons: 1. A tectonic setting for economical efficient production of deep geothermal energy exists only in restricted areas, 2. The geothermal exploitation in Germany is still at its beginning which means that the entrance risks (e.g. success of drilling, environmental risk, political risks) are high (Weber et al., 2015), 3. Induced seismicity in regions with low natural seismicity upsets local residents which intensifies the political risks (Rybach, 2003).

31 deep geothermal projects are currently operating with two additional power plants under construction (Federal Association Geothermal Energy, 2017). In total these account to a capacity of 303.36 Megawatt (MW) thermal and 36.9 MW electrical energy. Approximately the same number of projects are currently planned. Fig. 1.3 shows the global geothermal electric production

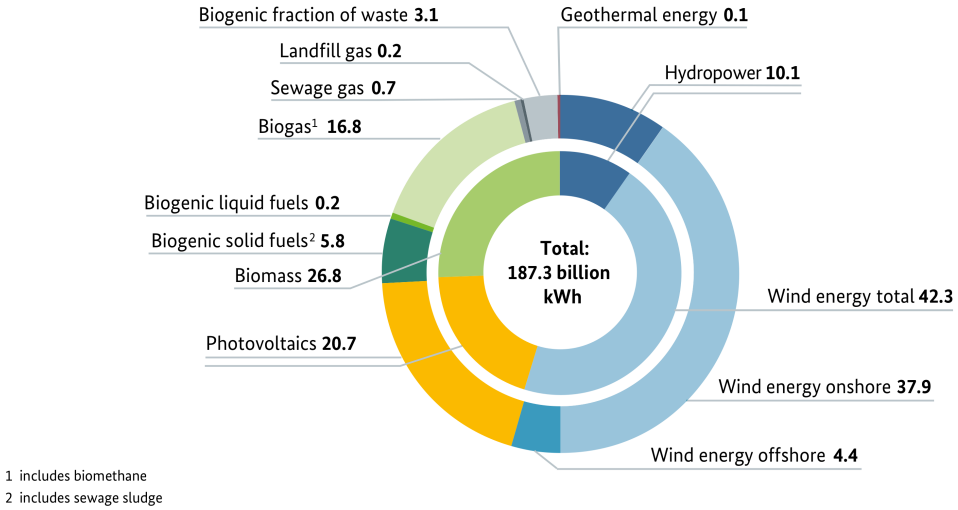

Figure 1.1.: Percentile share and absolute electrical energy generation in kWh from renewable energy sources in Germany in 2015. Reprinted from BMWi (2016).

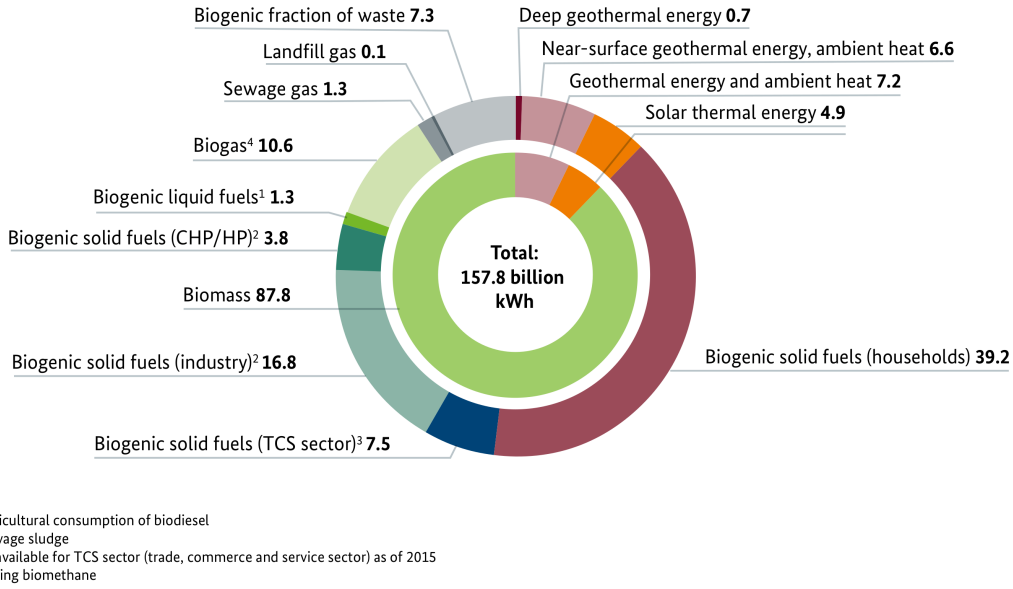

Figure 1.2.: Percentile share of renewables-based heat energy consumption in Germany in 2015. Reprinted from BMWi (2016).

capacity installed by 2015. In comparison to Germany (27 MW in 2015), countries with high subsurface temperatures, e.g. Iceland, Indonesia, Italy, Mexico, New Zealand, Philippines or the USA have more than 500 MW and up to 3.5 Gigawatt (GW) capacity installed (Bertani, 2016).

In Germany, three major regions provide the tectonic setting with either hot-water aquifers, deep-seated fault systems or crystalline rocks: the North German Basin approximately north of 52° N; the South German Molasse Basin around Munich towards west-south-west and the Upper Rhine Graben (URG) from Basel up to Frankfurt (Suchi et al., 2014). The URG provides the highest temperatures in crystalline rocks at depths around 3 km and is therefore of special

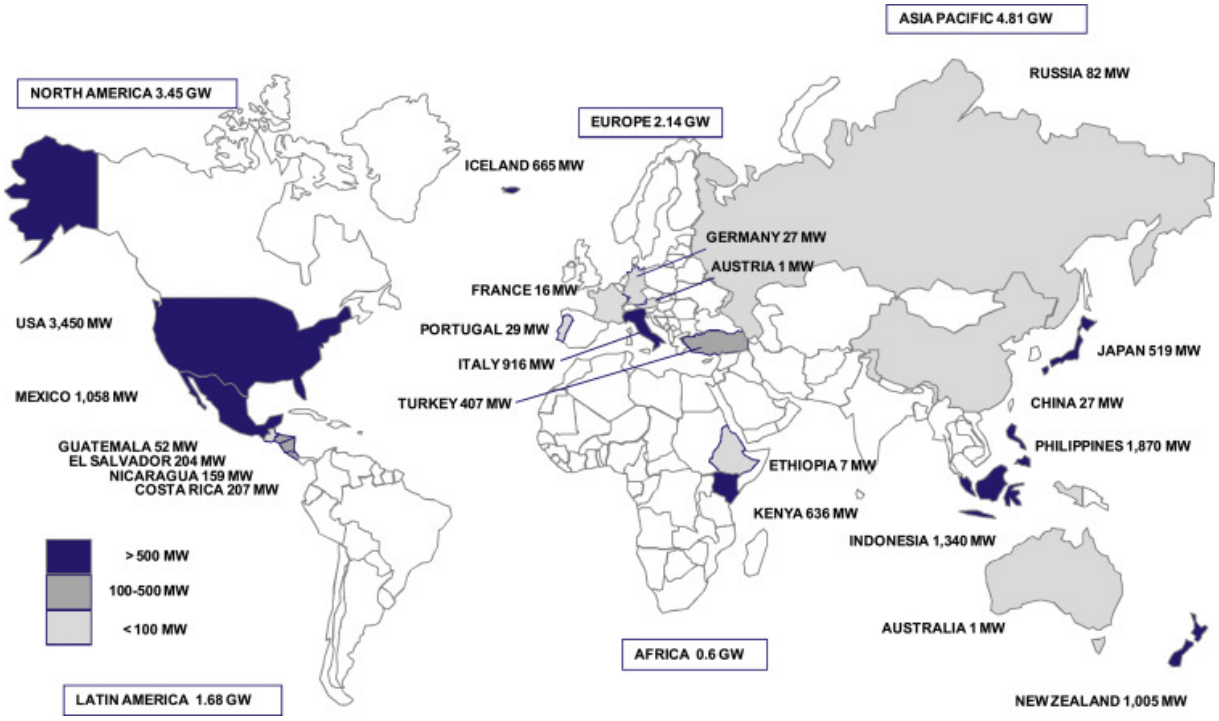

Figure 1.3.: Global map with installed geothermal electric production capacities per country by 2014. Reprinted from Bertani (2016).

interest for the future development of deep geothermal energy (Fig. 1.4).

Currently, two geothermal power plants are operated in the URG region. The older plant at the city of Landau is operating since 2007 and has been the first economically operating geothermal plant in Germany. Five kilometer south of Landau, close to the village Insheim, a second power plant started production in 2012. Fig. 1.5 shows the general concept of the Landau facility and energy production.

$155°C$ hot water is pumped up from depths between 2.5 and 3.3 km through the production well. At the surface a filtering system removes salts before the water flows through the first heat exchanger. The heated working media, Isopentan, is driving the turbine which generates up to 2.5 MW electrical energy. Before the Isopentan returns to the heat exchanger it is cooled down further circulating through a system of fans. The cooled down yet not cold water (about $70°C$) continues through a second heat exchanger. 8 MW heat energy are extracted and directly transferred to supply homes and factory facilities. Finally, the cooled down water is reinjected.

The Insheim power plant uses the same concept with wells reaching into deeper regions (up to 3.6 km) producing hotter water (up to $165°C$). In order to operate at higher production rates, its injection well has a side-track. Furthermore, since the transport of extracted heat energy at the surface is inefficient a heat transportation network with local consumers is required. Around Insheim neither a heat transport network exists nor sufficient consumers are available. Consequently, only 4.8 MW electric energy capacity is installed.

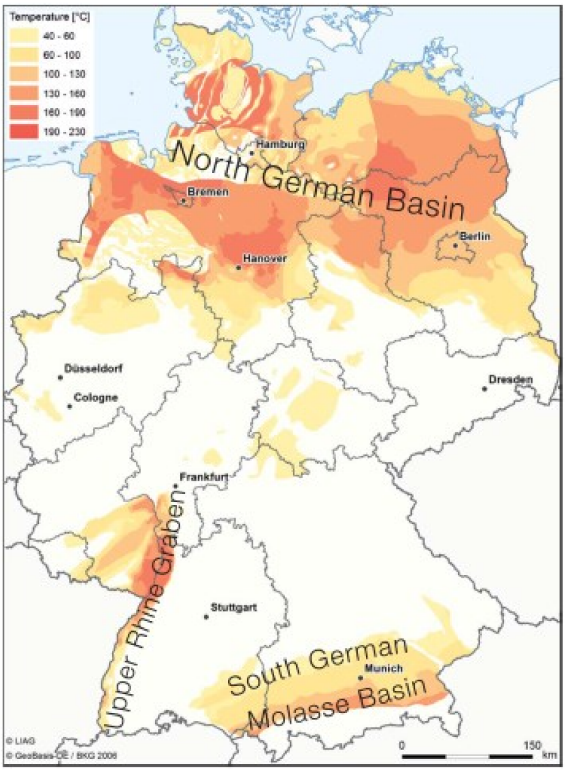

Figure 1.4.: Map of Germany with temperature ranges at the Upper Rotliegend sandstones aquifer in the North German Basin, at the Muschelkalk and Buntsandstein aquifers in the Upper Rhine Graben and the Malmkarst aquifer in the South German Molasse Basin. Reprinted from Suchi et al. (2014).

In comparison to major geothermal reservoirs in the USA (The Geysers Geothermal Complex: installed capacity 1,517 MW) or in Italy (Larderello Geothermal Complex: installed capacity 769 MW), the power plants in the Upper Rhine Graben are midgets. Nevertheless, since geothermal energy production in Germany is still at the very beginning, the Landau and Insheim projects have the potential to be role models for production in the URG and in Germany overall.

1.2. Upper Rhine Graben

The Upper Rhine Graben is a unique structure in Germany. It is part of the European Cenozoic rift system, which splits central western Europe from north to south. From the Northern Sea coast to the Rhenish Massif in western Germany extends the Ruhr Valley Graben (Illies and Greiner, 1979)/Lower Rhine Embayment (Prodehl et al., 1992)/Lower Rhine Graben (Schumacher, 2002). South of the Rhenish Massif towards the Franco-Swiss Jura (south-east) follows the Upper Rhine Graben (URG) which is connected to the Bresse Graben in East France by the Burgundy transfer zone. The Rhone Depression continues the graben structures from the area around Lyon towards the Mediterranean shore. Ziegler (1992) assigns furthermore the Golf of

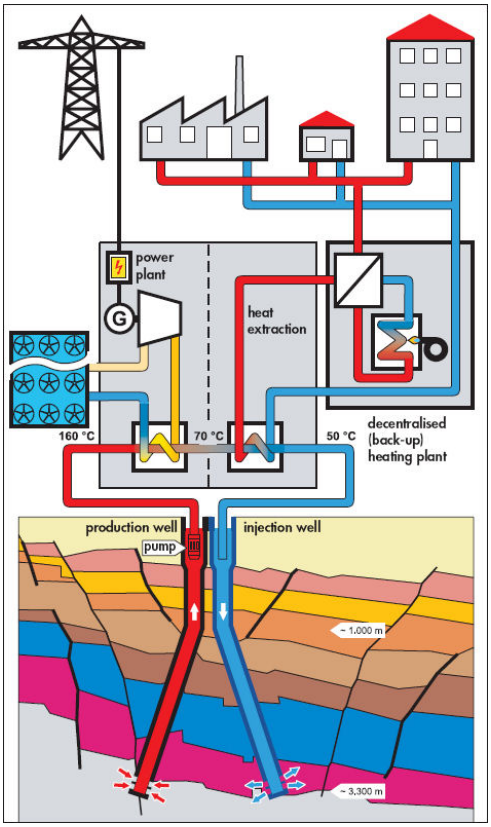

Figure 1.5.: Sketch of the general concept of the Landau power plant. Reprinted from geox GmbH (2016).

Lion and the Valencia Trough to this chain of graben structures.

Fig. 1.6 by Peters and van Balen (2007) shows the tectonic bodies of the URG, the sediment filling of Quaternary sediments and a sketch of a vertical cross-section including the position of the city of Landau.

The URG is a rift valley filled with Tertiary and Quaternary sediments extending approximately 40 km in the east-west and 300 km in the north-south direction. During the Late Cretaceous the compressional deformation of the Alpine and Pyrenees began due to the African-European continental collision. The orogenese changed the initial stress regime in the surrounding foreland (Illies and Greiner, 1978; Fuchs et al., 1987; Ziegler, 1992; Ziegler and Dèzes, 2006). While blocks of Hercynian basements reacted rigidly to the stress, tectonic extension in a ENE-WSW direction has been dominant in the Rhine Graben area during the Eocene to early Pliocene (Illies and Greiner, 1978; Larroque and Laurent, 1988). Thinning and subsidence of the crust in the rift valley and mass compensation from the lithosphere resulted in an E-W spreading of approximately 5-6 km (Villemin et al., 1986). The rifting process coincides with an updoming of the Lithosphere-Asthenosphere Boundary and Mohorovičić discontinuity as well as with volcanic activity in the north-western extension (Rhenish Massif, Illies and Greiner, 1978, 1979; Ziegler, 1992; Schumacher, 2002). The URG is a "passive rift" since the composition of volcanic

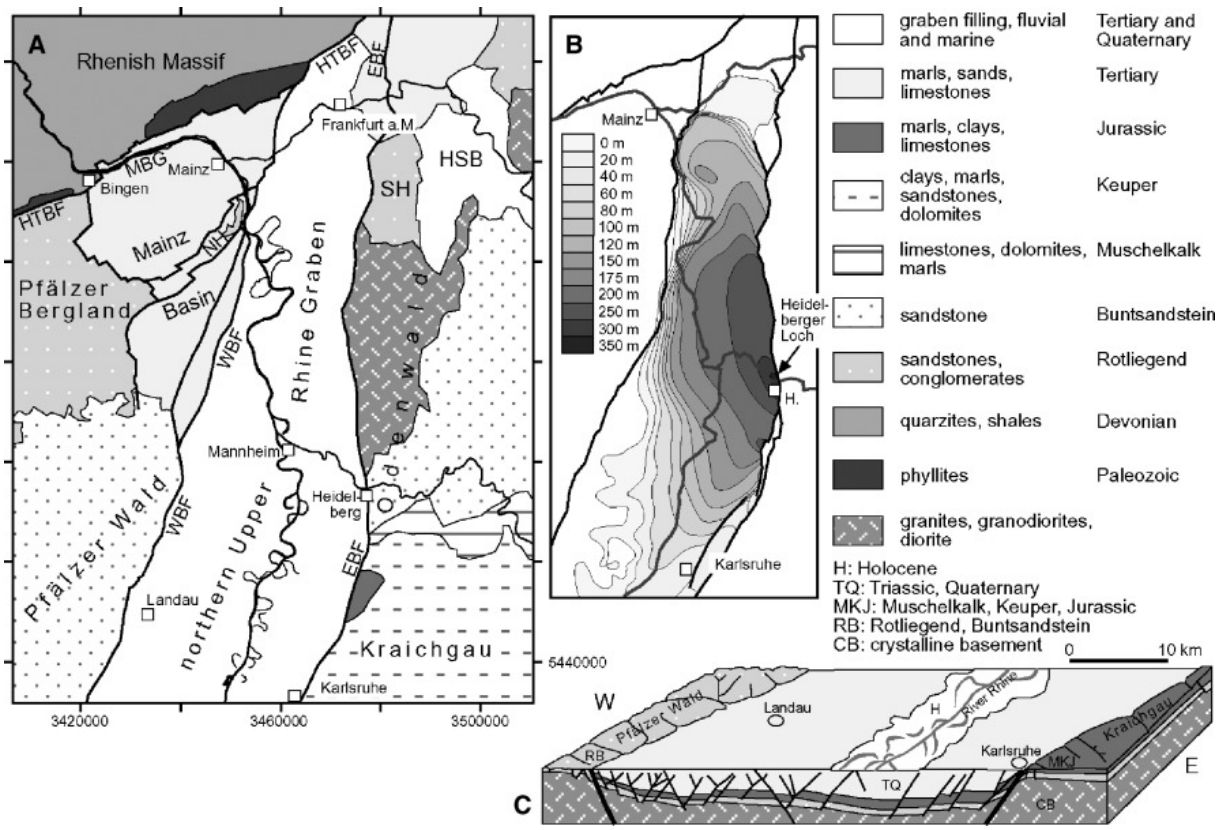

Figure 1.6.: A: Geological map of the northern Upper Rhine Graben and shoulder areas. EBF-Eastern Border Fault, HSB - Hanau-Seligenstadt Basin, HTBF - Hunsrück - Taunus Boundary Fault, MBG - Mainz Bingen Graben, NH - Niersteiner Horst, SH - Sprendlingen Horst, WBF - Western Border Fault. b: Distribution of Quaternary sediements in the northern Upper Rhine Graben with location of Heidelberger Loch . C: Simplified geological profiles across the northern Upper Rhine Graben. Reprinted from Peters and van Balen (2007).

deposits in the Rhenish Massif indicates a lower lithospheric/upper asthenospheric origin and seismic studies do not show any evidence for a plume originating from deeper mantle regions (Ziegler, 1992; Ziegler and Dèzes, 2006). On the eastern and western rims of the rift valley, shoulder formations are uplifted with today heights of several hundred meters on the western (Vosges/Palatinate Forest) and up to 1,500 m on the eastern side (Black Forest/Odenvald).

During the Miocene to early Pliocene, the rifting process slowed and the process of isostatic adjustment as well as denudation in the Alps led to a new stress regime. Furthermore, the retreating sea level resulted in an enhanced sedimentation during Pliocene and Quaternary (Illies and Greiner, 1978; Ziegler and Dèzes, 2006). Surrounded by consolidated Herkynian basements, the URG is a weak spot for tectonic stress relief. The north/north-east direction of the stress from Alpine denudation and uplift follows nearly the graben axis and therefore reactivated the former rift valley into a sinistral shear zone (Illies and Greiner, 1978). Depending on the segment orientations, compressional or extensional shear faulting is observed (Illies and Greiner, 1979). Besides the stress regime, the URG shows an exceptional temperature anomaly resulting from the thin crust. This feature and the shallow crystalline base rock makes it an ideal location for

geothermal energy production.

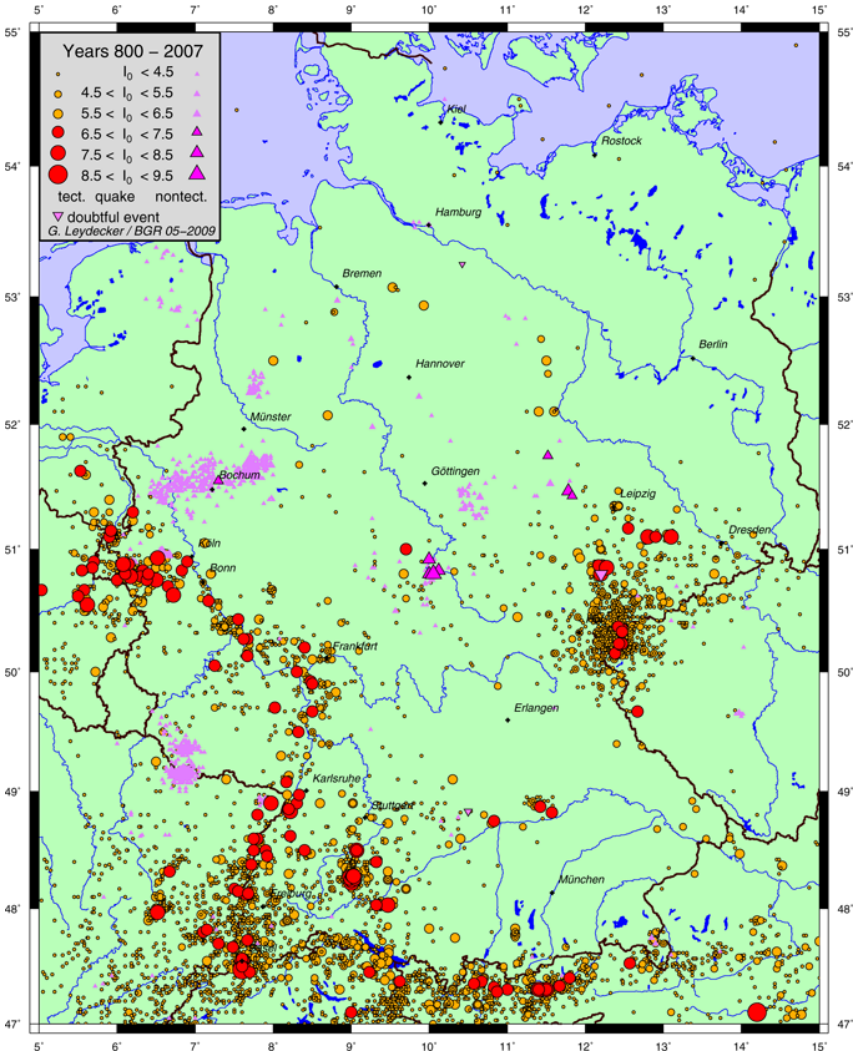

Figure 1.7.: Map of Germany with locations and intensity of tectonic and induced earthquakes determined from seismic recordings and historical sources. Reprinted from Leydecker (2011).

Tectonic seismicity is occurring along the German parts of the European Cenozoic Rift Zone (Fig. 1.7). Especially the southern URG (south of Karlsruhe to German-Swiss border) and the Lower Rhine Embayment (west of Cologne) are characterized by large earthquakes up to local magnitudes (Ml) of 6. Major events have been the historical earthquake in 1356 which destroyed Basel and more recently the Ml5.9 earthquake in Heinsberg in 1992 or the Ml5.7 earthquake in Albstadt in 1978. The region around Landau is located in a seismically less active area of the northern URG, where Homuth et al. (2014) detect only 56 earthquakes in the range from Ml0.5 to Ml3.2 between 2010 and 2013. Within the vicinity of Landau (<30 km) the latest tectonic earthquake in the region occurred close to the city of Speyer in October 2016 and had a magnitude of Ml1.6.

1.3. Induced seismicity in geothermal reservoirs

Compared to other regions where geothermal energy is produced, the seismicity rate in the URG is inferior. In Iceland, Turkey, Italy, New Zealand or the western USA earthquake magnitudes and seismicity rates exceed the URG by far. Consequently, the occurrence of induced seismicity in the URG is highly conspicuous whereas it nearly vanishes in the background seismicity of the other named regions.

The term induced earthquakes includes events which release anthropological induced stress as well as events which are artificially triggered but the released stress is of tectonic nature. Examples for induced seismicity are large underground explosions (Kisslinger, 1976), impoundment due to mass changes (e.g. large water reservoirs behind damps, extraction of fluids, Kisslinger, 1976; Segall and Fitzgerald, 1998), fluid injection (e.g. waste disposal, stimulation in geothermal or shale gas reservoirs, Kisslinger, 1976; Ellsworth, 2013; Grünthal, 2014; Zang et al., 2014) or opening of cavities for mining (Kisslinger, 1976).

Depending on the inducing mechanism, the event type and magnitudes differ as well as the acceptance of potential seismic risks for infrastructure and population. Although the potential for large magnitude events in geothermal reservoirs in central Europe is moderate, an on-going scientific and political debate endangers the success of geothermal power production (Grünthal, 2014).

Since different seismic behavior at different geothermal reservoirs have been monitored and studied thoroughly in the last decades, several triggering mechanisms are identified to be responsible for induced seismicity in geothermal reservoirs. The mechanisms differ depending on operational parameters as well as geological and tectonic settings:

- According to the classical stick-slip friction model, fault sliding is triggered if the ratio between shear and normal stress on the faults surface reaches the static friction coefficient (Scholz, 1998). During sliding the frictional resistance is reduced and may cause a dynamic instability resulting in the nucleation of an earthquake. Consequently, either the shear stress must be increased or the normal stress reduced to induce events. By injecting a fluid, the pore pressure is increased reducing the effective normal stress on faults in the reservoir. Depending on the reservoir rock, different reactions on injection are observed. In volcanic rock or sediments, the fluid injection leads to opening of stressed tensile cracks (Zang et al., 2014) whereas in crystalline reservoirs shear failure of existing faults are observed (Häring et al., 2008; Ellsworth, 2013; Zang et al., 2014).

- Extracting fluid or steam from a geothermal reservoir reduces the pore pressure which leads to a contraction of the reservoir rock. Since it is elastically coupled to the surrounding rock, the stress is transferred to the surrounding crust. As a results earthquakes which show a

dilatation source mechanism are induced as well as subsidence at the surface (Eberhart-Phillips and Oppenheimer, 1984).

- Extraction of fluids from a creeping fault system may lead to an increase of friction and the fault being locked. Such fault systems are found in tectonically active regions (e.g. San Andreas fault). Over time, the shear stress on the fault surface increases resulting ultimately in a stick-slip effect and the nucleation of earthquakes (Allis, 1982).

- The injection of cold fluids or the extraction of hot fluids lead to cooling of the reservoir rock and consequently induces thermoelastic stress. Although several studies suggest it to be a considerable effect causing microseismicity, none is able to verify or distinguish it as sole inducing mechanism (Allis, 1982; Segall and Fitzgerald, 1998).

The highest seismicity rates can be associated to the so-called stimulation of rocks with high-pressure injected fluids in EGS systems. During this stimulation phase a fluid is injected with increasing pressure over several days in order to open up cracks in the reservoir rock and hence increase its permeability. Well-studied cases with several thousands of microseismic earthquakes occurring during stimulation are the Basel EGS (Swiss, Häring et al., 2008; Bachmann et al., 2011, 2012; Cataldi et al., 2013), Soultz-sous-Forêtz (France, Grünthal, 2014; Zang et al., 2014) and The Geysers (USA, Allis, 1982; Eberhart-Phillips and Oppenheimer, 1984; Majer and Peterson, 2007; Zang et al., 2014). In opposition to these, stimulation injection over several days at the geothermal plant in Groß Schönebeck in Germany led to only 80 microseismic earthquakes with magnitudes smaller than Ml-1 (Moeck et al., 2009). The lack of seismicity in this example are likely caused by the much lower tectonic stress in the North German Basin as well as by the volcanic rock/sediment reservoir (Moeck et al., 2009; Zang et al., 2014).

At the Basel EGS the stimulation led to four events larger than magnitude Ml3 and finally to an end of the power plant project indicating how serious the issue of induced seismicity is for geothermal power plant projects in central Europe. However, the induced magnitudes in other exploitation sites (e.g. mining) exceed the ones observed at geothermal reservoirs. Furthermore, large b-values indicate that the probability of the occurrence of large events is smaller than for mining, fossil fuel exploitation or waste water disposal (Grünthal, 2014). Finally, in comparison to the large magnitudes observed at Basel (4 events with Ml$>$3 during stimulation), Soultz-sous-Forêtz (13 events with Mw$>$2 during stimulation) or The Geysers (up to Mw4.5 during stimulation and production) (Grünthal, 2014; Zang et al., 2014), the induced seismic energy release observed at Landau (2 events with Ml$>$2) and Insheim (1 event with Ml$>$1) is rather small.

Nevertheless, since a continuous local seismic monitoring has been set up in 2010 several hundred (Landau: $\approx 300 - 400$; Insheim: $\approx 600 - 700$) induced events have been detected (pers. comm.

Dr. L. Küperkoch, Bestec GmbH, Landau i.d. Pfalz, Germany). During production between 40 and 60 liter of fluids are pumped up and reinjected into the reservoirs per minute. After a leakage in the upper borehole-casing of the Landau injection well and displacement of surrounding terrain, the Landau power plant has been switched off in March 2014. The seismicity rate in the Landau reservoir has been declining since then showing only individual events. Since the characteristics of the induced seismicity at these plants have not been studied thoroughly, it remains unclear which mechanisms trigger these earthquakes.

Located on the eastern rim of the rift valley in the URG, Landau and Insheim are positioned at faults with an extensional shear stress regime (Peters and van Balen, 2007). Thus, normal fault source mechanisms with a sinistral shear tendency are expected if the induced seismicity occurs on major faults.

The monitoring of seismicity began in 2007 with a single three component surface station. After a Ml2.7 event at the Landau reservoir in 2009 the production rates at the Landau plant have been reduced (Bönnemann et al., 2010) and an injection sidetrack has been added to the later built Insheim plant. Following the incident a network of additional seismic stations by different agencies have been installed covering the region around Landau densely (about 50 stations). A systematic routine processing with detection and locations of induced seismicity has been carried out since 2010 (pers. comm. Dr. L. Küperkoch, Bestec GmbH, Landau i.d. Pfalz, Germany).

1.4. Automatic Processing of seismic recordings

Manual processing of seismic recording is time consuming and allows reliable learning about the seismic behavior only if performed continuously (Majer et al., 2007; Ellsworth, 2013). Since a monitoring network of seismic stations requires a significant financial investment geothermal plant operating companies do not prioritize the surveillance of seismicity for research applications. In order to study the phenomena of induced seismicity, however, a comprehensive database is fundamental. Every-day routine processing tasks, which are partially still carried out manually, make it difficult for monitoring companies to investigate characteristics of recorded induced seismicity further.

Consequently, automatic processing of induced seismicity offers several opportunities. On one hand, automatic processing is able to handle large amount of data and speed up the routine processing. On the other hand, it avoids inconsistencies due to subjective opinions of different manual processors (e.g. Diehl et al., 2009; Küperkoch et al., 2010, 2012). Routine processing steps are e.g. the detection of seismic events, the arrival time determination of seismic waves, the location of events from the arrival times or the magnitude determination.

Detection of seismicity provides the basis for any seismological studies and may be essential for

success of geothermal projects (Dahm et al., 2012). Since the seismic response of geothermal reservoirs can be modeled based on detection catalogs, the completeness of such catalogs is important. The performance of established algorithms depends on the tectonic set-up, quality of recordings and source-receiver geometry. While the well-established short-term-average to long-term-average detection algorithms are robust yet strongly quality dependent, similarity detection provides the opportunity to identify events in noisy data and furthermore resolve additional information of source location volumes.

The detection process is commonly assessed automatically yet sensitivity to noise and completeness of detection catalogs are still case dependent and vary with different approaches. On the contrary, phase arrival time determination is still a problem which is solved by time-consuming manual processing (Küperkoch et al., 2012). Regional and time dependent noise patterns and ever changing seismic signals make the automatic arrival time picking a huge challenge which has not sufficiently been solved yet. Since the seismic phase arrival times are used to determine hypocenter locations it is of fundamental interest how automatically determined arrival times influence location results.

1.5. Scientific key questions and strategy in this thesis

This thesis combines the issue of automatic processing with the so-far sparsely analyzed induced seismicity at the geothermal reservoirs at Landau and Insheim. As indicated in the previous chapters, induced seismicity poses a significant threat for geothermal energy production (e.g. Basel EGS, Bachmann et al., 2011; Grünthal, 2014). At the same time, geothermal energy production has large potential since it is independent of quickly alternating environmental factors like the wind or the solar radiation. Hence, to retain the opportunity of geothermal energy production to play a role in the age of alternative energy sources in Germany, a thorough understanding of inducing and triggering earthquake mechanisms is essential and can be achieved by consistent monitoring and analyzing of induced seismicity on site.

In order to comprehend the local microseismicity occurrences at Landau and Insheim, the processing of seismic data is performed using automatic methods. The scientific key questions of this thesis are:

- Are existing catalogs complete or can additional earthquakes be detected?
- Are the induced earthquakes at the geothermal reservoirs Landau and Insheim occurring in groups (clusters) and what are characteristics of the clusters?
- Can automatic arrival time picking achieve comparable precision to manual time readings?
- How reliable are hypocenter locations from automatically determined arrival times? Can these be considered for routine processing?

- What information on the Insheim reservoir can be derived from re-processed induced seismicity?
- How does the Insheim reservoir respond to the injection of fluids.

In order to complement existing event catalogs and to get a primary picture of the Insheim and Landau reservoirs seismic characteristics, a similarity detection algorithm is applied on continuous seismic recordings.

In the second step, the issue of automatic arrival time determination is discussed. An algorithm to determine reliable arrival times from waveform recordings is proposed. To verify its general applicability, its performance on teleseismic P- and S-waveforms as well as the database of induced seismicity at Landau and Insheim is discussed. Furthermore, automatically determined arrival times are considered in a re-location process with the objective to test the consistency and robustness against manual processing results. To get a better resolved picture of the reservoirs seismicity, relative relocations are calculated in addition.

Finally, the results of detections and locations are combined to interpret the seismic response of the geothermal reservoir Insheim, including which mechanisms may be triggering the nucleation of induced earthquakes.

2. Offline similarity detection of induced seismic events

2.1. Introduction

2.1.1. Motivation

One essential aspect for the success of geothermal projects is a near-complete detection catalog of microseismicity (Dahm et al., 2012). These catalogs are needed to gain general knowledge of the seismicity and magnitude occurrences and the evaluation of seismic hazards. Furthermore an observation of fluid migration, and stress changes is important for the purpose of reservoir modeling.

Since induced seismicity at geothermal power plants reached the level of public as well as political awareness, reliable real-time detection and magnitude determination is essential for a well informed communication with publicity and decision-making. Operating companies depend on established methods so that neither the processing itself nor the results can be challenged, allowing for a trustworthy foundation for a dialogue between stakeholders.

Observing and modeling seismic behavior need to be complementary tasks. In the case of a geothermal energy project this means on the one hand observing the reservoir behavior and seismic responses to operating parameters, e.g. injection pressure, and on the other hand training model parameters on recent observations and evaluating modeling results on posterior data (e.g. Bachmann et al., 2011; Cataldi et al., 2016). Such models are able to describe the fluid flow, stresses induced by fracture propagation (e.g. Wassing et al., 2014), stress-earthquake interaction (Cataldi et al., 2016), friction evolution (McClure, 2012), frequency-magnitude distributions and consequently seismic hazards (e.g. Eberhart-Phillips and Oppenheimer, 1984; Bachmann et al., 2011; Király et al., 2015) or combined thermal-hydraulic-mechanical (THM) parameters (e.g. Jeanne et al., 2014; Rutqvist et al., 2015b,a).

The most crucial models for the success of geothermal energy production in Germany might be the seismic hazard models. Several studies suggest so-called traffic-light systems to analyze detected events. Based on frequency-magnitude distribution and either statistical or hydro-mechanical approaches, future seismicity and the risk of continuing production are ranked following traffic-light colors. Since the Basel EGS is one of the most fateful cases of induced seismicity in geothermal reservoirs, several studies discuss the advantage of different methods on this example (e.g. Bommer et al., 2006; Deichmann and Giardini, 2009; Bachmann et al., 2011). With a dense

network of seismic stations including several borehole sensors (>1000 m), induced seismicity of this reservoir have been observed with a magnitude of completeness $M_c = 0.6$ (Bachmann et al., 2011). The Basel reservoir is an excellent test ground for these systems because it is well monitored. Nevertheless, it is insufficient to rely on individual test grounds to obtain robust systems for monitoring and assessing risks since seismicity is strongly related to the geologic and tectonic backgrounds.

In this study, we focus on seismicity at the Landau and Insheim geothermal reservoirs in Germany. The monitoring situation around these reservoirs is less comfortable and possibly only presents incomplete detection catalogs. There are only 3 borehole stations compared to Basel, which are positioned in shallow wells (<500 m) and thus have a lower signal-to-noise ratio (SNR) than the Basel borehole seismometers. Nevertheless, for monitoring and interpretation of seismicity, as well as for the hazard assessment and decision-making, well-established detection algorithms and as complete as possible catalogs are important. Is a similar approach as the one in Basel still applicable to this region? Or how does the detection incompleteness influences the modeling results?

A recent and in the context of induced seismicity in Landau and Insheim highly relevant study is the similarity detection algorithm proposed by Vasterling et al. (2016). The algorithm is applied to detect induced seismicity of the geothermal reservoirs Landau, Insheim as well as to identify quarry blasts in the region. Furthermore it assigns the detected events to these three source regions. It performs well, achieving a completeness-magnitude of 0.0 (MAGS-Magnitude) for approximately 500 microseismic events, four erroneous detections of local tectonic events and no wrong assignment of events among the three source regions. Furthermore, it has been implemented into the SeisComp3 software and is used by the local earthquake monitoring service Rheinland-Pfalz (LER). The company Bestec GmbH, which operates the local monitoring network has been applying a real-time STA/LTA algorithm to detect induced seismicity (pers. comm. Dr. L. Küperkoch, Bestec GmbH, Landau i.d. Pfalz, Germany).

Both detection approaches are optimized to provide real-time or near to real-time earthquake detections. Therefore, a quick processing of data is required while the amount of considered data must be limited. Similarity based detection algorithms like the MAGS-detector by (Vasterling et al., 2016) are less sensitive to noise than STA/LTA approaches. However, the cross-correlation in a moving-time window is inefficient and thus only a selected number of stations (≤ 7) are included in the detection process. A noisy environment like the agricultural area around Landau may then result in the incomplete earthquake catalogs. Furthermore, similarity detection provides insights into the reservoir seismicity. Applying the cross-correlation on the envelope of waveform data (Vasterling et al., 2016) may smooth waveform characteristics and thus neglect a part of the similarity information in the data. Whereas (Vasterling et al., 2016) only differentiate between events of the two reservoirs, in this study we aim to distinguish individual earthquake clusters inside each reservoir. For these reasons, a complementary detection approach is selected.

In the following, I will give an introduction to detection algorithms and similarity analysis of seismicity, followed by the presentation of an derived offline detection algorithm based on waveform similarity. Its application is consequentially evaluated using the dataset of induced seismicity at Landau and Insheim and compared to the catalogs obtained by the real-time STA/LTA- as well as the MAGS-detector by (Vasterling et al., 2016).

2.1.2. Similarity analysis and detection

Applying similarity analysis methods to investigate seismicity distributions, aftershock sequences as well as swarm and multiple events has become a common seismological analyzing practice (Aster and Scott, 1993). These methods enable knowledge gain on source information: e.g the source-time function, rupture characteristics, high-precision relative locations (e.g. Aster and Scott, 1993; Augliera et al., 1995; Hemmann et al., 2003; Baisch et al., 2008; Wehling-Benatelli et al., 2013); as well as structural information: e.g. from multi-source and -receiver processing or scales of heterogeneity at source regions (Nakahara, 2004; Gibbons and Ringdal, 2006).

In general, similarity analysis in seismology refers to the correlation of either waveform data or transformations of waveforms at one (auto-correlation) or multiple stations (cross-correlation). Transformations can be any sort of characterizing functions, e.g. the envelope (e.g. Vasterling et al., 2016) or the power spectra (e.g. Joswig, 1990) of seismic recordings. Multiple studies have been undertaken to determine reliable relative travel times of phase arrivals and apply these to retrieve high precision relative locations of events (Geller and Mueller, 1980; Ito, 1990; Augliera et al., 1995; Maurer and Deichmann, 1995; Hemmann et al., 2003; Nakahara, 2004; Gibbons and Ringdal, 2006; Baisch et al., 2008). While this might be the most frequent application of similarity analysis, detecting known patterns within continuous data has also been an application during the early development stages of this methodology (Anstey, 1966).

Relative location and similarity detection are based on the assumption that similar earthquake waveforms are caused by similar source mechanisms as well as similar propagation pathways of the seismic waves. If hypocenters of two or more earthquakes are in immediate vicinity to each other it is likely that the source mechanism is of the same orientation. Furthermore, the propagation pathways from the center of these events to a station are assumed to be nearly identical, resulting in nearly identical Green's functions and hence highly similar waveforms. If the seismicity is restricted to distinct zones within a seismic active region, the similarity detection approach can be used to detect events showing similar waveforms to known earthquakes as well as distinguish between earthquakes belonging to different distinct zones. In the following the most common detection approaches will be shortly introduced and discussed.

The most widely known/used detection approach, short-term-average to long-term-average algorithms (STA/LTA) calculate average values of recorded data or its transformations over a short and a long time window. If the short-term-average exceeds the long-term average by a certain

threshold, a seismic phase arrival and hence an event detection is declared. STA/LTA algorithms have proven to be quick and robust for the detection of seismic phases in recorded data (e.g. Allen, 1978; Baer and Kradolfer, 1987). However, they are sensitive to erroneous detections due to noise bursts, and moreover they are insensitive to earthquake waveforms hidden by low SNRs.

Another approach, the Walsh detector, calculates a Walsh transform of the waveform which results in a set of rectangular functions sorted by frequency ranging from -1 to +1. The Walsh coefficient can be used to identify a signal within Gaussian noise (e.g. Goforth and Herrin, 1981). Since these approaches do not require complex calculations, they can be applied to any dataset with only few parameters (e.g. threshold) to be set. However, the Walsh detector is similarly insensitive to signals accompanied by strong noise amplitudes.

Joswig (1990) introduces a detection algorithm using sonogram pattern recognition. Signal as well as noise related patterns are compared to sonograms of data and a detection is triggered if signal patterns and data sonograms are similar. This means a characteristic amplitude distribution in the time-frequency plane is used to detect events. It is similar to the method by (Vasterling et al., 2016), however the amplitude information in various frequency bands is evaluated separately. Applied to an example dataset it performs well in comparison to common STA/LTA and Walsh detection algorithms reducing the number of false alarms and missed events significantly.

Using pattern recognition, even small magnitude events, hidden in noise, can be detected by cross-correlating waveforms of known events (master events) with continuous seismic recordings (Israelsson, 1990; Harris, 1991; Gibbons et al., 2012). Master event waveforms are station specific recordings cut around the relevant earthquake signals. Such similarity detection approaches to microseismicity were applied e.g. by Maurer and Deichmann (1995) and more recently by Gibbons and Ringdal (2006).

Maurer and Deichmann (1995) calculate the similarity detection on seismic earthquake waveforms in the Alps. They define master events by selecting earthquakes from catalogs with the restriction that these have minimum epicenter distances of 100 km. P- and S-wave signals are individually correlated and the sum of all correlation values provide the network similarity of different events. P-waves tend to provide a higher similarity than S-waveforms, which prove to be more complicated. They identified 150 clusters of at least two similar events with correlation values higher than 0.8. 600 out of 1,500 known events are identified and assigned to these clusters. By relocating events, they use the similarity analysis as an independent measure of hypocenter location precision.

Gibbons and Ringdal (2006) use an array-stacked cross-correlation detector to increase sensitivity and detect a small aftershock of the 1997 Kara Sea earthquake as well as induced seismic events on Spitsbergen over 2,000 km distances. They apply array processing to combine individual correlation traces and increase the SNR. They find that detection sensitivity of a single stream

similarity approach is lower by an order of 0.7 magnitudes, compared to what the STA/LTA array approach is able to detect. For their long-distance case study they introduce a frequency-wavenumber analysis to reduce false alarms.

It has been shown that similarity analysis is strongly dependent on parameter choices such as time window length and filtering. Major conclusions have been the decrease of correlation with increasing window lengths and with filter bands including higher frequencies (Augliera et al., 1995; Nakahara, 2004; Baisch et al., 2008). Concerning the impact of spatial separation between events, different case studies in different regions show heterogeneous results from which a strong dependency on case geometries and local geology and tectonics can be concluded (Aster and Scott, 1993; Augliera et al., 1995; Hemmann et al., 2003; Nakahara, 2004)).

The similarity detection algorithm by Vasterling et al. (2016) evaluates waveform similarities at each station individually. They calculate the envelope of three component data and perform a cross-correlation of these with envelopes of master reference waveforms. The envelope has the advantage of smoothing the waveform, which reduces high frequency differences between event waveforms and therefore results in larger similarity values. Detections are declared if at 70% of the considered stations the similarity threshold is exceeded. Nevertheless, the magnitude of completeness $M_c = 0.0$ is given as MAGS magnitude which underrates events by half a magnitude compared to local magnitudes (Ml).

Taking advantage of the methods and learning of the methods described above an offline detection algorithm similar to Gibbons and Ringdal (2006) is presented. The basic idea of this approach is to provide a complementary tool to existing event catalogs from similarity as well as STA/LTA detection algorithms.

The greatest drawback of the similarity detection methods is the requirement of a priori knowledge about multiple recorded events and locations, which are representative for seismicity in a region. Furthermore, only earthquakes or seismic events actually similar to the master events are detected. The approach by (Vasterling et al., 2016) reduces this restriction since the envelope has the advantage of smoothing the waveform, which increases the overall correlation values. However, the low number of stations included make it insensitive to detections if local noise amplitude increases while the potential to differentiate earthquake groups, so-called clusters, in the individual reservoirs is neglected and clustering within the reservoirs can not be detected.

By calculating the cross-correlation using as many data as available a lower sensitivity to noise variations is expected. Furthermore, using the waveform directly instead of the envelope a stricter differentiation between event similarities is likely. Thus individual clusters in the reservoirs should be more distinct.

Similar to (Gibbons and Ringdal, 2006), stacking of correlation functions of individual events

aims to improve the SNR. In order to differentiate, including P- as well as S-waves is useful to identify events with low hypocenter separations (Maurer and Deichmann, 1995). For a continuous monitoring application the algorithm is supposed to improve the catalog completeness besides sorting detected events into clusters. The algorithm approach is introduced in the following section before testing the sensitivity of envelope cross-correlation against waveform cross-correlation. Finally, the algorithm is applied to the Landau and Insheim datasets.

2.2. Similarity detection algorithm

2.2.1. Similarity detection algorithm

Many similarity analysis approaches have been applied in seismological studies ranging from detection and location to timing-accuracy. Key objectives of the proposed detection algorithms are:

- Maintaining sensitivity in a low SNR environment.
- Managing large amounts of seismic data.
- Differentiating clusters within the geothermal reservoirs.

In order to increase the methods sensitivity to low magnitudes, in this study data of all available stations should be considered, which consequently, requires a fast processing approach. These two requirements already address two of the above mentioned objectives for detection algorithms. In the framework of the MAGS (Microseismic Activity in Geothermal Systems) project and its follow-up MAGS2, the amount of seismic stations deployed around Landau and Insheim increased significantly to 50 stations recording simultaneously, in 2014 - 2016. The large amounts of data advises against the normalized cross-correlation approach calculated in a moving time window, since it is quite time consuming.

The third point requires the usage of multiple master events per reservoir to identify the respective clusters. Thus, recorded and cataloged seismicity has to be reviewed in order to identify possible master events, which show varying waveforms. For this purpose, a similarity analysis is applied.

In a following step, the algorithm must be able to calculate the similarity between current data and all master events simultaneously and assigns detections to the respective clusters. Calculating the cross-correlation of the envelopes of waveforms and continuous recordings has been successful in the MAGS-detector (Vasterling et al., 2016) increasing the similarity between events. Fig. 2.1 shows the similarity calculated using the envelope of 43 induced events located at the Insheim reservoir (pers. comm. Dr. L. Küperkoch, Bestec GmbH, Landau, Germany). The hypocenters are distributed over the whole reservoir volume and range over the whole production time (2012-2016) and magnitude range (Ml0.7 - Ml2.1). The cross-correlation has been calculated for a single station's recordings (STS1) and both P- as well as S-phase are included in the correlation. Overall, high similarities among all event waveforms are observed, excluding the last two events.

Fig. 2.2 shows in comparison the similarity matrix of the same events calculated by cross-correlating the waveforms directly. The overall similarity among the events is lower while the clusters of similar events stand out more distinct.

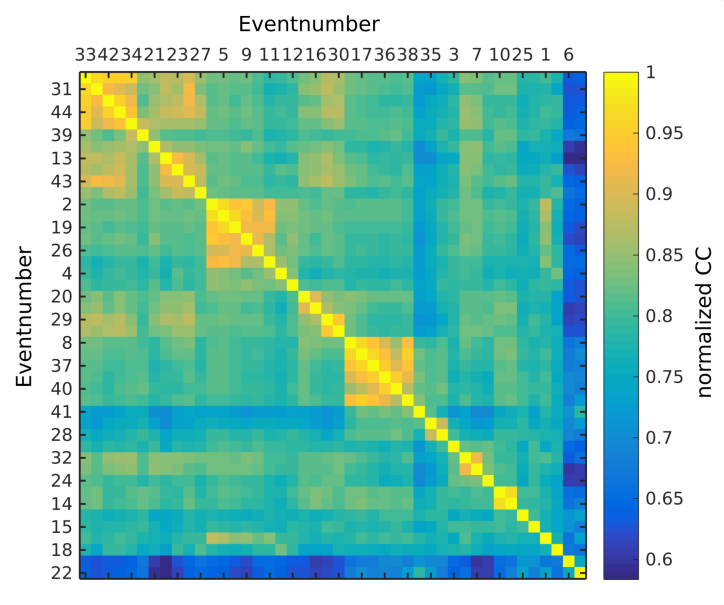

Figure 2.1.: Similarity matrix showing cross-correlation indices (cc) of 43 characteristic induced earthquakes at the Insheim reservoir. The events differ in locations, magnitudes and source times. The cc is calculated using the envelopes of three component data, including P- and S-wave arrivals, recorded at the borehole station STS1. Top left event has cumulative maximum correlation and additional events are sorted by maximum correlation to the one above.

For the two events which show low similarity in both, waveform and envelope correlation, waveform signals vanish in background noise at station STS1. In general, the cross-correlation indices using the waveform are still high with cc>0.5. A distinction between groups of similar events becomes more apparent using the waveform correlation method. Consequently, while applying the envelope correlation appears reasonable in order to derive complete detection lists, the waveform offers the possibility to differentiate clusters. Moreover, the lower sensitivity between dissimilar events, provides the possibility to reduce the detection threshold. Consequently, the waveform detection algorithm is considered the better choice for this explicit application, although, it requires well-recorded and detected master waveforms for each cluster.

In the following, the detection algorithm is described and applied exemplary on a single day recording before the master event selection process for Insheim and Landau is discussed.

The algorithm described here is a complementary offline approach in addition to real-time detection algorithms and aims to complete catalogs and do a cluster analysis. The algorithm consists of four major steps: cross-correlating master event waveforms with continuous data of all channels individually, stacking and normalizing the correlations to a detection function, preliminary detections at times where the detection function exceeds a threshold, verifying preliminary detections by recalculating the normalized cross-correlation between master and detected waveforms.

Fig. 2.3 shows continuous three component waveform data, bandpass filtered between 1 and 30

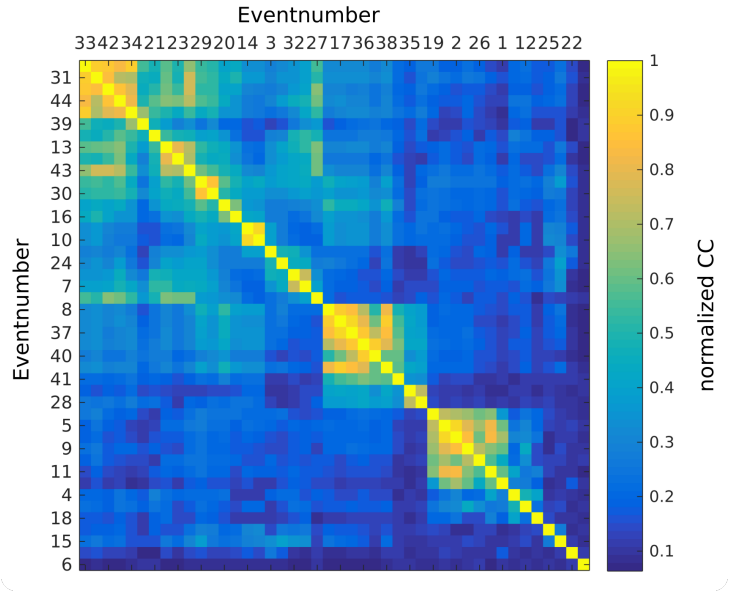

Figure 2.2.: Similarity matrix showing cross-correlation indices (cc) of 43 characteristic induced earthquakes at the Insheim reservoir. The events differ in locations, magnitudes and source times. The cc is calculated using the three component waveform data, including P- and S-wave arrivals, recorded at the borehole station STS1. Top left event has cumulative maximum correlation and additional events are sorted by maximum correlation to the one above.

Hz, recorded on October 2^{nd} 2013. Three detections are shown in cut out windows of which the first one is the strongest event (Ml2.1) recorded at the Insheim reservoir so far and the third shows a noise burst. To visualize the detection process, the slightly weaker (Ml1.3) second event at 01:43am is selected as master event and applied to the same day in the detection process.

Most similarity detection approaches calculate the normalized cross-correlation over two equally long signal segments (e.g. Joswig, 1990; Gibbons and Ringdal, 2006; Vasterling et al., 2016)). This requires a moving time window which is time consuming. In order to pursuit a more time efficient approach, instead of normalizing the cross-correlation by both, the energy in the continuous recording and the energy in the master event data, it is normalized only by the energy in the master event data. Thus, instead of processing short time windows of data sequentially, long data sequences of continuous data can be processed at once according to:

$$r(t_k) = \frac{1}{\sum_{j=1}^{S} w_j} \left[\sum_{j=1}^{S} w_j \frac{1}{\sum_{c=1}^{M} m_c} \left| \sum_{c=1}^{M} m_c \frac{\sum_{i=1}^{N} y_{jc}(t_i) \cdot x_{jc}(t_{i-k})}{\sum_{i=1}^{l_m} (x_{jc}(t_i))^2} \right| \right], \tag{2.1}$$

where $r(t_k)$ is the correlation function and $x_{jc}(t_i)$ and $y_{jc}(t_i)$ are the master waveform and the continuous data on component c at station j. As the result of the normalization with the master event energy only, the correlation amplitude does not indicate the waveform similarity in the range between zero and one, but is defined by the waveform similarity and the relation be-

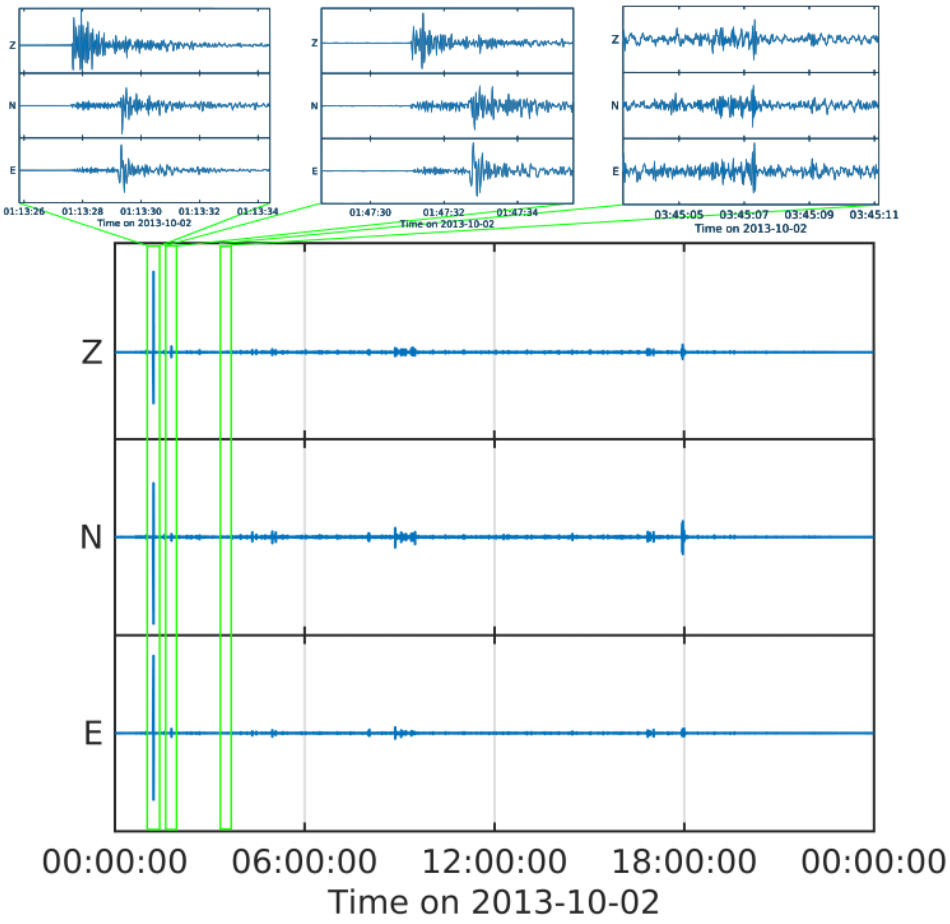

Figure 2.3.: Three component waveform data (bandpass filtered 1-30 Hz) of station SOS6 recorded on October 2^{nd} 2013. Enlarged windows show induced Insheim events Ml2.1 at 01:13am, Ml1.3 at 01:47am and noise burst at 03:45.

tween master waveform amplitude and continuous data amplitude. As a consequence, if a high magnitude master event is selected, the correlation value of very low magnitude earthquakes is underestimated due to the amplitude ratio much smaller than one. On the contrary, assuming that the waveform of a master and detected event are identical the resulting correlation value $r(t_k)$ is the ratio of the master and detection waveform amplitudes and consequently can be used to estimate the magnitude similar to Gibbons and Ringdal (2006). The quick estimation of magnitudes is a big advantage of this correlation approach, especially since no preceding hypocenter location is required. However, the waveforms are never identical and thus a magnitude correction term must be introduced.

The utilization of multiple stations' data is reasonable since a better data coverage should provide the best detection rate. Weighting the impact of individual stations or components is useful to enhance or reduce the influence of special waveform characteristics, e.g. strong distinct S-waveforms or noisy/distant stations, to improve detection sensitivity. Thus, including multiple stations, master waveforms of length l_m are correlated with continuous data of length N for M components at S stations resulting in a single correlation function. w_j and m_c are used as

weights of individual stations j and components c. Since the source time of the master event is selected as reference time for each master waveform x_{jc}, a detection time t_k should coincide with the approximate source time of the detected event.

The correlation function can still be calculated using the envelope, derivative of the envelope or the waveform. However, a full review of these different methods is not part of this study.

The calculation is fast, yet two aspects must be considered. A moving-time window approach requires a continuous recalculation of the cross-correlation which is the time-consuming part of the processing. Calculating it only once avoids the usage of loops in the numerical implementation and thus is much faster considering multiple stations and a dataset of at least a day.

Fig. 2.4 shows the cross-correlation of three component waveform data of station SOS6 with the selected master event. Several peaks of high correlation values are visible, three coinciding with the approximate event times as well as with noise bursts. Asymmetric correlation indicates the correlation of the master event with noise bursts on the N-component.

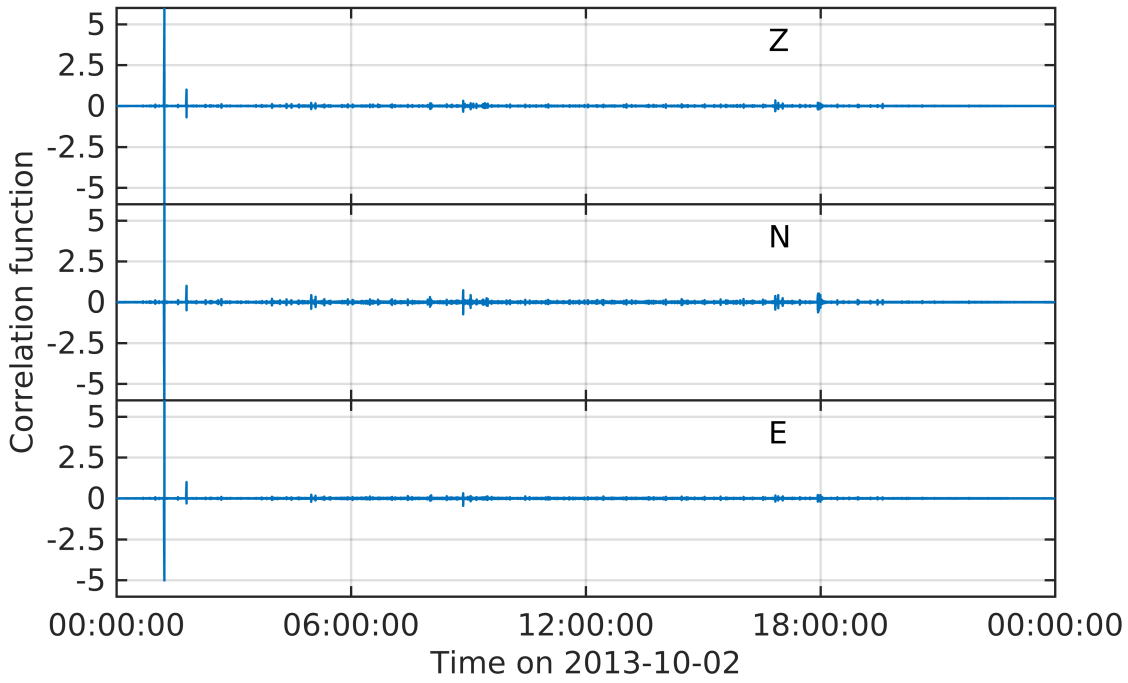

Figure 2.4.: Correlation of three component day waveform data on 2^{nd} October 2013 of station SOS6 with master event waveform from Ml1.3 2^{nd} October 2013, 01:47 event showing minor amplitude increase during day and amplitude peaks around first two known detections.

Gibbons and Ringdal (2006) apply similarity detection on both single station and arrays of stations pointing out that using a f-k-stacking approach on an array can reduce the detection sensitivity by half a magnitude. Considering this, the correlation functions of different stations

are added up using the component and station weighting. Fig. 2.5 shows the stacked correlation functions including 3, 9, 12 and 15 stations on October 2^{nd} 2013. A reduction of the overall correlation amplitude is not observed while individual noise peaks, including the noise burst around 3:45am, decrease the more stations are included.

Considering the event characterizing importance of $t_S - t_P$-times, the vertical and horizontal components are weighted equally. To detect low magnitude events, stations are inversely weighted with epicenter distances to the master event.

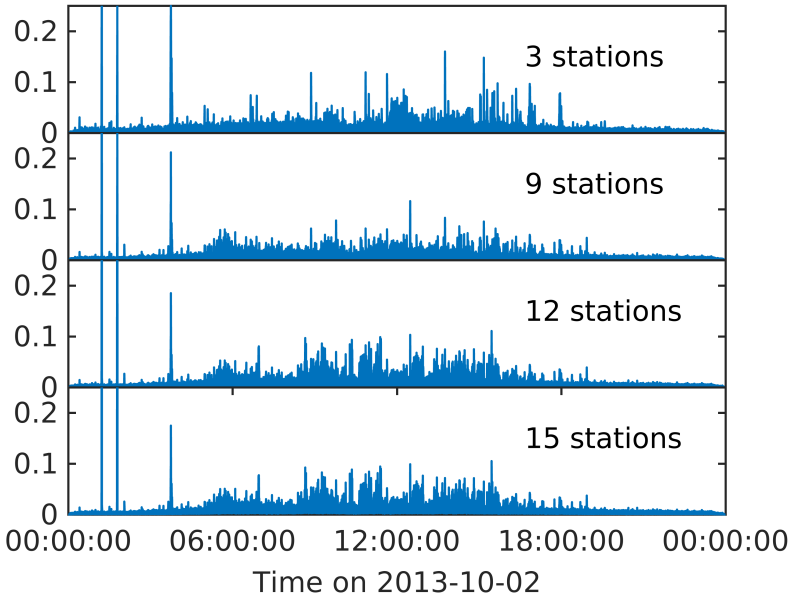

Figure 2.5.: Weighted stacked correlation functions of October 2^{nd} 2013 including 3, 9, 12 and 15 stations. The overall daytime noise amplitude is remains constant while noise peaks are reduced in amplitude due to stacking.

The increase of noise during daytime and its consequential higher correlation amplitude must be considered for selecting detection thresholds. Instead of choosing a dynamic threshold, the correlation function is normalized with a noise level resulting in the detection function $D(t_k)$:

$$D(t_k) = \frac{r(t_k)}{[\frac{1}{2l_n} \sum_{i=k-l_n}^{k+l_n} r(t_i)]}, \tag{2.2}$$

with l_n as half the window length in which the noise level is determined. It is calculated recursively as mean value over the window length $2 \cdot l_n$ (here 100 s) around each sample of the correlation function. Fig. 2.6 a) shows the correlation function and the corresponding noise level (green), which has a similar amplitude rise during daytime. Contrary, the resulting detection function in Fig. 2.6 b) is lacking this diurnal variation indicating that the normalization works.

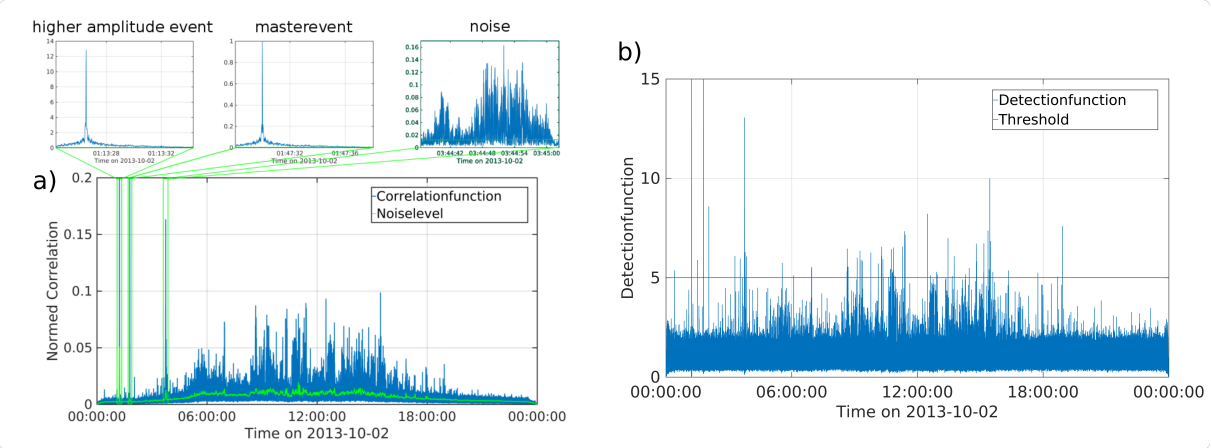

Figure 2.6.: a) Correlation function of 17 stations and corresponding noise level (green) calculated as mean correlation over a 100 s moving time window. Three cut-outs show the correlation function around the master event (01:47am) itself, a Ml2.1 Insheim event (1:13am) and a noise burst (03:45am). b) Detection function calculated as correlation function normalized by noise level and detection threshold (red) above which a preliminary detection is declared.

Both events show strong and similar correlation patterns with strong main peaks. Much lower peaks, which still exceed the noise level, are distributed over the whole day. The threshold level is set rather low at a value of 5 to avoid missing a possibly unknown low amplitude event. Exceeding a detection function value of 15, both known events stand out from the much lower noise detection values.

In order to remove noise events, e.g. strong noise peaks, from the detections a post-processing using normalized cross-correlation is proposed. After determining preliminary detections during the day using the unnormalized cross-correlation, in this second step the amplitude dependency is removed.

In this post-processing, the normalized cross-correlation master event and detection waveforms cut out around the initial detection times is calculated according to:

$$cc = MAX_j \left[\frac{1}{M} \sum_{c=1}^{M} \frac{\sum_{i=1}^{n} z_{jc}(t_i) \cdot x_{jc}(t_{i-k})}{\sqrt{\sum_{i=1}^{l_m} (z_{jc}(t_i))^2} \sqrt{\sum_{i=1}^{l_m} (x_{jc}(t_i))^2}} \right], \tag{2.3}$$

where z_{jc} is the detection waveform at station j on component c and has the same length as the master waveform x_{jc}. Thus, if the averaged cross-correlation indices cc at a single station exceeds the post-processing threshold the detection is confirmed.

Applying a threshold of $cc > 0.5$ the preliminary detections are reduced to two remaining: the largest Insheim event at 01:13 am and the master event itself at 01:47am. These events show highly similar waveforms on all stations included in the detection process (Fig. 2.7). Only sta-

tion INS3 shows a noise pattern preceding the P-phase waveform which is not apparent in the detected waveform.

These high waveform similarities indicate that both events can be assigned to one cluster of events whose hypocenters are expected to be in close proximity to each other. As a result, the existence of event clusters sharing source regions and source mechanism among the induced events at the Insheim reservoir is already shown and only the extent of the clustering is unknown.

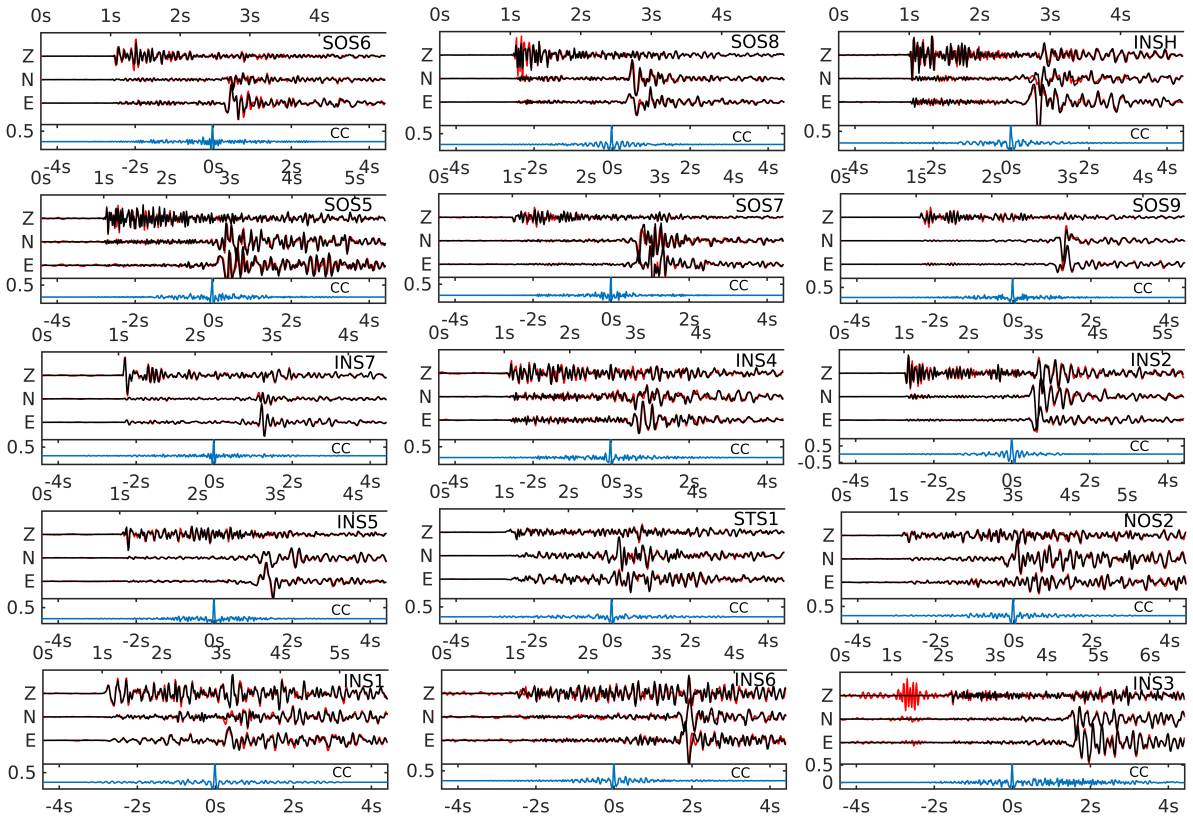

Figure 2.7.: Three component waveforms (Z,N,E) of the detected Ml2.1 Insheim event at 01:13am (black) and master event waveforms (red) at 15 stations which are included in the detection process. The data is 1 to 30 Hz bandpass filtered. Below each waveform plot, the cross-correlation function cc between detection and master event at each stations is displayed. The time on the x-axis is given in seconds.

2.2.2. Station weighting

After introducing the detection process and its usage of as many stations as possible, in this section the role of station weighting is discussed. According to equation 2.1 both stations and components can be individually weighted. In the case of microseismicity with low magnitudes, a distance dependent weighting scheme is proposed.

Fig. 2.8 shows the relative positions of stations to the Insheim event on May 20^{th} 2015. Most

stations are positioned within 1 to 5 km around the master events epicenter. With increasing distance the signal amplitudes are expected to decrease due to scattering and damping.

The resulting weighting function is shown in Fig. 2.9 for the station distribution in Fig. 2.8. Nearby stations, where better SNR is expected, are weighted much higher in order to enhance the detection sensitivity of even low magnitude events.

The weighting function has been empirically tested against linear curves as well as for different steepnesses. It is applied for all master events, while the stations relative position on the curve is recalculated for each master event individually.

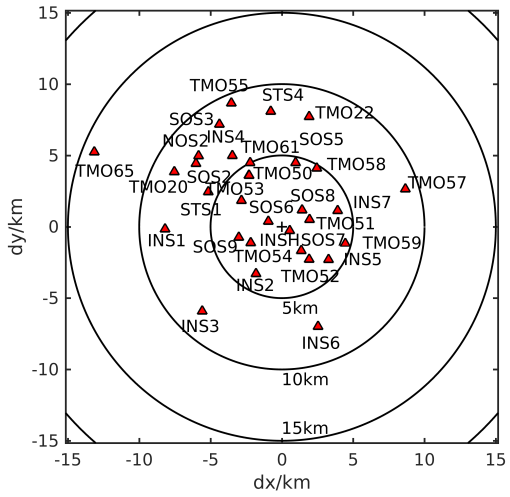

Figure 2.8.: Relative locations of seismic stations to the epicenter of an Insheim event on May 20^{th} 2015.

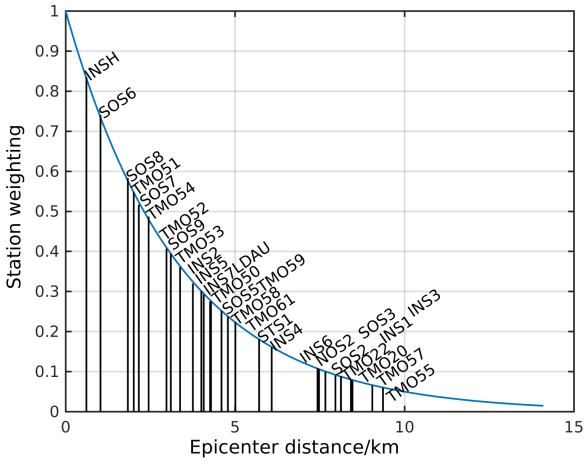

Figure 2.9.: Station-distance weighting function and stations weighting for Insheim event on May 20^{th} 2015.

The detection algorithm has been introduced, pointing out its ability to search through big datasets and applying multiple different master events. As pointed out, the envelope is useful to achieve a good level of completeness while the waveform is able to differentiate between clusters of seismicity. A distance dependent station weighting scheme is provided to deal with low magnitude microseismic events and hence low SNRs. Stations closest to the epicenter of the master events are given the highest weights whereas the lowest weights are assigned to the stations farthest away. In the following chapter the database of continuous recordings is presented followed by a discussion of the algorithms application on the complete database.

2.3. Database

In the region around Landau and Insheim the recording of continuous data evolved since the start up of the Landau geothermal project in 2007. Station SOS2 has been installed by the monitoring company Bestec/Geo-X GmbH in the same year. Although up to 50 stations have been recording simultaneously since then, the availability of data is partly restricted. Fig. 2.10 shows the number of station channels in the region around Landau for which data is available between 2007 and 2016. The available station data is retrieved from the GEOFON data center via Arclink or provided by Bestec/GEO-X GmbH and varies between 1 to 20 stations. After the Ml2.7 Landau event in 2009, additional stations were installed by Bestec/GEO-X GmbH, Deutsche MontanTechnologie GmbH (DMT GmbH) and the local earthquake monitoring agency (LER). However, the DMT stations are recording only if triggered and therefore do not provide continuous data streams. Within the first MAGS-project from 2010 till 2013, the Karlsruhe Institute of Technology (KIT), the Bundesanstalt für Geowissenschaften und Rohstoffe (BGR) and the LER added several stations in the region, adding up to approximately 20 three-component stations in a 15 km - radius surrounding the plants at Landau and Insheim. Within the MAGS2 project the station density has further increased by the BGR and LER setting up additional stations. The amount of data in the continuous data only slightly decreases in 2014, when the Landau power plant was sold including some of the monitoring stations.

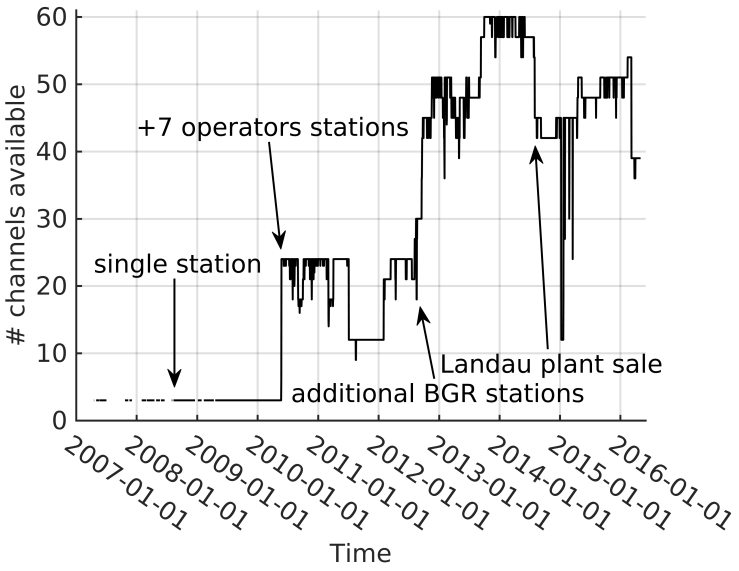

Figure 2.10.: Availability of channel data of up to 20 stations around Landau from 2007 to mid 2016 including Bestec/GEO-X stations and BGR MAGS-network stations.

Fig. 2.11 shows the stations' locations in the vicinity of Landau and Insheim including roads and urban areas. The distance between the plants and inhabited areas affects the SNR of seismic stations in the area. In addition, low magnitude events leave only close-by stations to use. The close vicinity around the power plants are well covered while only few stations are located further east as well as to the west of Insheim.

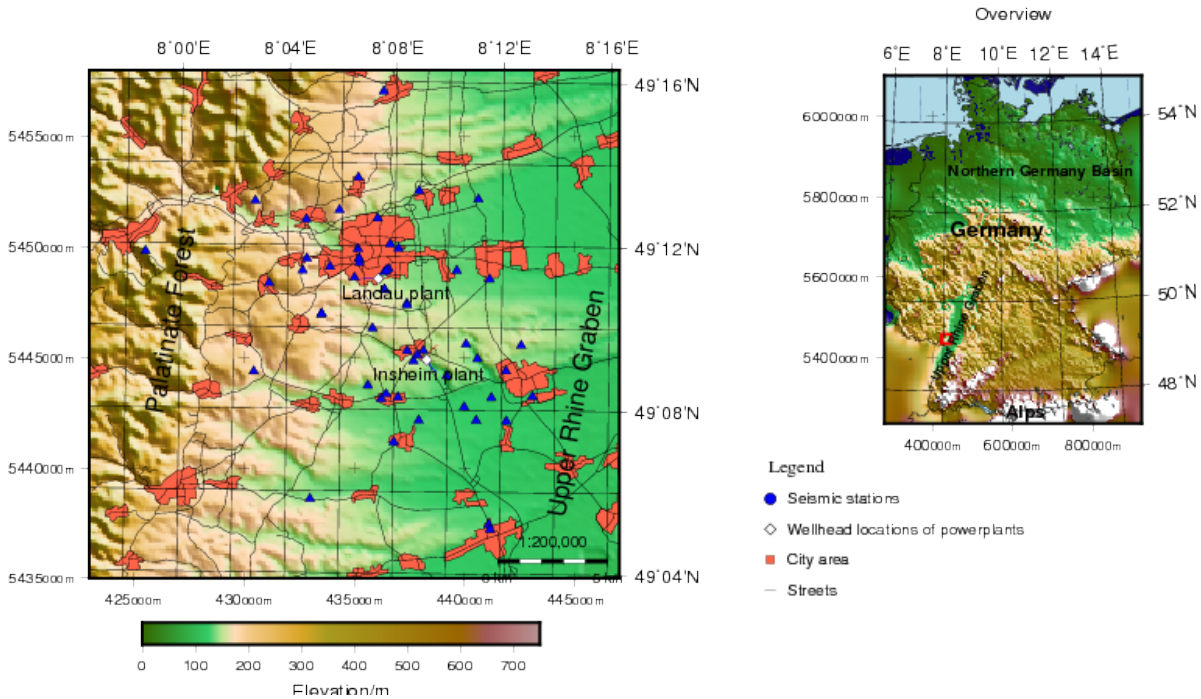

Figure 2.11.: Map of seismic stations, geothermal power plant locations, urban areas and topography in the surrounding area of Landau with UTM32s and WGS84 coordinates.

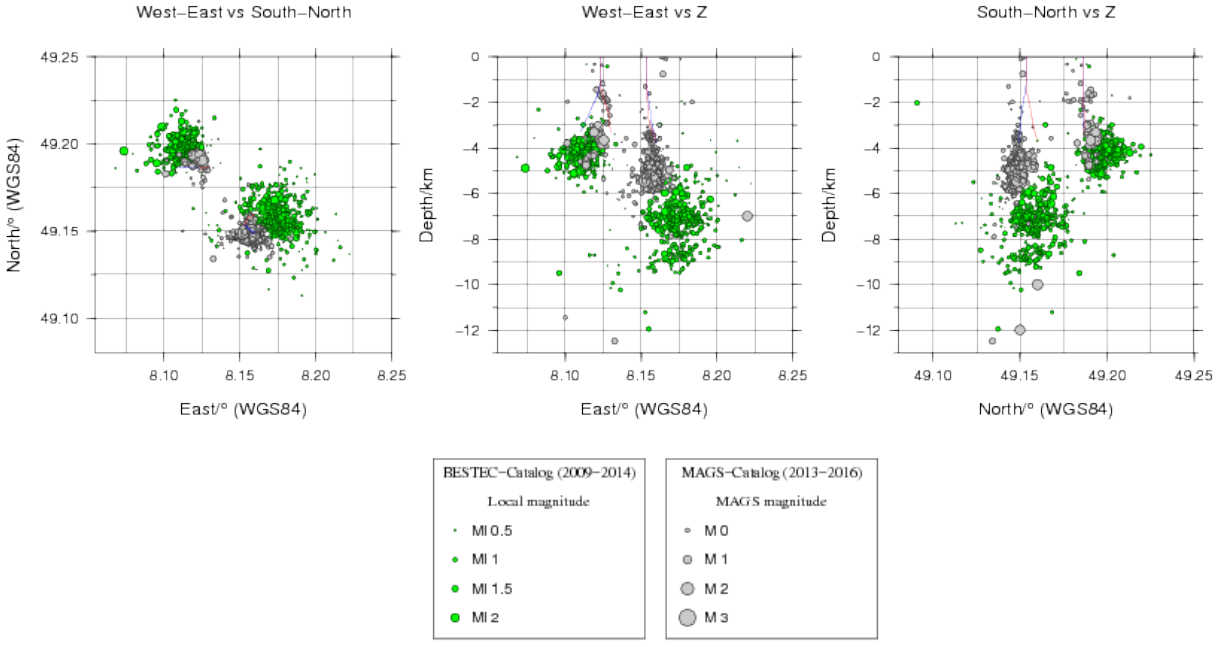

Figure 2.12.: Maps of induced earthquake hypocenter locations taken from MAGS (gray) and Bestec (green) catalogs in top-, south- and east view. Red and blue lines indicate the production and injection wells of the Landau and Insheim power plant.

To improve the processing speed of the detection algorithm the data sampled between 100 and 400 Hz are all consistently re-sampled to 100 Hz. A third order butterworth bandpass filter

from 1 to 30 Hz is applied before the correlation. The filter setting corresponds to the routine processing filter. As references, the catalogs of the monitoring company Bestec GmbH as well as the LER are used. These are referred to as Bestec- and MAGS-catalogs hereafter. Fig. 2.12 shows the locations and magnitudes of induced events at the Landau and Insheim reservoirs taken from the MAGS (gray) and Bestec (green) catalogs. Bestec runs a real-time STA/LTA algorithm on up to 9 stations. The LER applies the MAGS-similarity detector included in the SeisComp3-software (Vasterling et al., 2016). Differences between the locations and determined magnitudes are observed. The MAGS locations are concentrated within a smaller volume. Reasons for the discrepancy are different processing parameters, different magnitude definitions and different time spans covered by each catalog.

2.4. Results

In this section the application of the offline-detector introduced above is described in detail. Preceding the application, the master event selection process and the master events are presented. Finally, the determined event detections of recordings from 2007 to 2016 for both geothermal reservoirs, Landau and Insheim, are discussed.

2.4.1. Master events

In order to differentiate earthquake clusters of several locations, source mechanism and magnitudes within the geothermal reservoirs, master events with typical representative waveforms must be selected. An iterative approach is selected for finding appropriate master earthquakes.

Following the similarity analysis in Fig. 2.2 an initial selection of 8 master events is found for the Insheim reservoir and applied in the detection process. When a major induced earthquake, listed in one of the catalogs, is not detected by any applied master event, it is considered to represent a new cluster and thus defined as new master event. For the Landau reservoir an initial selection of 5 earthquakes with dissimilar waveforms is found and iteratively increased. Finally, 20 independent master events are defined for the Insheim reservoir and 12 independent master events for the Landau reservoir. Locations and magnitudes as given in the Bestec catalog are shown in Fig. 2.13. A full list of locations, source time and magnitudes of all selected master events is given in Appendix A.

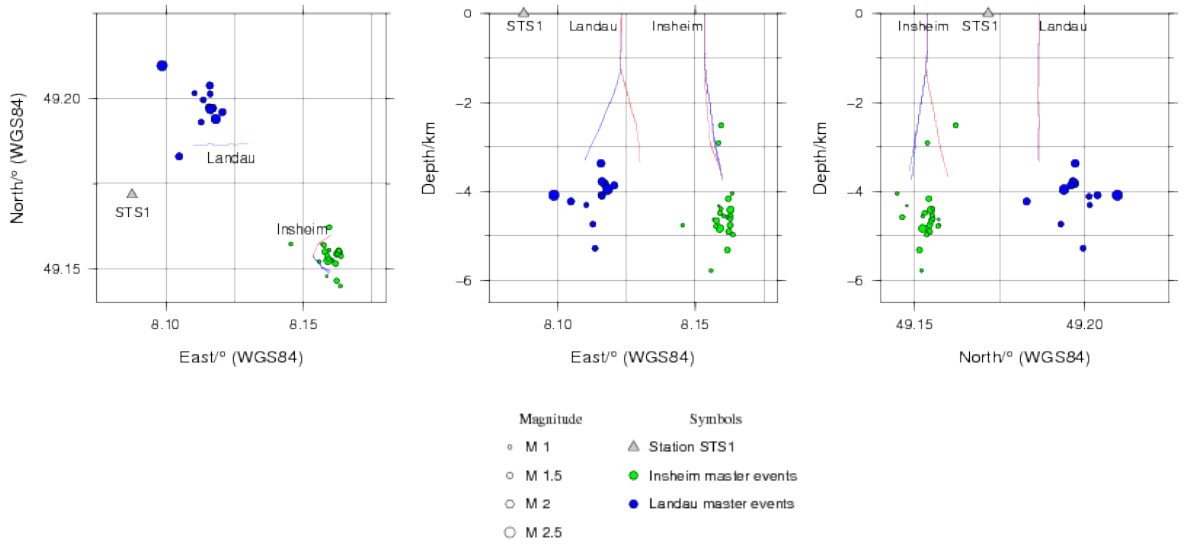

Figure 2.13.: Bestec catalog locations and magnitudes (Ml) of selected master events for Insheim and Landau reservoir. Production (red) and injection (blue) wells of the Landau and Insheim power plants as well as location of the seismic borehole station STS1.

Figs. 2.14 and 2.15 show the similarity matrices calculated on three component data at the seismic

borehole station STS1. Each column-line combination of the matrices represents the maximum three-component cross-correlation value of two master waveforms including the P- and S-wave arrivals. Overall the master event waveforms show similarities less than $cc = 0.5$ which is due to different P- and S-waveforms as well as residuals between the P- and S-phase arrivals t_{S-P}. These are good indications that the selected masters are indeed representing different event locations or source mechanisms within the reservoirs.

A limitation for the selection process are the magnitudes of the induced earthquakes. Small events are unsuitable as master events since waveforms of these are visible only on nearby stations and even there with low SNRs. Careful revision of possible master events led to a minimum selected magnitude of Ml0.6. For events with larger magnitudes the duration and variability becomes more important for the correlation between the master event and the detected event. Although large magnitude master events may result in low similarity values to similar low magnitude events which are then missed by the algorithm, the amount of available earthquakes in the catalogs does not allow for an upper master event magnitude limit.

To avoid reduced similarities due to noisy stations or noise preceding and following the earthquake signals, each stations master waveforms are reviewed and cut or removed if too noisy.

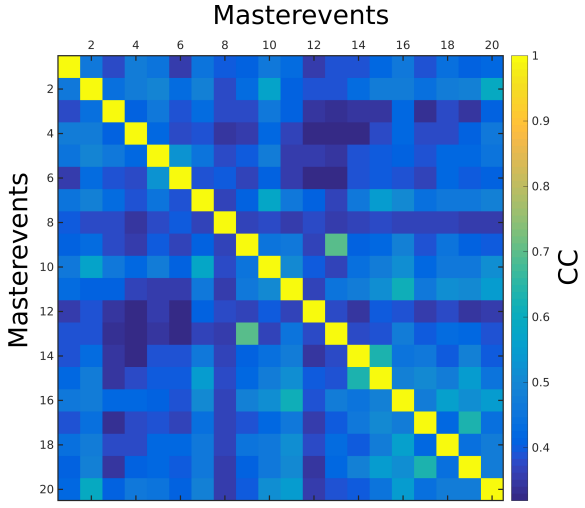

Figure 2.14.: Similarity matrix of master events selected for Insheim reservoir. Similarity is calculated as cross-correlation of 3-component waveforms including P- and S-phases of borehole station STS1.

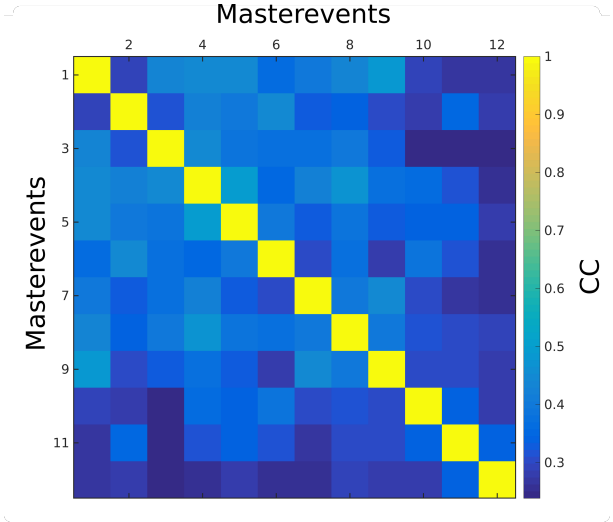

Figure 2.15.: Similarity matrix of master events selected for Landau reservoir. Similarity is calculated as cross-correlation of 3-component waveforms including P- and S-phases of borehole station STS1.

According to empirical tests, a bandpass filter of 1 to 30 Hz is applied to the data before calculating the cross-correlations. Similar to the example in section 2.2.2 the correlation noise level is determined as the mean value in a moving 100 s time window. Furthermore, a threshold of 5 is set as a reasonable trade-off between detection sensitivity and calculation effort. When a

preliminary detection is declared, no other detection is allowed within the next 10 s in order to avoid multiple recognition of the same events.

2.4.2. Detection of Insheim microseismic events

In four years of data 575 detections are found at the Insheim reservoir. About 12-16% of these are not in the catalogs while approximately 65% of the catalog events are detected again. The percentage of detected signals which are not induced earthquakes related (false alarms) is extremely low at 0.0032% (2 false alarms).

Fig. 2.16 shows histograms of detected events in the Bestec/MAGS-catalogs and the events identified by the similarity detection. The tendency of seismicity occurrence and the approximate number of events in the Insheim reservoir appear the same in all three cases. Gaps of missed events by the similarity detection are visible in 2015 and 2016. Although seven master events from 2015 are applied and 20 stations are available, a lower detection completeness in this year indicates an increasing differentiation of seismic earthquake signals during this time.

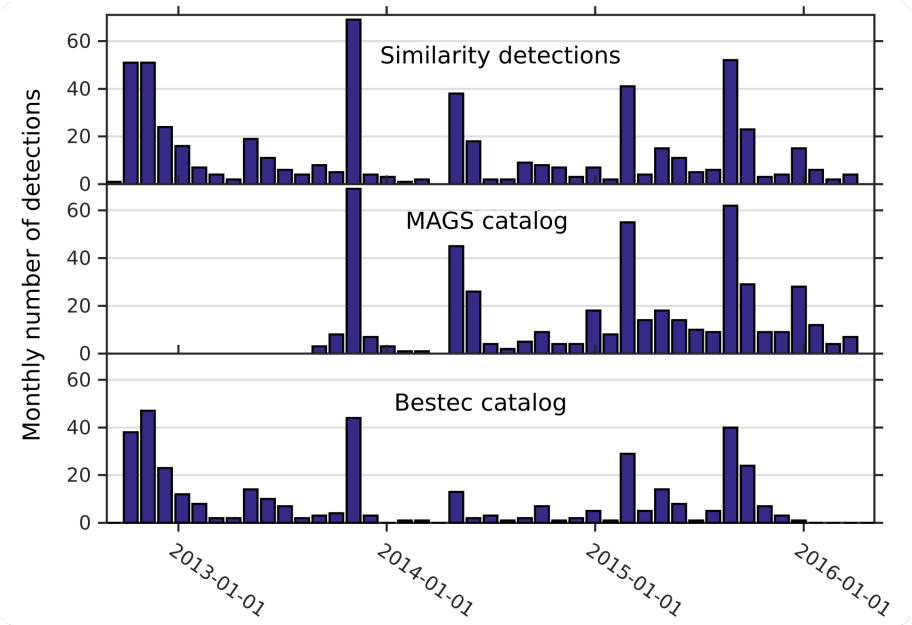

Figure 2.16.: Histogram of detections per month at the Insheim reservoir by similarity detection, in MAGS (2013-2016) and in Bestec (2012-2014) catalog.

Between 5 and 45 events are detected by each master event and assigned to the corresponding clusters. Minor quantitative differences among the clusters indicates that the seismicity is distributed equally into different parts of the reservoir.

Fig. 2.18 shows the temporal distribution of Insheim detections and maximum station specific waveform correlation indices *cc* between detection and master waveforms. Since the start-up in

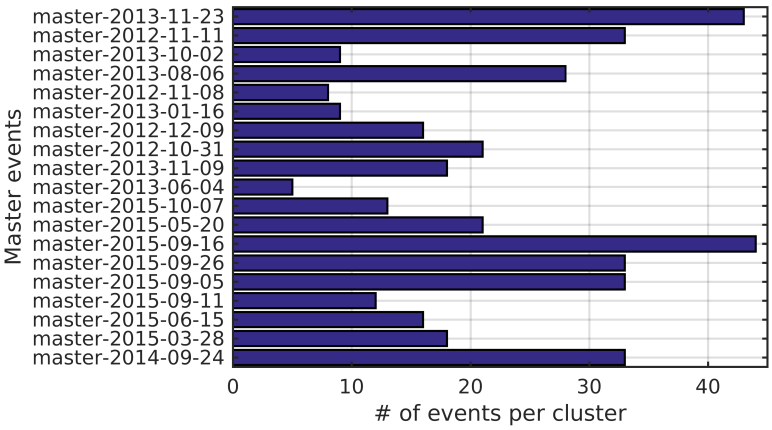

Figure 2.17.: Number of detected Insheim earthquakes per master event.

2012 a change of seismicity characteristics is observable. The dominant clusters, defined by number of detections, change over time in accordance with the corresponding master event source times. These can be identified by the highest correlation indices $cc = 1$. Furthermore, with increasing time difference between detections and master events the similarity decreases systematically. At the beginning and end of 2013, mid of 2014 and end of 2015 periods of enhanced seismicity occurrences, restricted to a few clusters, are observed. This could indicate a triggering mechanism, e.g. a production increase or shut-in of production, for these clusters.

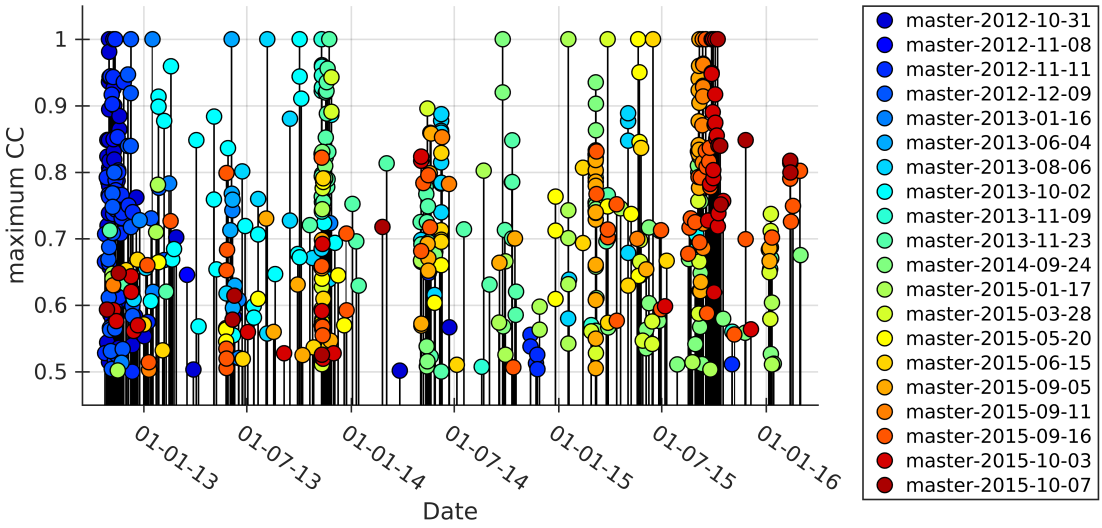

Figure 2.18.: Detection times and maximum cross-correlation values for single station with master events (colors) for the Insheim reservoir. Colors show shift of event similarities with time as different clusters are getting more and less active.

After considering the absolute timing of earthquake occurrences revealed by the similarity detections, Fig. 2.19 shows the intermediate times between sequential events of each cluster as well as the first occurrences of events of each cluster. Inter-event times range from 10 s up to

more than a year. While many clusters cover the whole time range, some clusters show preferred time periods between events. Detections with similarities to the master event on November 9^{th} 2013 shows a high number of events which follow within 10 minutes or just within a day on previous events. The cluster identified by the master events on January 16^{th} 2013 and June 4^{th} 2013 are distinct since inter-event times between sequential earthquakes are at at least half a day.

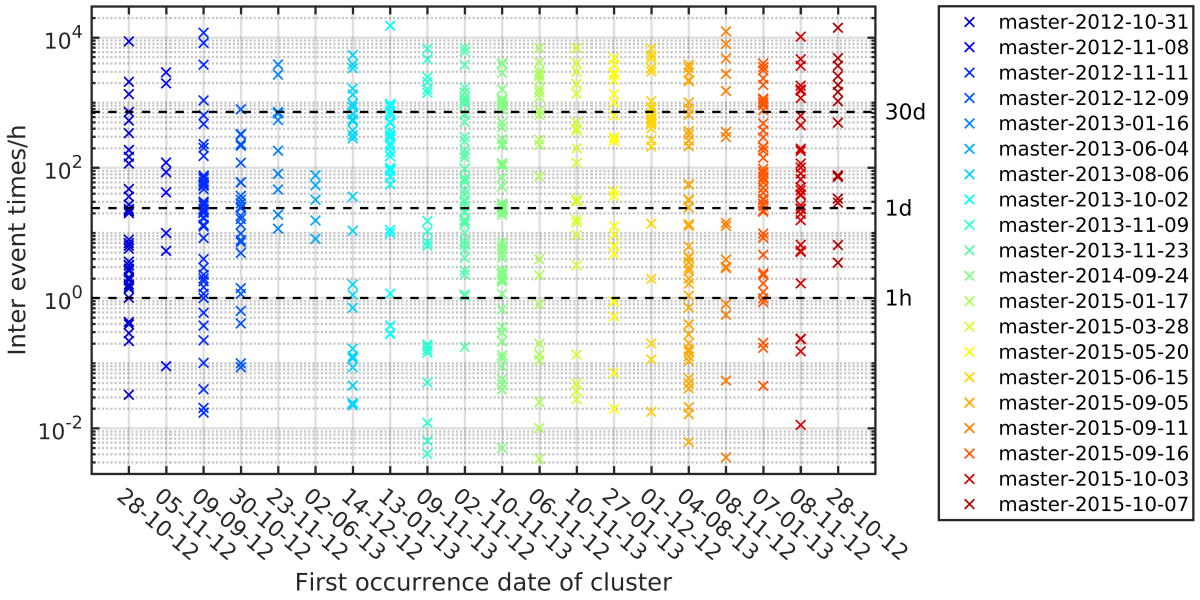

Figure 2.19.: Inter-event times of detected Insheim earthquakes sorted by clusters. On the x-axis, the first detection date of an event at each cluster is given.

2.4.3. Detection of Landau microseismic events

Since the existing catalogs for the Landau reservoir cover only parts (2010-2014 Bestec GmbH/2013-2016 MAGS) of the whole seismic activity period (2007-2016), the found detections provide a new insight into seismic activity beyond these catalogs. The seismicity declined significantly after the shutdown in 2014 (Fig. 2.20). Consequently, the number of similarity detections (838) exceeds the number of events in both catalogs by a factor of three.

In the overlapping times only about 50% of the known events are detected again while about 180 new Landau events are added. Before 2009, approximately 500 unknown events are detected by the similarity algorithm. By detecting with only one available station and a lower post-processing correlation threshold ($cc \geq 0.3$) the sensitivity is increased. A result of this is approximately 5% false alarms.

The number of detections per cluster show a completely different pattern than at the Insheim reservoir (Fig. 2.21). Three master events find each more than 100 detections while most of the others find less than 50 events. Consequently, the seismicity at the Landau reservoir is much more focused within a few clusters in contrast to the flat distribution for Insheim. This could

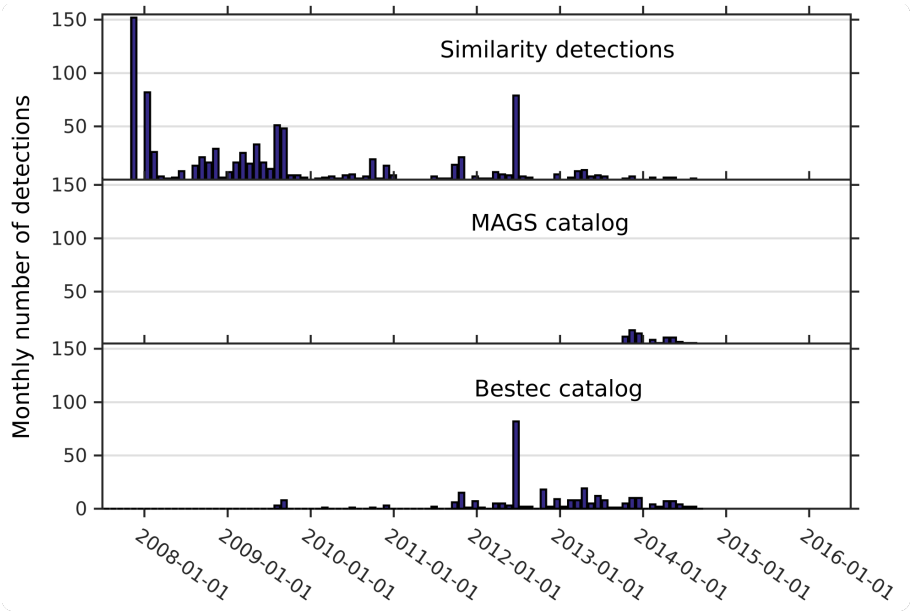

Figure 2.20.: Histogram of detections per month at the Landau reservoir by similarity detection, in the MAGS (2013-2016) and the Bestec (2012-2014) catalogs.

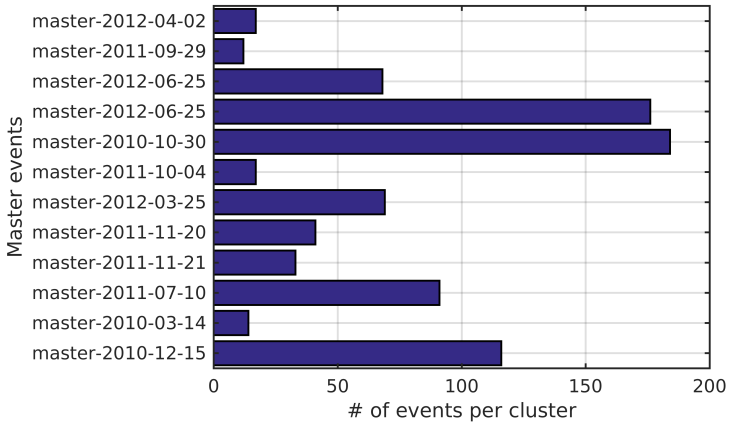

Figure 2.21.: Number of detected Landau earthquakes per master event.

indicate that the overall volume where earthquakes nucleate is much smaller at the Landau reservoir or that certain weak spots may be triggered repetitively and co-seismic stress release is concentrated there.

Fig. 2.22 shows the temporal distribution and post-processing cross-correlation values (cc) of the Landau detections. A decrease of correlation indices with residual times between detections and master events is even more distinct than for the Insheim reservoir. In consequence of the Bestec catalogs period, strong events were selected mainly from 2010 to 2013. This results in low similarities (cc<0.7) before 2010 and after 2013. The earthquake swarm on June 25^{th} 2012 stands out as well as three more concentrated occurrences of similar events which are detected at the end of 2007, beginning of 2008 and end of 2010. Overall enhanced seismicity is visible before 2010. Shifting color dominance, representing the master events, indicates changing seismicity

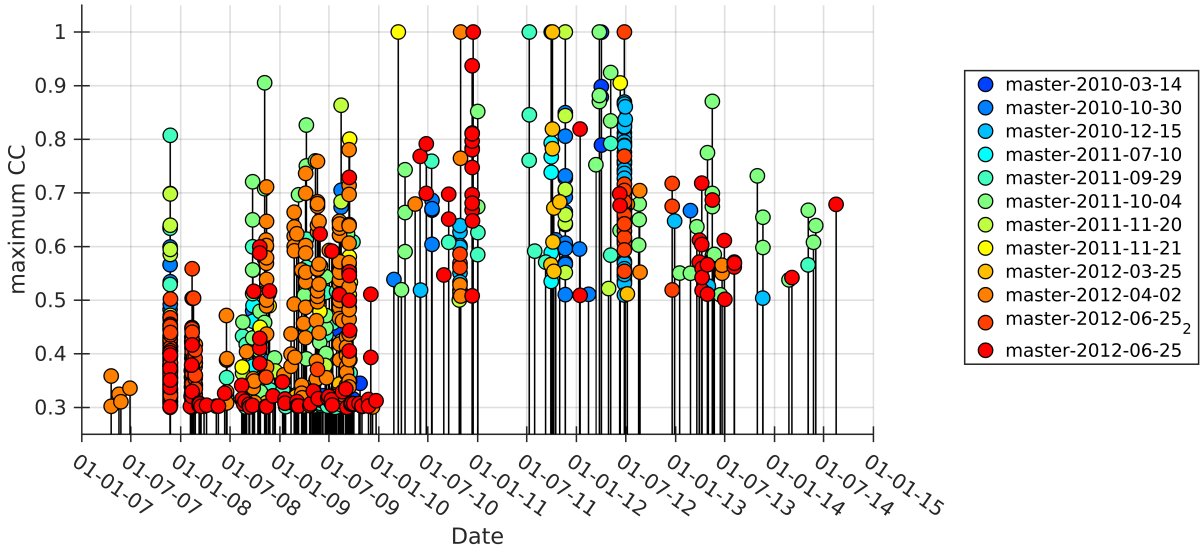

Figure 2.22.: Detection times and maximum cross-correlation indices (cc) between detection and with master event (colors) waveforms at the Landau reservoir. Colors indicate shift of event similarities with time as different clusters are getting more and less active. Before 2010 the cross-correlation threshold is reduced since only one station data (SOS2) is available.

characteristics.

Fig. 2.23 shows the inter-event times between earthquakes belonging to individual clusters. Similar to the Insheim reservoir, clusters showing inter-event times from 10 s to more than a year can be differentiated from clusters showing very distinct periods between sequential events. The master events on October 30^{th} 2010, December 12^{th} 2010 and July 10^{th} 2011 show no preferences for intermediate times. Since the master event on June 25^{th} 2012 belongs to an earthquake swarm, the inter-event times are mainly between 10 s and 30 min. The earliest master event belongs to a cluster without events in short period sequences (<1 hour).

For both reservoirs, Insheim and Landau, the applied similarity detection approach is able to complete existing catalogs adding between 15% and 50% of new events to the catalogs while determining only 0.0032% to 5% false alarms. Furthermore, it is suitable to (re-)process older data based on known master events identifying about 500 new events at the Landau reservoir before 2010. 20 clusters are found for Insheim as well as 12 cluster for Landau, each containing between 6 and 185 events.

Concentrated occurrences of earthquakes with high waveform similarity within short periods are observed for some clusters while others show scattered single event occurrences with low similarities. Declining maximum correlation indices with increasing residuals to master event source times give hints on changing seismic characteristics. Furthermore, changing dominant master events in accordance to their source times supports this. Missing detections of known catalog events indicate that further master events are required in order to re-detect up to 100% of the

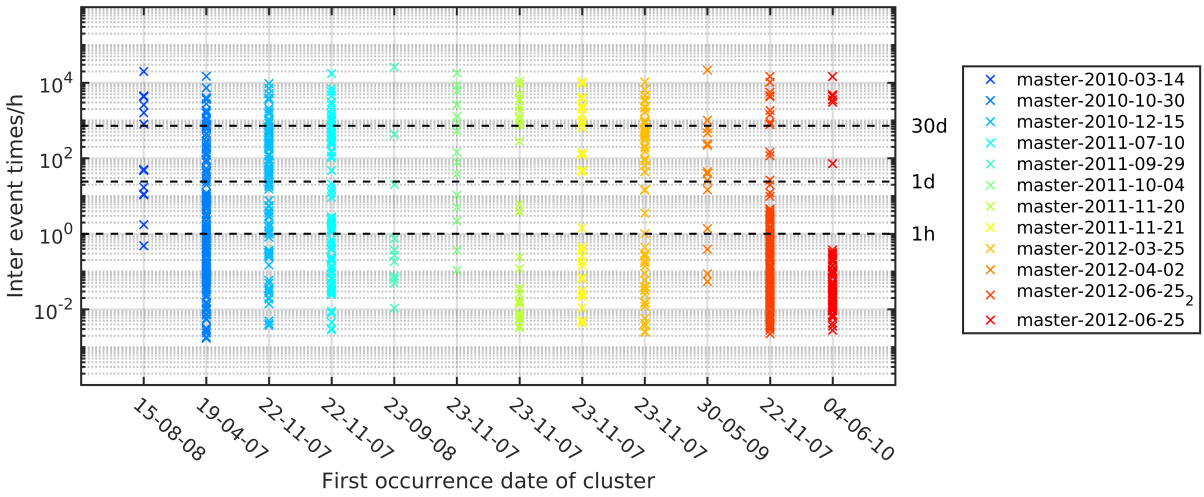

Figure 2.23.: Inter-event times of detected Landau events sorted by cluster. On the x-axis, the first detection date of an event at each cluster is given.

known induced earthquakes at both reservoirs under the premise that the undetected events occur in clusters.

2.5. Discussion and conclusion

A large dataset of partially unprocessed data and large error sources in a complex tectonic area is a challenging, yet promising, setting to be seismologically investigated. Hence a cross-correlation detection algorithm is applied to process the raw data, to complete existing catalogs and to identify clusters of events.

The algorithm uses a partially normalized cross-correlation, allowing a calculation without a moving time window. Consequently, it is able to process all the available data, ranging from a single station recording from 2007 to 2010 to up to 60 channels between 2013 and 2015. Furthermore, this calculation method provides the opportunity to estimate the detection magnitudes which could be used in hazard monitoring schemes, e.g. traffic-light systems (Bommer et al., 2006). Similar to the array detector by Gibbons and Ringdal (2006), the correlation functions of the individual channels are weighted and stacked. Since the percentage of false alarms is extremely low for Insheim, by combining correlations of multiple stations a reduction of noise-related correlations is accomplished. On the contrary, using only one station for Landau results in the slightly higher, yet moderate 5% false alarms.

While the proposed algorithm is able to compensate for a low SNR, the correlation stacking is dependent on correct timings at the recording stations. Although it is not observed in this case, GPS clock offsets at individual stations may be able to introduce an error to the correlation stacking. If the timing accuracy declines, correlation peaks of individual stations may be shifted, which would result in not positive signal interference. Temporal GPS-time shifts may be a reason for not detected induced earthquakes. However, including multiple stations lowers the dependency on individual stations with time shifts. Therefore, this is only a problem during periods when very few stations' data are available.

An evaluation of detection reliability in comparison to other applied algorithms (MAGS-similarity Vasterling et al., 2016, , Bestec STA/LTA) is problematic. 40% of the Insheim catalog and 50% of the Landau catalog were not detected. On the contrary, 70 - 90 previously unregistered Insheim events and 180 unknown Landau events are found. These gaps between detections and existing catalogs indicate that each detection method has weak points and that a complementary approach, as proposed by this algorithm, is highly recommended. In order to further discuss the weaknesses of each detection methodology, a review of individually detected or not detected earthquakes is required.

Besides adding events to complete catalogs, the similarity detector distinguishes between events belonging to different earthquake clusters within the reservoirs. Thus, the percentage of not detected events in the catalogs is expected to decline with increasing numbers of master events. At least for the Insheim reservoir where each cluster has approximately the same number of events, such a continued iterative master event selection process appears reasonable. If the number of re-detected catalog events per master remains approximately constant, the complete catalogs

could be re-detected applying about 34 master events. For the Landau reservoir, on the contrary, the success of the iterative master selection depends strongly on identifying and selecting master of clusters with many events rather than of clusters containing very few earthquakes. However, such an approach can only be successful if all undetected earthquakes actually belong to clusters which must not be the case.

Ideal master events are recorded by many stations with a good SNR. Consequently, low magnitudes are a limitation to the master event selection process. Induced earthquakes with magnitudes down to/as low as Ml0.6 were selected with at least four stations with well visible waveforms. The mainly low magnitude catalog events, which are not re-detected by other master events, do not fit these requirements. Thus, either the selection criteria must be reduced, additional station data included, or the occurrence of events with a sufficient magnitude be awaited in the future. Finally, a magnitude calculation of detected events and comparison to the other catalogs should provide a statement on how sensitive this similarity detection approach is to low magnitude events and how the other detection algorithms perform compared to it.

The 20 clusters identified at the Insheim reservoir and another 12 clusters at the Landau reservoir, as well as 40% of catalog events which are not detected, hint to differing seismic properties. Since the master event waveforms show similarities less than $cc = 0.4$ to each other, either different source regions and hence different Green's functions or alternating source mechanisms may cause the differentiation of seismicity. Both reservoirs are located in a tectonic region, where fault directions are oriented according to the former extensional regime of the URG rift valley (north-east to south-west) and the compressional-shear regime of the younger Alpine denudation (south to north). Thus, it is likely that the high number of identified clusters do not just indicate different source volumes but may differentiate between differently oriented source mechanism, as well. Furthermore, several inducing source mechanisms other than stick-slip have been observed in other deep geothermal reservoirs (Kisslinger, 1976; Segall and Fitzgerald, 1998). Such alternative inducing mechanisms could explain the differentiation of further clusters.

The similarities of detections to the Landau and Insheim master events show temporal patterns. Both, the decline of similarities with increasing residuals between detections and master events, as well as the concentrated occurrences of distinct clusters within restricted time periods, are indications for changing seismic attributes of clusters. The decreasing similarities of detections to master events over time indicate that seismic clusters migrate within the reservoir. Furthermore, the restriction of clusters to certain time periods is an evidence for repetitive failures and hence earthquake nucleation within small volumes.

Swarm events, like the one at Landau on June 25^{th} 2012 are absent at the Insheim reservoir. This raises the question, what kind of local features cause (Landau) and hinder (Insheim) these swarm occurrences? While events are distributed equally among the 20 clusters at the Insheim reservoir, the Landau reservoir shows a high concentration of seismicity within three clusters. Both

these features indicate that the seismic responses of the two reservoirs seem to be fundamentally different. Since neither detailed structural reservoir information nor precise hypocenter locations are available, an initial statement on possible mechanism differences remains problematic.

Analysis of temporal detection distributions and inter-event times of sequential events reveal another interesting attribute of clusters. While some show no particular inter-event times, earthquakes of other clusters seem to repeat at preferred rates. In case of the cluster which includes swarm events, inter-event times less than half an hour are dominant. Others show no such short period repetition times, indicating that stress is built up over longer periods (>12 hours) and released by single events. This could again indicate continuing break-ups of fractures and opening of fluid path-ways which increases the permeability of the reservoir rock over time. The fluid path-ways' orientation is expected to be according to the dominant stress regimes orientation. For the reasons that only few clusters show such a behavior, physical rock properties may be changing throughout the reservoir.

Shifts of the hypocenter locations between two events cause varying residuals between P- and S-wave arrival times. With the objective of a differentiation between clusters, we consequently chose to include both, P- and S-wave arrival times. However, to test for a complete detection, it can be argued to use only the P- or S-waveform. In case of a cluster with earthquakes migrating along a fault or sequentially further opening fractures, the source mechanism may not be changing while the migrating source locations ($t_S - t_P$) could explain the observed decreased similarity (cc) over time. Thus, if the influence of the Green's function along the ray paths does not vary significantly, but the P-to-S residual time does, a re-detection using only P- or S-wave arrivals could lead to the merge of clusters consisting of earthquakes migrating along fluid flow paths. According to (Nakahara, 2004), applying the P-arrival would lead to a less restricted differentiation between events than using the S-arrival.

Finally, to further interpret the cluster occurrences of induced microseismic events at the Landau and Insheim geothermal reservoirs, precise locations are required. However, only for the Insheim reservoir an improved velocity model and operational data are available. Thus, a discussion of the spatial distribution of clusters as well as the relation to operational shut-downs is performed in regard to the Insheim reservoir after relocating the detected events in the following chapters.

3. Automatic phase onset time determination using an AR-AIC-Cost function approach

3.1. Introduction

After having introduced a detection methodology for induced events, in this chapter we present an automatic phase arrival time determination for first and later phases of seismic signals. Only few studies investigate the application of automatic arrival time determinations on induced seismicity, although it is an application area for which consistent automatic processing is of great interest. Within this section, first the motivation to automatically determine phase arrival times is discussed introducing existing algorithms, problems and objectives. Then the AR-AIC-Costfunction approach is explained in detail. The more common application field of teleseismic data is used to show its general applicability by comparing derived automatically determined arrival times to manually derived arrival time readings, which are taken from the catalog by the International Seismological Centre (ISC). Finally, the results of applying the automated picking algorithm to the dataset of induced seismicity are presented and evaluated.

3.1.1. Motivation

Seismic phases describe direct, reflected, refracted and converted waves traveling from a seismic source to a receiver. Different seismological analysis methods investigate different phases and attributes of phases to extract information on the sources as well as on the upper- and lower crust, the mantle and the core structures dependent on the distance and path the waves travel. Besides direct traveling compressional and shear waves, subsurface structures and interfaces lead to reflected, refracted or converted wave phases. Seismological analysis methods, e.g. receiver function- (e.g. Zhang et al., 2016; Kind et al., 2017), seismic tomography (e.g. Charléty et al., 2013; Liang et al., 2016) or polarization analysis (e.g. Cristiano et al., 2016), use these phases to learn about the subsurface structures. Locating seismic events like earthquakes and large explosions is another important task, routinely accomplished by different seismological agencies worldwide. For this as well as for body wave tomography consistently and precisely determined arrival times of seismic phases at stations are required (Di Stefano et al., 2006; Diehl et al., 2009). While it is still common practice that the arrival time readings are retrieved manually, the steadily increasing number of stations (Fig. 3.1) and simultaneously growing amount of data

suggest that this becomes more and more a Sisyphean task.

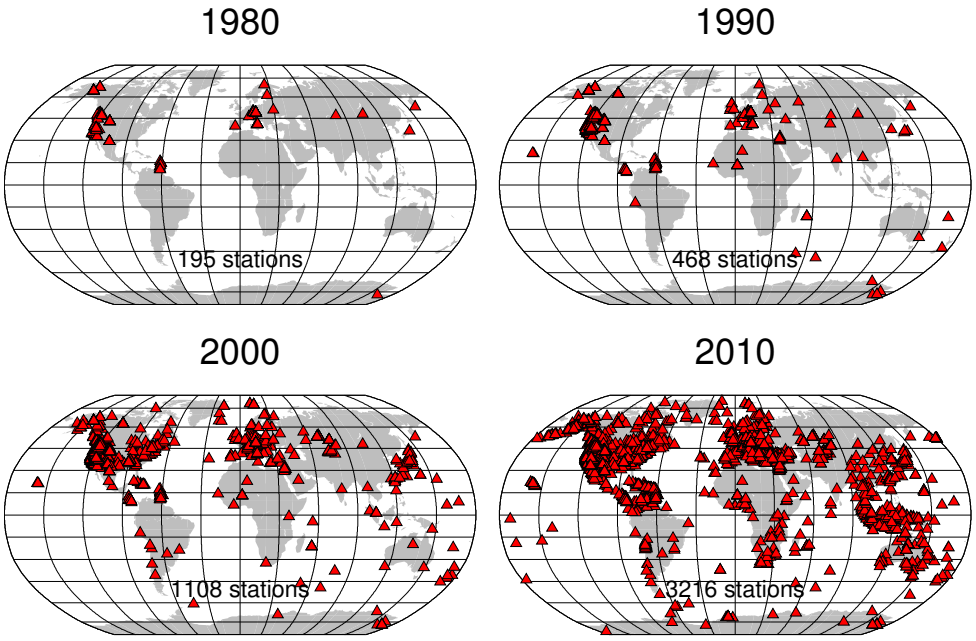

Figure 3.1.: Stations with data accessible via the GEOFON data center, operating by 1980 (top left), 1990 (top right), 2000 (bottom left) and 2010 (bottom right).

The ISC provides the largest collection of continuous earthquake detections, phase arrival readings and event locations. More than four million seismic events and explosions as well as 50 million phase arrival times for more than 6000 stations have been collected from about 130 agencies since 1964 (ISC, 2016). It is an unmatched database for global and regional tomographic studies (e.g. Soldati et al., 2015; Koulakov and Sobolev, 2006). Although ISC analysts review the collection, various studies show that phase time readings contain systematic and non-systematic errors which can be problematic to assess (Grand, 1990; Gudmundsson et al., 1990; Röhm et al., 1999, 2000; Engdahl and Ritzwoller, 2001; Diehl et al., 2009; Husen et al., 2009). These studies show exemplary errors in readings (Grand, 1990) and temporal variations of azimuth corrected median travel time residuals (Röhm et al., 1999; Engdahl and Ritzwoller, 2001) in the ISC dataset. Similar problems are evident in other datasets, where systematic reading errors of 1 s for teleseismic and regional P-phase arrival times are found (Flanagan et al., 2007).

Changing station hardware and software (Röhm et al., 1999), inconsistent analyzing behavior of operators (Röhm et al., 1999; Leonard and Kennett, 1999) as well as different processing parameters, e.g. window size, magnification and filtering (Grand, 1990; Douglas et al., 1997) are the essential reasons for systematic and non-systematic errors in arrival time readings, which can amount up to several seconds. These errors are not consistently and often insufficiently accounted for (Grand, 1990; Röhm et al., 1999). Douglas et al. (1997) find that many P-phase readings with an assigned uncertainty of 0.1 second can have actual reading errors higher than 0.5 seconds.

While the large amount of data in the ISC catalog makes it an attractive database for tomographic projects, most of the data waveforms are not available, which prohibits a retrospective error assignment. In global tomographic applications the random error propagates insignificantly into the results, while approximately 40 % of systematic errors results in blurring effects in the resulting tomographic models (Röhm et al., 2000). Both, Diehl et al. (2009) and Husen et al. (2009), compare tomographic results using automatically and manually determined phase arrival times. The studies suggest that picking and quality assessment must be done consistently and automatically in order to avoid systematic errors in the consecutive processing, e.g. on location or tomography. Since automatic picking cannot be described theoretically, engineered solution algorithms are necessary. Several such algorithm approaches developed over the last decades are introduced in the next chapter.

3.1.2. Automatic phase arrival time determination

Since the 1960s various picking algorithm proposals have been published, tested, discussed and implemented in software packages (e.g. Allen, 1978; Baer and Kradolfer, 1987; Aldersons, 2004; Küperkoch et al., 2012; Spallarossa et al., 2014). In the following, a brief introduction into phase picking and the most important algorithms is provided.

Determining a seismic phase arrival time, called "picking", is based on a high-frequency approximation of the elastic wave theory. As a result of this approximation, the elastic wave equations are simplified so that the wave propagation can be described by the start point of a wave, its take-off direction, source time and a velocity distribution according to the so called "Ray Theory". With a given velocity model, observed wave arrival times can be used to compute the location and time of the waves source. For the initial source locating procedure the velocity model is assumed to be true. Forward calculations of the arrival times for different source locations and times yield an optimum source location and source time if the residuals between calculated and observed arrival times are minimized. Furthermore, if the sources location and time are given, the observed arrival times can be used to invert for an improved velocity model.

Seismic body wave tomography is more complex. A dataset of known source locations and seismic phase arrivals at a large number of stations are processed. Starting from a 1D-velocity model, the velocity distributions and ideally also the source parameters are adjusted in an inversion process minimizing the residuals between observed and calculated phase arrivals (Pavlis and Booker, 1980; Nolet, 1987). Locating events is of fundamental importance for any seismological study, while body wave tomography is essential for studying upper mantle and crustal structures. Consequently, arrival times and their uncertainties have a significant influence on the interpretation of seismicity and the velocity model.

In order to take over an experienced manual analysts task of identifying a seismic waves arrival time, an automatic algorithm needs to analyze the waveform characteristics and differentiate

between the wave phase and preceding recording parts. These signals can be dominated by noise such as preceding first arriving phases (Pg, Pn, P) or seismic coda, i.e. scattered waves due to the 3D-heterogeneous earth, e.g. later arriving phases (Sg, Sn, S or surface waves). Consequently, agreed objectives of an automatic phase picker are 1) sensitivity towards phase arrivals, 2) precision in onset time determination, 3) time efficiency to process large datasets and finally 4) an automatic quality evaluation to avoid reviewing single arrival times (Di Stefano et al., 2006; Diehl et al., 2009; Küperkoch et al., 2010, 2012).

Automatic arrival time picking originates from event detection algorithms (e.g. Freiberger, 1963; Stewart, 1977; Goforth and Herrin, 1981), which are rather imprecise when it comes to determining the timing. Various arrival time determination algorithms have been proposed and a detailed discussion of them is provided by Küperkoch et al. (2010, 2012). The algorithms use varying statistical models to determine the arrival times:

1. short-term averages to long-term averages (STA-LTA, Allen, 1978, 1982; Baer and Kradolfer, 1987; Earle and Shearer, 1994),

2. auto-regressive (AR) predictions of traces individually or combined with the Akaike-Information-Criterion (AIC, Akaike, 1973; Maeda, 1985; Takanami and Kitagawa, 1988; Leonard and Kennett, 1999; Sleeman and van Eck, 1999; Küperkoch et al., 2012),

3. higher-order statistics (HOS, Saragiotis et al., 2002; Küperkoch et al., 2010),

4. relative travel time determination (VanDecar and Crosson, 1990),

5. combination of different approaches (Bai and Kennett, 2000; Zhang et al., 2003)

6. neural networks (e.g. Gentili and Michelini, 2006).

Recent studies propose further combined approaches like the decomposition of waveform data, e.g. eigenvalue decomposition combined with HOS (Baillard et al., 2013), a singular-value-decomposition to detect P- and S-phase arrivals (Kurzon et al., 2014) or an Empirical Mode Decomposition (EMD) combined with the AIC-picker used by Earle and Shearer (1994) (Li et al., 2017). Although it is difficult to classify the algorithms if these are not compared directly, the results indicate stable results with residuals compared to HOS or AR-AIC algorithms. In an attempt to reduce the number of parameters required for the picking process, Rawles and

Thurber (2015) apply a nearest-neighbor similarity approach, searching for signal and noise patterns with a database retrieved from manual processing.

With the increasing number of studies proposing varying algorithms, it is an important task to evaluate the skill of these approaches. Residuals between automatic and manual arrival time picks can be statistically interpreted to determine the precision of algorithms. However, many studies apply the proposed algorithms only on examples which does not allow a systematic skill evaluation of the algorithm (e.g. Kurzon et al., 2014; Li et al., 2017). Studies considering datasets with manual phase time readings show heterogeneous results. Standard deviations of the residuals range from $\pm 0.04s$ (Rawles and Thurber, 2015), $\pm 0.08s$ (Baillard et al., 2013) to $\pm 0.4s$ (García et al., 2016) for P-waves and $\pm 0.23s$ (Baillard et al., 2013) and $\pm 0.68s$ (Rawles and Thurber, 2015) for S-waves. It is however noteworthy, that each application is case dependent and the values hence do not provide enough evidence to rank the algorithms.

Studies comparing algorithms, test their application of picking approaches on the same dataset (e.g. Küperkoch et al., 2012; Sabbione and Velis, 2013). Sabbione and Velis (2013) apply the automatic pickers by Allen (1978), Baer and Kradolfer (1987) and Earle and Shearer (1994) on borehole array seismometer recordings to detect first arrivals. Finding that all algorithms perform approximately equally well, although the picker by Earle and Shearer (1994) shows a systematic bias towards picking too early. Combining results from various studies, Küperkoch et al. (2012) proposes an AR-AIC algorithm and tests it against the approach of Allen (1978), Baer and Kradolfer (1987) and a HOS-approach by Küperkoch et al. (2010). While Turino et al. (2010) find that the Allen picker and an AIC picker provide comparable results, Küperkoch et al. (2012) shows that both, HOS and AR-AIC algorithms, outperform the STA/LTA approaches regarding the signal sensitivity. Further tests indicate that while the HOS algorithm is sensitive to changes in amplitude only, the AR prediction is sensitive to changes in amplitude, frequency content and phase changes. Moreover, the AR-AIC approach is well applicable to single and multi-component data and hence to first as well as later arriving P- and S-phases.

Another way to assess the pickers skill is the comparison of advanced processing results obtained by using automatically and manually picked phase arrival times. Scafidi et al. (2016) use P- and S-wave picks, determined by using the RSNI-picker of Spallarossa et al. (2014), to relocate tectonic events in a local tomography in Northern Italy. To quantitatively compare automatic and manual processing they consider residual distributions (standard deviations of $\pm 0.13s$ for P-wave picks and $\pm 0.28s$ for S-wave picks), relative location offsets (80% of locations show an offset less than 5 km) and velocity perturbation differences ($\pm 0.5 kms^{-1}$ for P-wave velocities and $\pm 0.3 kms^{-1}$ for S-wave velocities). These consistent results indicate a good reliability and precision of the automatic phase picks.

Since the picking algorithm by Baer and Kradolfer (1987) is one of the most established, it is used by both, Di Stefano et al. (2006) and Diehl et al. (2009), in their respective local tomographic

studies. Both studies show that datasets of consistent automatic picks can match large, accumulated datasets of manual phase readings, in terms of tomographic resolution. Furthermore, they point out that a systematic quality evaluation of picks is essential. Many studies assess the skill of the automated picking by simply calculating the SNR (e.g. Baillard et al., 2013; Kurzon et al., 2014), whereas the assessment by Di Stefano et al. (2006); Diehl et al. (2009) or Küperkoch et al. (2010) is the definition of quality classes according to more elaborate measures. Di Stefano et al. (2006) and Küperkoch et al. (2010) combine attributes of the waveforms, like the waveform sampling rate, the spectral density analysis, the SNR and the impulsiveness of the CF to determine the uncertainty of automatic picks. Diehl et al. (2009) provides uncertainty measures towards later and earlier time, i.e. latest- and earliest likely phase arrival times, based on the noise amplitude and the dominant signal period. In each of these individual evaluation studies, the respective approaches perform well making a ranking difficult once more.

Based on the evaluation analysis by Küperkoch et al. (2012), in this study we aim to combine a well established AR-AIC phase detection algorithm with a cost-function. In the direct comparison to HOS- and the established (Allen, 1978) and Baer and Kradolfer (1987) picking approaches, the AR-AIC algorithm outperforms the others. However, a complex process of training sensitive parameters make it difficult to adopt to new datasets. Thus, in order to provide a more comprehensible approach providing quicker, robust and precise results, a cost function is added on top. A cost function combines characteristics of the waveform picking and thereby may be able to improve the estimation of robust and precise P- and S-wave arrival times. Furthermore, it can be straightforward optimized for different datasets since each parameter function can be weighted individually.

Furthermore, having a large dataset of located induced events a similar approach to Li and Peng (2016) is taken. They determine theoretical arrival times from local velocity models and apply an automatic picking algorithm around these reference times. By using iterative relocations of earthquakes and re-picking of arrival times, they improve the velocity model such that the residuals between automatically determined arrival times and calculated onset times are minimized. Thus, instead of applying the algorithm on continuous data streams to detect and pick phase arrivals, we use calculated phase reference times around which the arrival times are determined.

In opposition to the applications of proposed algorithms to small datasets or examples, the automatic picking algorithm proposed here is tested on a teleseismic dataset before applying it to local induced seismicity to prove its applicability to different settings.

3.2. AR-AIC-Costfunction algorithm

After reviewing various methods, the AR-AIC algorithm by Küperkoch et al. (2012) is selected as basis for the picking algorithm introduced in this section. It is sensitive to changes in amplitude, phase and frequency, applicable to first as well as later phases and multi-component recordings while a small number of parameters needs to be optimized before application. However, Küperkoch et al. (2012) find that a single AR-AIC application determines automatic picks slightly too late. Thus, they apply the AR-AIC combination twice with a second AR-prediction including higher frequency parts of the signal. Instead of using the AR-AIC approach repetitively a cost function is proposed here.

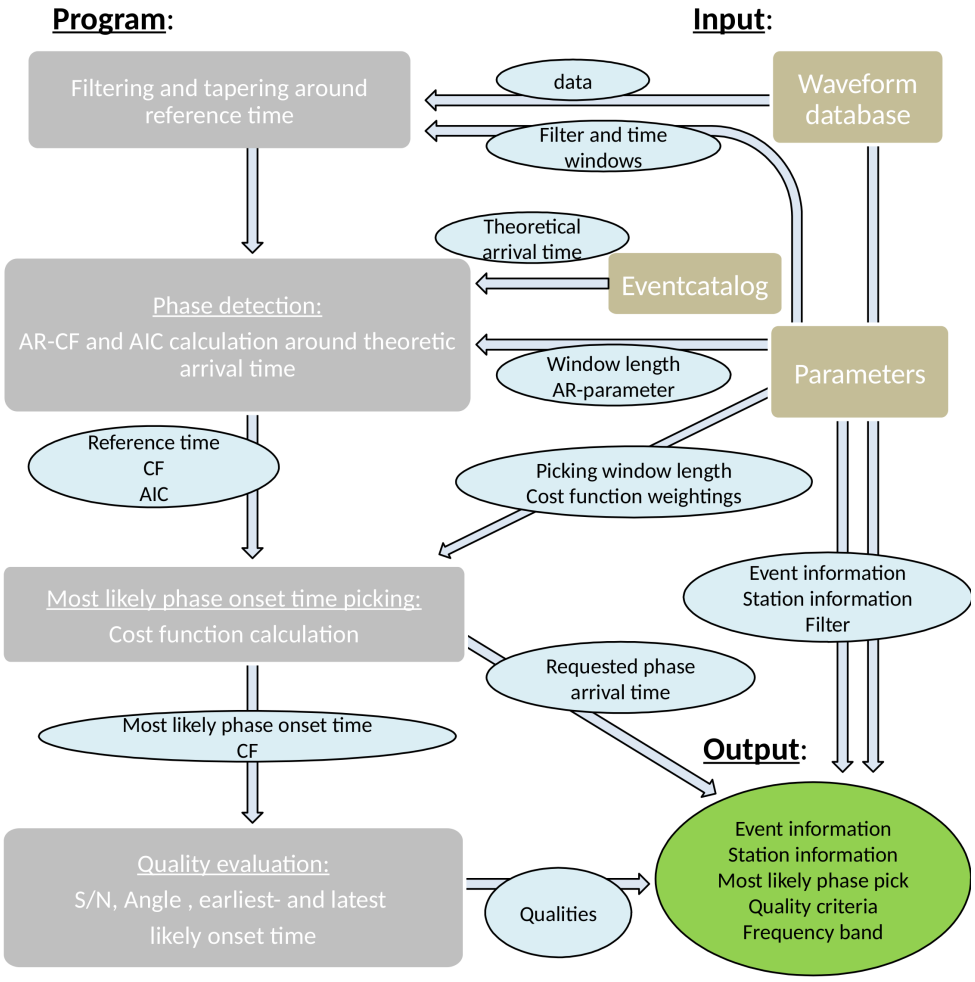

Figure 3.2.: Flowchart of the picking process. The input (olive boxes) consists of waveform data, event- and station information, the theoretical travel time and the picking parameters. The picking process (gray boxes) is subdivided into the preparation of the data, the phase detection, the phase onset time picking and the quality evaluation. Saved to the output are both event- and station information, the phase onset times as well as the quality criteria and the frequency band.

Overall, the picking algorithm can be divided into four major steps shown in Fig. 3.2:

1. The preparation of the waveform data with filtering and tapering.
2. The phase detection where a reference time for the arrival time picking is determined.
3. The onset time picking using the cost function approach.
4. A quality evaluation of the automatic pick.

In the following, the individual steps are discussed in detail.

Preceding the wave arrival time determination, waveform data is pre-processed. The data is cut around the theoretical arrival times which are considered as a reference time, similar to Li and Peng (2016). Both, single and multi-component data can be processed. In order to reduce noise signals in the recordings a third order butterworth bandpass filter is applied. Following these preparation steps the requested phase is identified within the defined time window.

3.2.1. AR-AIC phase detection

Similar to Küperkoch et al. (2012), a characteristic function (CF) is determined using auto-regressive waveform prediction. A CF is generally defined as a non-linear transformation of the waveform. When referred to in picking approaches, it is supposed to illustrate the change in waveform characteristics by an indicative, swift change in amplitude.

Calculating an AR-prediction requires multiple steps. At first AR-parameters, which linearly connect samples to its preceding data, are determined. The number of AR-parameters, the so-called order of the AR-prediction, indicate how many preceding samples are considered to predict the following one. By least-square minimizing the AR-prediction equation for a given data sequence, the optimal AR-parameters are determined. Since short period signals may be changing over time, the parameter determination is performed repetitively in a moving time window, the determination window. Depending on the order of the AR-prediction, more complex signals can be predicted while increasing the calculation effort.

Following the determination a second moving time window, the prediction window, is defined in which the AR-parameters are applied to predict the single or multi-component waveform samples. These windows are moving simultaneously without overlap. The error of the waveform prediction is then defined as CF according to:

$$CF(t_{l+lpred}) = \sqrt{\frac{1}{M}\sum_{c=1}^{M}\left(\frac{1}{lpred}\sum_{i=l}^{l+lpred}[y_c(t_i) - \hat{y}_c(t_i)]^2\right)}, \tag{3.1}$$

where $y_c(t_i)$ is the time series on component c, $\hat{y}_c(t_i)$ is the predicted waveform on component c, M is the number of components considered and $lpred$ is the length of the prediction window in samples.

Selecting an AR-order between 2 and 4 according to Leonard and Kennett (1999) and Küperkoch et al. (2012), noise can be predicted well, while the AR-error increases when a seismic phase is recorded. Fig. 3.3 und 3.4 show the CF based on the AR-prediction error as well as the AIC exemplary for an induced P- and S-wave example recorded at the borehole station STS1 on 29^{th} December 2013.

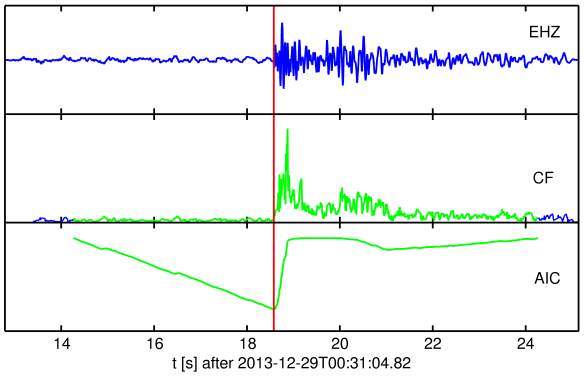

Figure 3.3.: Vertical component (third order butterworth bandpass filtered 1-30 Hz), characteristic function (CF) based on the AR-prediction error of the vertical waveform and the Akaike-Information-Criteria (AIC) as well as phase detection time (red).

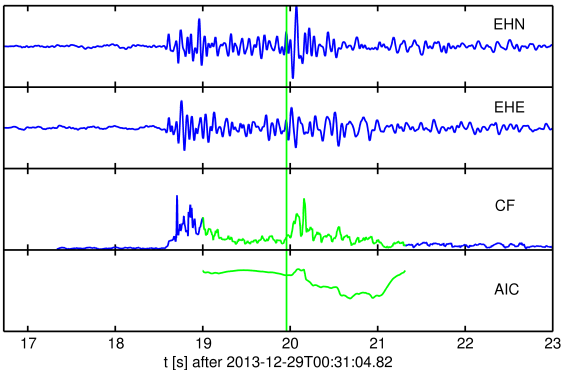

Figure 3.4.: Horizontal components (third order butterworth bandpass filtered 2-25 Hz), characteristic function (CF) based on the prediction error of the horizontal components and the Akaike-Information-Criteria (AIC) as well as phase detection time (green).

The CF is in contrast to the waveform purely positive and can be described to consist of two sequential parts. First low amplitudes due to well-predictable noise followed by large prediction errors due to the less predictable waveform of the considered phases.

The AIC, originally used as a model fit evaluation criteria (Akaike, 1973), applied to the CF is expected to decrease steadily. At the time of transition from one model to the other a minimum is found followed by a swift increase afterwards (Leonard and Kennett, 1999). This AIC-minimum is defined as phase detection time (red/green vertical line) around which the arrival time picking is applied.

While the AIC minimum for the P-wave is found as expected, for the S-wave example the global minimum is located at the transition from the S-waveform to coda. Here this second transition is more dominant. Therefore, the local minimum preceding the global maximum is selected as phase detection time similar to Küperkoch et al. (2012).

The window length in which the AIC is calculated and in which the phase detection time is found (green marked in Fig. 3.3 and 3.4) can be reduced on one or both sides if other dominant phases arrive immediately before or after the theoretical arrival time.

In contrast to the original approach, the time window defined for phase picking Δt_{Pick} is asym-

metric around the phase detection time with a larger part preceding the phase detection time.

3.2.2. Cost function

Instead of repeating the AR-AIC concept with a higher sampling rate, to determine the phase arrival time, a cost function approach is selected. The repetitive AR-AIC approach requires a complicated parameter training, while the concept of a cost function is straight forward. It provides a simple and robust approach to combine different transformations of the waveform by a simple, weighted sum. Following the phase detection, the cost function $C(t_i)$ is defined within the picking window Δt_{pick} according to:

$$C(t_i) = \sum_{j=1}^{3} C_j(t_i), \tag{3.2}$$

where C_j are parameter functions of the waveform. A phase onset is supposed to coincide with the last minimum of the CF before its amplitude raises due to larger prediction errors. As a result, including the CF in the cost function avoids a late minimum. In addition, two parameter functions which penalize too early times with large amplitudes are considered as well. These three parameter functions are shown in Fig. 3.5 and 3.6 and are defined as:

$$C_1(t_i) = \begin{cases} w_1, & \text{if } \widetilde{CF}(t_i) < w_1, \\ \widetilde{CF}(t_i), & \text{else,} \end{cases} \tag{3.3}$$

$$C_2(t_i) = \begin{cases} w_2 \cdot |\frac{t_{AIC} - t_i}{\Delta t_{pick}}|^{\frac{1}{k}}, & \text{if } t_i < t_{AIC}, \\ 0, & \text{else,} \end{cases} \tag{3.4}$$

$$C_3(t_i) = w_3 \cdot \left| \frac{2 \cdot \frac{dCF_{sm}}{dt}(t_{AIC})}{\frac{dCF_{sm}}{dt}(t_i) - \frac{dCF_{sm}}{dt}(t_{AIC})} - 1 \right|, \tag{3.5}$$

where $\widetilde{CF}$ is the median normalized CF, t_{AIC} is the phase detection time, k is a parameter controlling the shape of C_2 (k=2 in this study), CF_{sm} is a smoothed CF, and w_1, w_2 and w_3 are the cost function weighting parameters.

- The median normalized CF is the first parameter function. Preceding the phase onset, small scale variations of the CF are visible. To not set the phase pick in any of these minor minima a "water level" is defined.

- The second parameter function C_2 penalizes times before the AIC minimum. It decreases until the AIC minimum and is zero afterwards. Its amplitude is controlled by weighting factor w_2.

- Very low noise recordings can influence the stability of the AR-prediction. In order to avoid low CF amplitude variations preceding the phase arrival, the third function C_3 penalizes low gradients of a smoothed CF. Its magnitude is controlled by the weighting factor w_3. The application of C_3 is reasonable for first arriving phases without preceding coda.

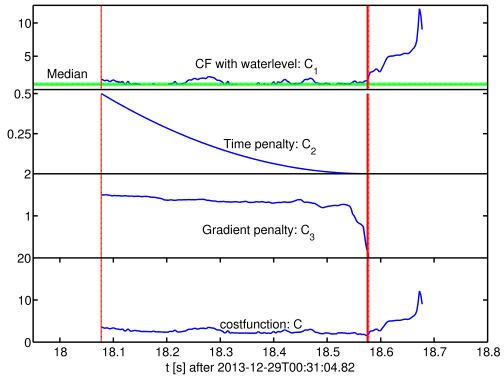

Figure 3.5.: Three parameter functions: median normalized CF with "water level", C_1, AIC-residual penalty C_2 and gradient penalty C_3 as well as final cost function with automatic P-wave pick.

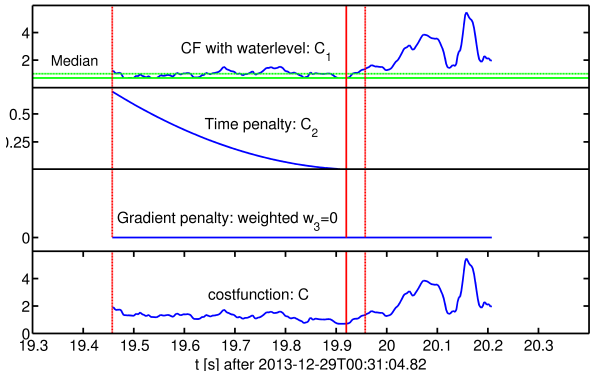

Figure 3.6.: Three parameter functions: median normalized CF with "water level", C_1, AIC-residual penalty C_2 and gradient penalty C_3 as well as final cost function with automatic S-wave pick.

Consequently, all three cost function parameters are defined positively and comparably weightable. The resulting most likely phase onset time (solid red) is defined by the minimum of the cost function. Rawles and Thurber (2015) argue that a picking algorithm must be easy to train in order to be applicable for different datasets. A big advantage of this approach is the well comprehensible weighting scheme through the cost function. It can be easily trained and adjusted for different phases and datasets. In the S-phase picking example above, the gradient penalty weight w_3 is set to zero. Waveform coda preceding the S-wave arrival results in larger prediction errors and hence in a stronger perturbed CF. The gradient penalty reflects it by showing several minima preceding the S-wave arrival and therefore favors too early S-wave picks.

3.2.3. Quality evaluation and final pick

Large waveform datasets can be processed by automatic picking approaches. However, due to complicated waveforms, low SNRs and seismic attenuation it is uncertain whether a wave arrival is actually visible in the data and whether the algorithm recognized the phase onset. A consistent evaluation procedure to distinguish between reliable and unreliable automatically determined arrival times is therefore highly recommended.

A quality evaluation is performed assigning a single quality value to each automatic wave arrival time. In consistency with the original approach by Küperkoch et al. (2012), SNR values of the single or multi-component waveform and the CF are calculated as well as a measure of the impulsiveness of the phase arrival. In contrast to Küperkoch et al. (2012), who use the steepness of

a slope fitted to the CF, here the angle of the slope is considered (Fig. 3.7). It has the advantage of being independent from the actual CF values and therefore more stable. Impulsive onsets of large magnitude earthquakes result in extreme steepnesses of the CF slope. The slope steepness of smaller, yet still impulsive phase onsets are then underrated, while the difference in angles between the CF slope of large and smaller earthquakes are minor.

Furthermore, while Küperkoch et al. (2012) performs an evaluation using all measures for all picks individually, here a combination of these measures to a single quality value Q_i per pick i is proposed, according to:

$$Q_i = MEDIAN[\frac{SNR_{TS_i}}{\widetilde{SNR_{TS}}}, \frac{SNR_{CF_i}}{\widetilde{SNR_{CF}}}, (\frac{ANG_{CF_i}}{\widetilde{ANG_{CF}}})^k], \tag{3.6}$$

where SNR_{TSi}, SNR_{CFi} and ANG_{CFi} are the SNRs of the time series and the CF as well as the CF slopes' angles determined for the picks i. $\widetilde{SNR_{TS}}$, $\widetilde{SNR_{CF}}$ and $\widetilde{ANG_{CF}}$ are the median values of the SNRs and the angles over all determine arrival times at all stations of a dataset. The normalization aims to remove the units while the exponent k provides comparability of ranges among the limitless SNRs and the limited angle. The same procedure can be carried out for existing manual picks as well to evaluate their reliability.

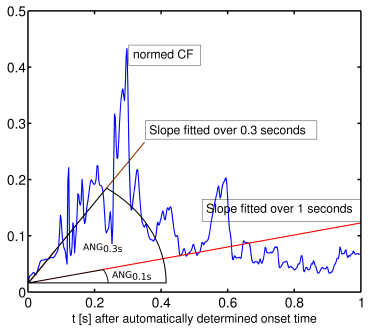

Figure 3.7.: Median normalized CF and fitted linear slope to determine angles $ANG_{\Delta t}$ as measure of impulsiveness after the automatically determined pick over $\Delta t = 0.3s$ and $\Delta t = 1s$.

The qualities cannot be directly translated into picking uncertainties, however a training on a reference manually picked dataset including uncertainties can provide an estimation on which quality values Q_i coincide with certain picking uncertainty estimation of manual processors.

While the resulting P-wave pick is well positioned immediately at the first P-phase impulse (Fig. 3.8), the S-wave pick is found within a phase-change on the East-West-component preceding the S-wave impulse (Fig. 3.9). Again the position is reasonable and the pick rated reliably. However, an individual example provides only very limited evidence for precision or goodness of the algorithm. For this reason, the application on a test dataset of teleseismic events recorded at stations of the Germany Regional Seismic Network (GRSN) is presented in the following chapter.

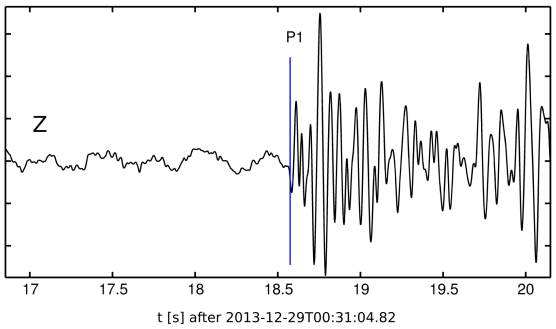

Figure 3.8.: Vertical component (third order butterworth bandpass filtered 1-30 Hz) and automatically determined P-wave phase arrival time (P1).

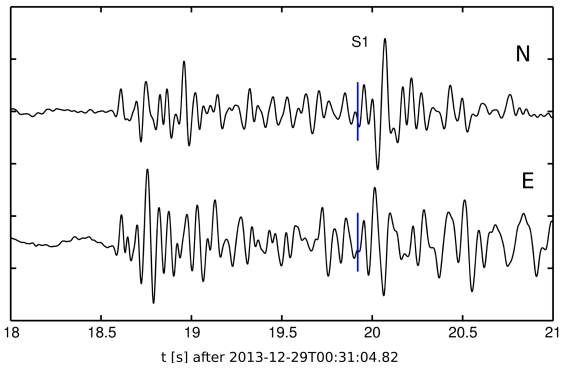

Figure 3.9.: Horizontal components (third order butterworth bandpass filtered 1-30 Hz) and automatically determined S-wave phase arrival time (S1).

3.3. Performance test on teleseismic seismicity

After introducing the algorithm, its performance is tested on a dataset of teleseismic recordings at the German Regional Seismic Network (GRSN). The teleseismic application is the most common because mantle phases are essential for tomographic studies. First the database is introduced, followed by the presentation of the results. Finally, tests using different filtering bands and component rotation are discussed.

3.3.1. Teleseismic dataset

The teleseismic database consists of 1,552 tectonic earthquakes from 1990 to 2012 taken from the EHB catalog (Engdahl et al., 1998; International Seismological Centre, 2009) and the Reviewed International Seismological Center Bulletin (ISC, 2016). A prior selection of allowed magnitudes and epicenter distances is performed. In case of strong events a possible influence of source time functions is suppressed while for weak events strong enough signal amplitudes are ensured. Event station combinations at distances between 10° and 100° for the teleseismic P-phase and 10° to 80° for the teleseismic S-phase are considered. Below 10° the first arriving P- and S-phases are crustal ones. Beyond the maximum distances the P- and S-phase waveforms are superposed by at the core-mantle boundary (CMB) refracted wave phases (Pdiff) as well as the core penetrating phases (SKS).

The distribution of considered earthquake magnitudes reflects the restrictions to smaller events closer to Europe and larger events in the major tectonically active regions: the mid-oceanic ridges in the Red Sea, Atlantic-, Pacific- and Indian Ocean as well as the subduction zones in Japan, Chile, Peru, Mexico, Alaska, New Zealand, Indonesia, Philippines, India, Iran, Greece and Italy as well as intracontinental earthquakes, for example in East Africa, Turkey or North China and Mongolia (Fig. 3.10). The intermediate deep and deep events correspond to the subduction zones around the Pacific Ocean as well as the Hellenic and Calabrian subduction zones.

Recordings of the events at 65 station of the German Regional Seismological Network, the Gräfenberg array, the GEOFON network, the Bavarian network, the Thüringen network and the Saxonian network are considered, depending on the distance and availability. The station map in Fig. 3.10 shows a dense distribution of stations in central Germany, particularly in Saxony, Thüringen and northern Bavaria. In north eastern Germany, in Schleswig Holstein as well as the Westphalia and Hessen regions the station density is lower.

The broadband recordings are sampled at 20 Hz and corrected for the instrumental responses. Teleseismic P- and S-phase arrival times are calculated using the TauP tool (Crotwell et al., 1999) included in the python ObsPy module (The ObsPy Development Team, 2016) using the AK135 velocity model (Kennett et al., 1995). Altogether 44,761 automatic P-phase as well as 19,359 S-phase onset times are determined. A comparison to 11,813 available manually deter-

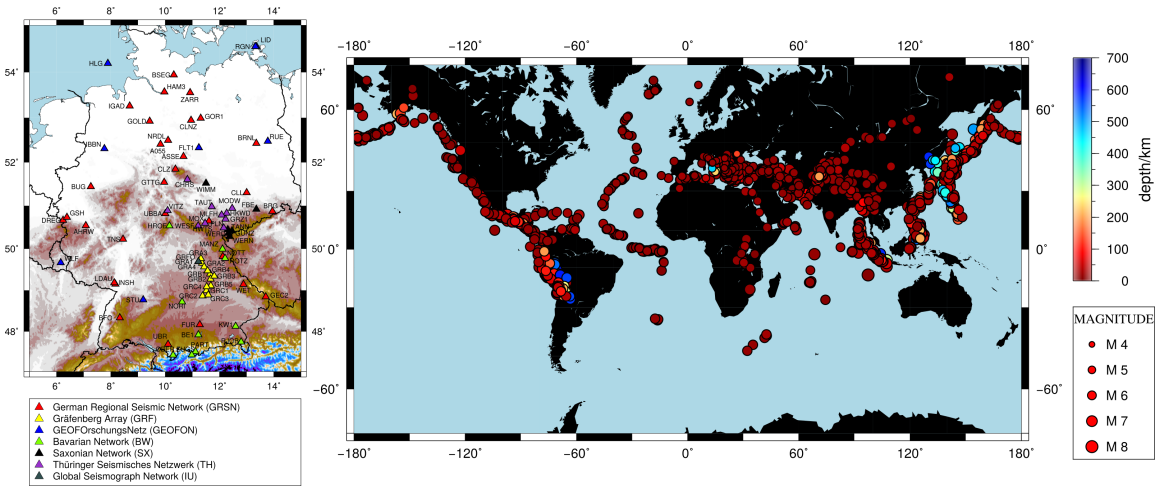

Figure 3.10.: Map with locations, depths and magnitudes of 1,552 teleseismic earthquakes taken from EHB catalog (Engdahl et al., 1998; International Seismological Centre, 2009) and the Reviewed International Seismological Center Bulletin (ISC, 2016). The magnitudes range from M 4.8 to M 8 dependent on the epicenter distance to the broadband stations shown in the smaller map of Germany.

mined routine P- and 1,415 S-picks obtained from the ISC bulletin (ISC, 2016) is carried out. The much lower number of S-phase onset times results from the stricter distance restriction (10° -80°) and the lower availability of the required horizontal components. For the P-phase the vertical component recordings are filtered with a third order bandpass filter from 0.25 to 3 Hz. Küperkoch et al. (2012) showed that the AR-prediction works on the unrotated components as well as on the rotated components. Therefore, the S-phase arrivals are initially determined on the unrotated components.

3.3.2. Results

Applying the algorithm on big-scale datasets requires a statistical analysis approach which is discussed in this section. Automatically determined P- and S-phase onset times are compared to manual picks and the theoretical travel times according to the AK135 velocity model (Kennett et al., 1995).

Teleseismic P-phase

The quality evaluation of the whole P-phase dataset is done according to formula 3.6 described in section 3.2.3. Therefore individual quality values for each determined arrival time are calculated as mean of the SNRs and the angle of the CF. These are normalized over the whole dataset. In order to adjust the ranges of the different quality criteria, the normalized angle is taken to the power of ten. Therefore, values above the median are increased while angle values below the median are weighted down. In general, the SNR is expected to be large for first arriving phases since no waveform coda precedes the signal arrival.

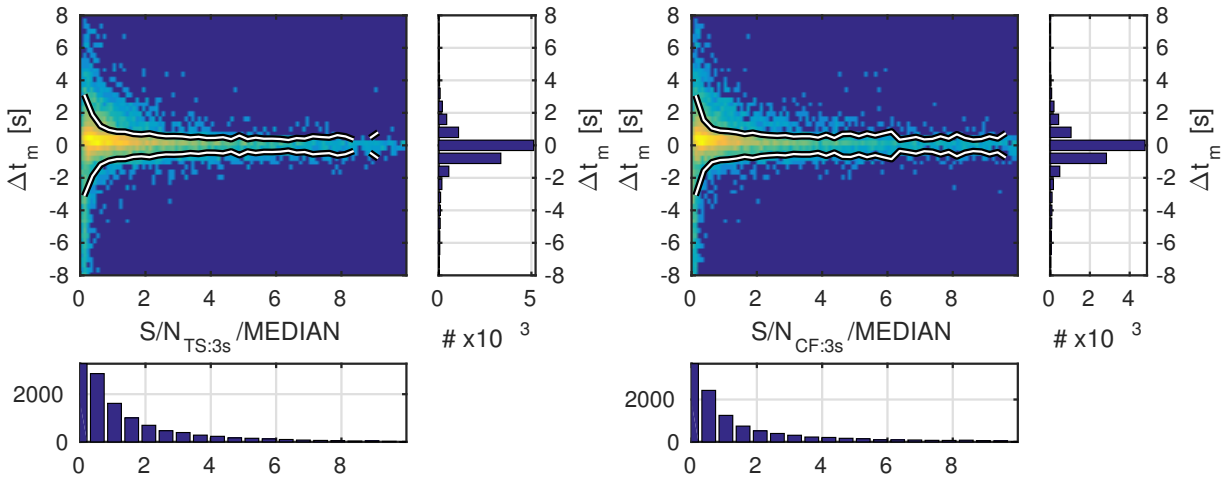

Figure 3.11.: 2D histograms of quality parameters of the P-phase picks. Left: the signal-to-noise ratio of the waveform is given as a function of the residuals between the automatic and manual picks (ISC, 2016). Right: the signal-to-noise ratio of the CF is given as a function of the residuals between the automatic and manual picks (ISC, 2016). Red colors indicate large numbers. The white lines indicates the standard deviation of the residuals as a function of the SNRs.

For a reasonable quality evaluation, the frequency of large residuals are expected to decrease with increasing quality values. Furthermore, picks with good qualities are expected to have unbiased residuals. Both attributes can be observed for both, the SNR of the waveform and of the CF (Fig. 3.11). The standard deviation of the residuals (white lines) decreases steeply up to about $\frac{S/N}{MEDIAN} = 0.7$. For larger quality values the slope is negligible but the standard deviation is already less than $\pm 0.5s$.

On the contrary, the residuals' standard deviation decreases steadily with increasing angles (Fig. 3.12 left) which confirms that the slope angle is an independent measure. While for the SNRs (Fig. 3.11) the majority of picks show low qualities, the quantities are distributed rather equally over the slopes range.

The median quality criteria Q is shown on the right side in Fig. 3.12. Low quality automatic P-phase picks ($Q < 0.5$) are determined systematically earlier than the reference manual picks. Consequently, the picking algorithm tends to pick early in cases of low SNRs or emergent P-wave arrival waveforms. Beyond $Q \approx 0.5$ the standard deviation is reduced significantly. This observation is used to identify unreliable automatic arrival times due to large SNRs or complicated waveforms that results in large residuals.

The decrease of residual standard deviation with increasing quality shows that the evaluation method is able to identify the residual outliers and provide reliable P-phase picks by large quality values.

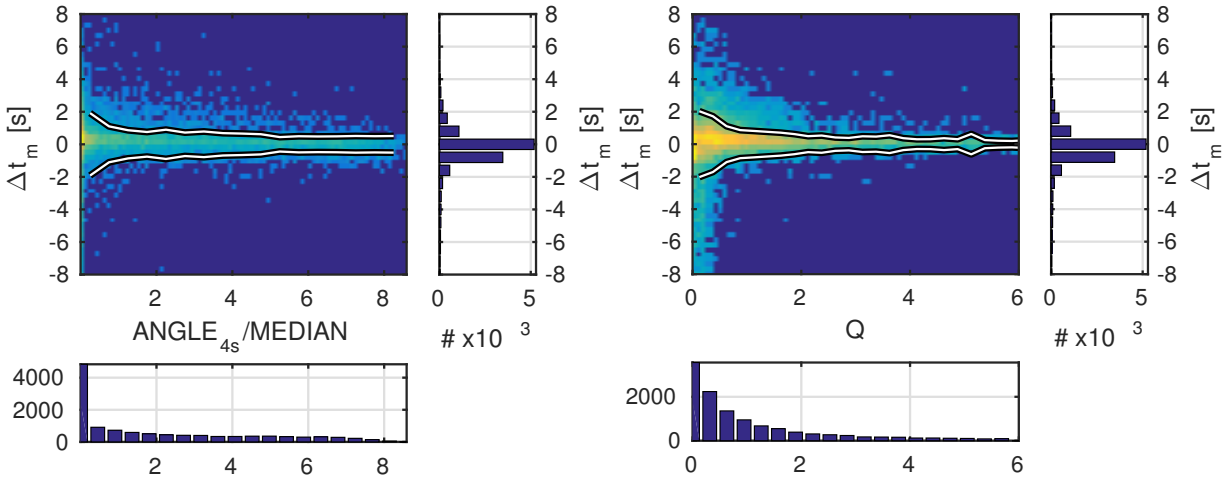

Figure 3.12.: 2D histograms of quality parameters of the P-phase picks. Left: the slope of the characteristic function is given as a function of the residuals between the automatic and manual picks (ISC, 2016). Right: the average quality is given as a function of the residuals between the automatic and manual picks (ISC, 2016). Red colors indicate large frequencies. The white line indicates the standard deviation as a function of the angle and quality measure.

Applying no quality restriction, the residuals to the theoretical arrival times appear unbiased (Fig. 3.13). Removing low quality picks ($Q \leq 0.5$), the mean residual value shifts to approximately $+0.4s$. With increasing qualities the standard deviations of the residuals decrease from $\pm 1.92s$ to $\pm 0.77s$. Considering only picks with $Q > 0.5$ already removes all automatic phase picks which are more than $\pm 2.5s$ off. To analyze the shape of distributions, the statistical measures kurtosis and skewness are included. The kurtosis indicates how flat-topped (<3) or peak-like (>3) distributions are compared to a normal distribution. Skewness describes on which side of the distribution peak the larger quantity is positioned. Although many automatic picks, which are close to the theoretic travel times, are removed as well, the kurtosis increases strongly for the restrictions $Q > 0.5$ and $Q > 1$. This indicates that for these cases more large residual picks are removed than picks around the mean value. For the even stricter restriction, the main reduction of residuals is observed around the mean value reducing the kurtosis again.

The residuals between the manual and automatic phase onset times (right) show a similar distribution with much lower standard deviations. Mean values around $0.01 - 0.23s$ show that the residuals are nearly unbiased. Late phase picks are evaluated more critically resulting in an asymmetric reduction of residuals with increasing quality. Considering the best quality picks only, the residuals between automatically and manually determined P-wave readings have a standard deviation of $\pm 0.49s$ around $0.09s$.

The distribution of the residuals between manually picked and theoretical P-phase onset times (Fig. 3.14) is shifted similarly to the residuals between automatically determined picks and theoretical arrival times (Fig. 3.13 left). Qualities shown are the evaluated quality of the reference automatic picks. The distribution appears much broader than for the automatic to manual picks residuals' distribution. The standard deviation is $\sigma = \pm 1.16s$. With half the standard deviation

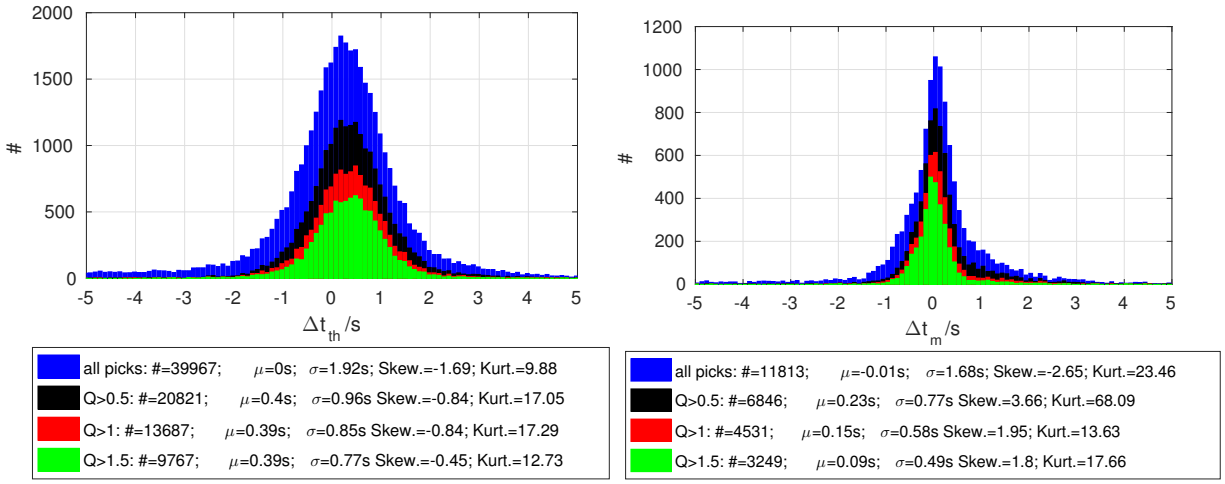

Figure 3.13.: Histograms of residuals between automatic P-phase picks and AK135 - theoretic arrival times (left) (Kennett et al., 1995) as well as automatic and manual P-phase picks (right) (ISC, 2016). Coloring indicates the minimum quality Q of automatically determined picks in each distribution according to the legend.

the automatic phase onset times are therefore much more precise and unbiased compared to the theoretical phase arrival times. The automatic assignment of qualities to manually read arrival times appears to be useful tool and should be considered for future applications. It may identify unreliably picked arrival times and help to evaluate accumulated catalogs.

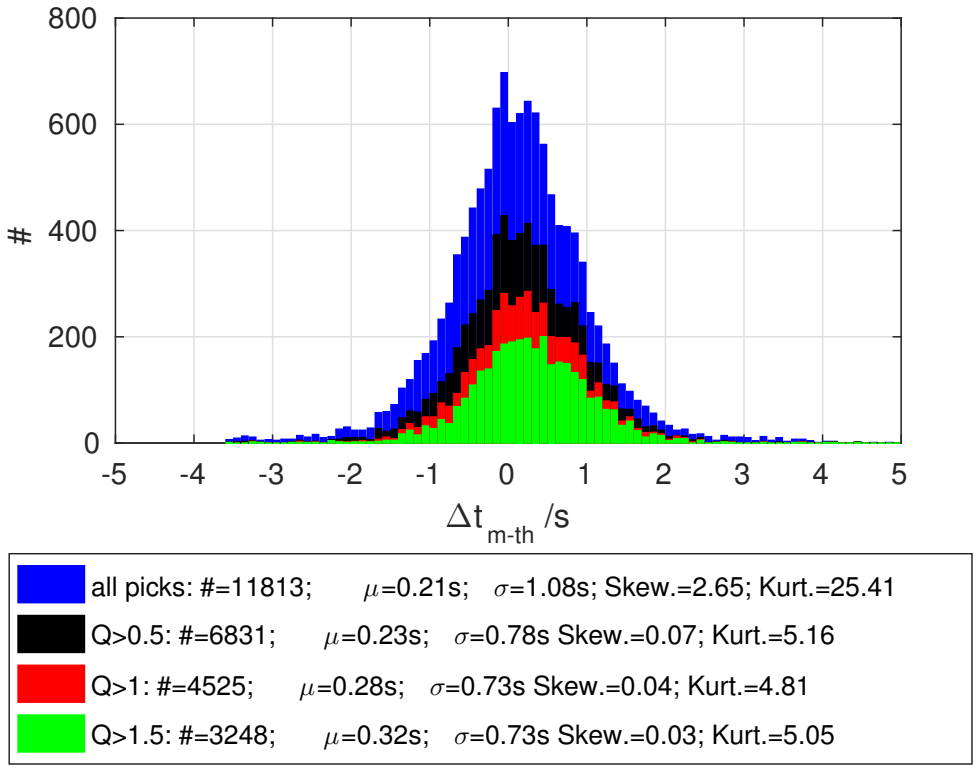

Figure 3.14.: Residuals between manual (ISC, 2016) and theoretical (AK135, Kennett et al., 1995) P-phase onset times. Automatic P-pick qualities are assigned to manual phase onset times.

A high number of arrival times with large residuals are removed by quality restriction. Good quality residuals range between $\pm 1s$ and $\pm 4s$ dependent on the distance (Fig. 3.15). In the distance range from 15 to 25° the late good quality picks might be explained by triplication due to the mantle transition zone, while in larger distances the broader range coincides with a larger total number of picks.

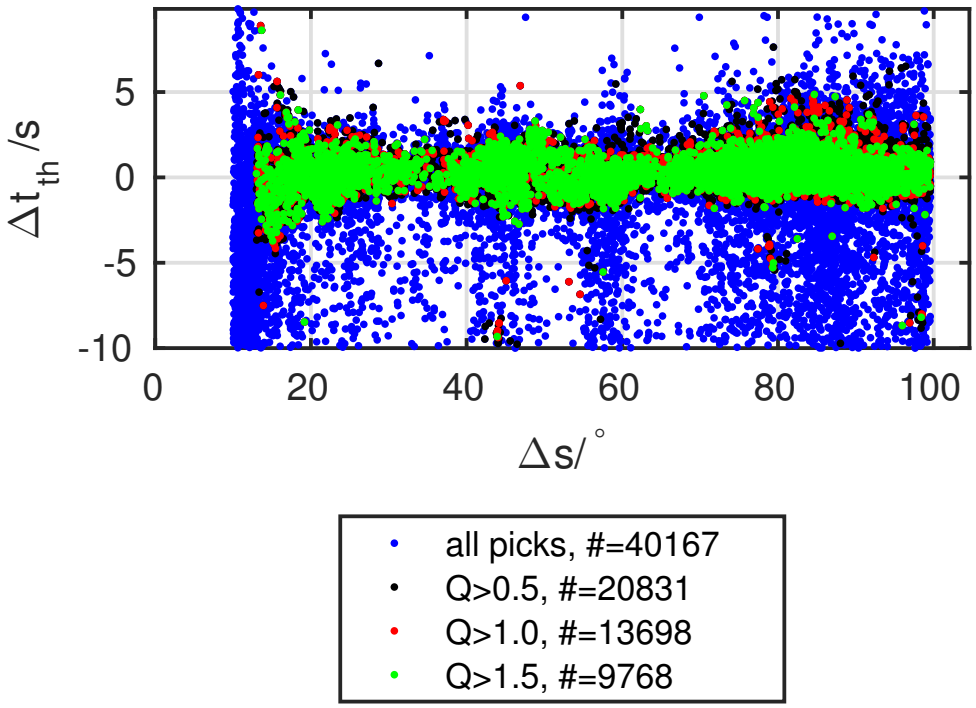

Figure 3.15.: Residual times between automatic picks and theoretical arrival times (AK135, Kennett et al., 1995) against the distance in degree for teleseismic P-phase arrivals. Coloring indicates the minimum quality Q of automatically determined picks in each distribution according to the legend.

In the following, the spatial distribution of residuals between automatic and theoretical phase onset times is discussed (Fig. 3.16). Visible are the station wise mean residuals (top left), standard deviations (top right), number of picks (bottom left) and the percentage of good picks ($Q > 1.5$, bottom right). The mean and standard deviation values are calculated for the automatic P-phase onset times with qualities $Q \geq 1.5$ only, which is the highest quality class considered.

Most stations show mean residual times within $\pm 0.5s$ and standard deviations below $\pm 1s$. This consistent distribution indicates that the picking approach works location independent. The outliers in the mean value map and the standard deviation map, for example the stations IGAD, ZARR, A055, FBE, VITZ and BRNL, coincide with very low absolute numbers of picks which dismisses the interpretability of these stations' values.

The accumulation of stations with negative mean residuals in the center and south-west of Germany as well as of stations with positive residuals in the south east and west of Germany can

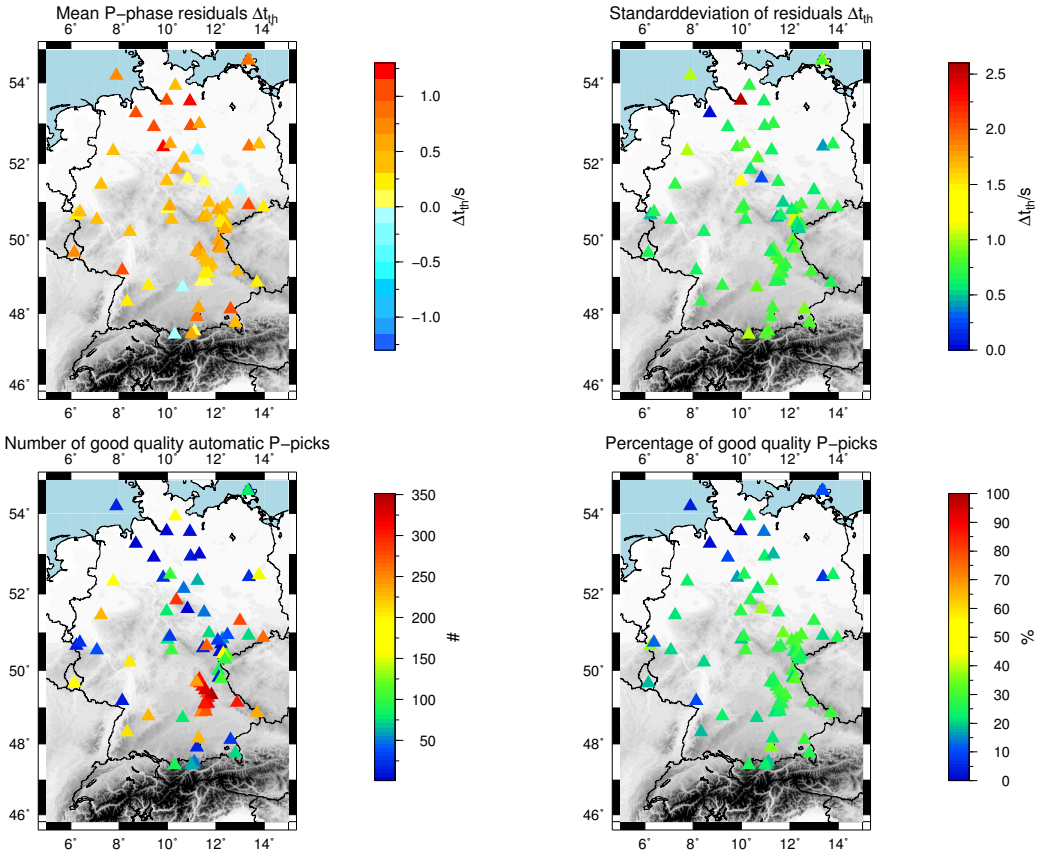

Figure 3.16.: Maps with station individual mean residuals (top left) and standard deviation of the residuals (top right) between automatically determined P-phase onset times and theoretical P-phase arrival times (AK135, Kennett et al., 1995). The lower left image shows the number of compared phase onset times and the lower right gives the percentage of compared phase onset times ($Q > 1.5$) to all determined picks at the stations.

be explained by regional velocity heterogeneity. The percentage of good quality picks appears station dependent. Stations with outstanding low numbers of good quality picks are known for low SNR data, e.g. HLG, HAM3, IGAD and RGN in the North German Basin.

These station specific residuals between automatically determined and theoretical travel times already indicate lateral heterogeneity throughout Germany. Many stations began recording in recent years yielding only low number of picks and the results there are consequently not meaningful.

Applying the same analysis on residuals between manually and automatically determined phase picks reduces the number of interpretable stations further (Fig. 3.17). Note that only good quality picks for which manual phase time readings are available are taken into account.

The mean and standard deviation values show that high quality automatic P-picks tend to be slightly earlier than the manual picks with standard deviations from $\pm 0.2s$ to $\pm 0.6s$. At the stations HLG, FBE and NOTT mean values between $+0.2s$ and $+0.3s$ and large standard devi-

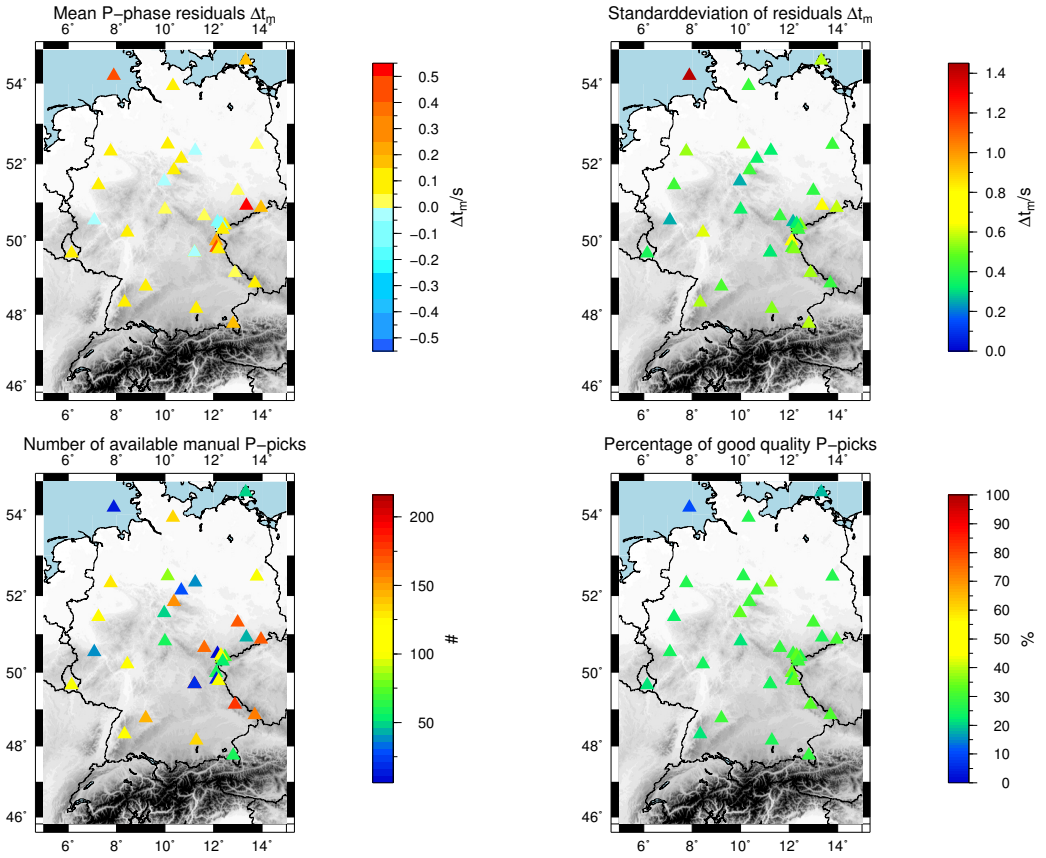

Figure 3.17.: Maps with station individual mean residuals (top left) and standard deviation of the residuals (top right) between automatically determined P-phase onset times and manual P-arrival time readings (ISC, 2016). The lower left image shows the number of compared phase onset times and the lower right gives the percentage of compared phase onset times ($Q > 1.5$) to all determined picks at the stations.

ations above $\pm 0.7s$ can be explained again by the low total number of compared P-phase picks. However, the stations MANZ, NOTT and ROTZ close to the Czech border show high standard deviations for high numbers of compared picks. The absence of such irregularities in other regions and a high percentage of good automatic picks at ROTZ and NOTT raises questions concerning the consistency of the reference manual picks.

The percentages of good quality picks do not vary strongly except for station HLG. Following these results, the residuals appear station independent. For the three outlier stations, it must be clarified whether the differences in standard deviations result from the automatically or rather from the manually determined phase arrival times.

Teleseismic S-phase

Bandpass filtered data of the unrotated horizontal components is considered to automatically determine S-phase arrival times. Before evaluating the spatial station wise results, the quality evaluation and statistical comparison of the whole dataset is discussed. The SNRs of the automatically S-phases are determined using a 10 s signal window.

For both, the SNR of the horizontal components (left) as well as the SNR of the CF (right), the standard deviations of residuals between automatically determined and 1,407 manually read S-wave arrivals (ISC, 2016) decline with increasing SNR values (Fig. 3.18). Note the much larger residual values to manual phase arrival times compared to the P-phase.

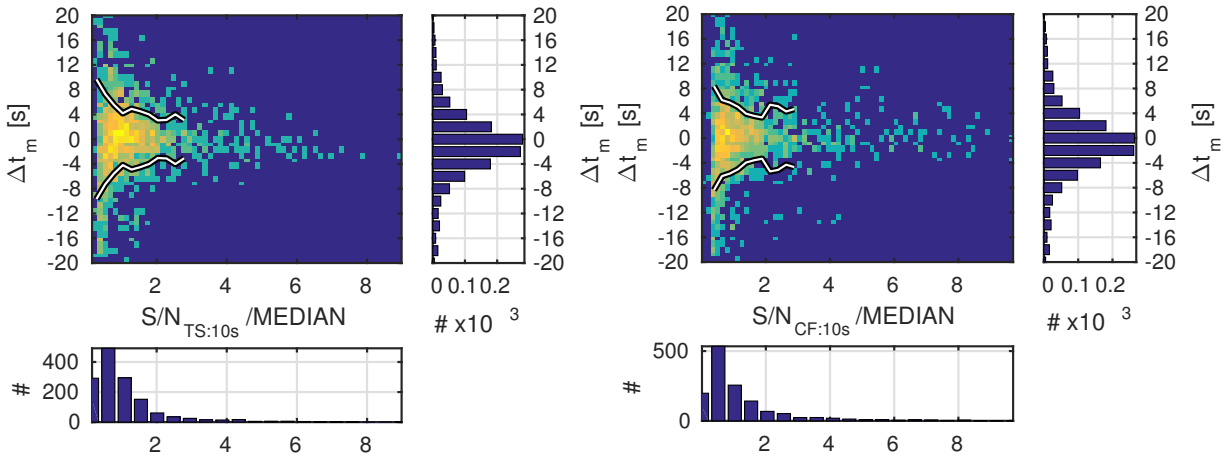

Figure 3.18.: 2D histograms of quality parameters of the S-phase picks. Left: the signal-to-noise ratio is given as a function of the residuals between the automatic and manual picks (ISC, 2016). Red colors indicate large numbers. The white line indicates the standard deviation as a function of the quality measure. Right: the signal-to-noise ratio of the CF is given as a function of the residuals between the automatic and manual picks (ISC, 2016). Red colors indicate large numbers. The white line indicates the standard deviation as a function of the quality measure.

Furthermore, while residual outliers ($\Delta t_m \geq \pm 5s$) are restricted to low quality ranges ($Q < 1.5$), the number of S-wave picks with large SNRs is much smaller than for P-phase picks. Consequently, the majority of picks have median normalized SNRs between 0 and 2.5.

The angle of the slope is fitted to the CF over $15s$ after the automatically determined S-phase pick. Similar to the P-phase, the normalized angles' distribution is stretched over a wider range than the SNRs (Fig. 3.19 right). Although the decline of the standard deviation of residuals between automatically and manually determined arrival times is nearly negligible, the combination of the three quality criteria is a reasonable approach to identify residual since different attributes of the data quality and arrival time appearance in the data are considered.

The quality value Q combined from the SNRs and the angle of the CFs slope is shown in Fig. 3.19 on the right. As already indicated for the individual quality parameters, restrictions of $Q > 1$

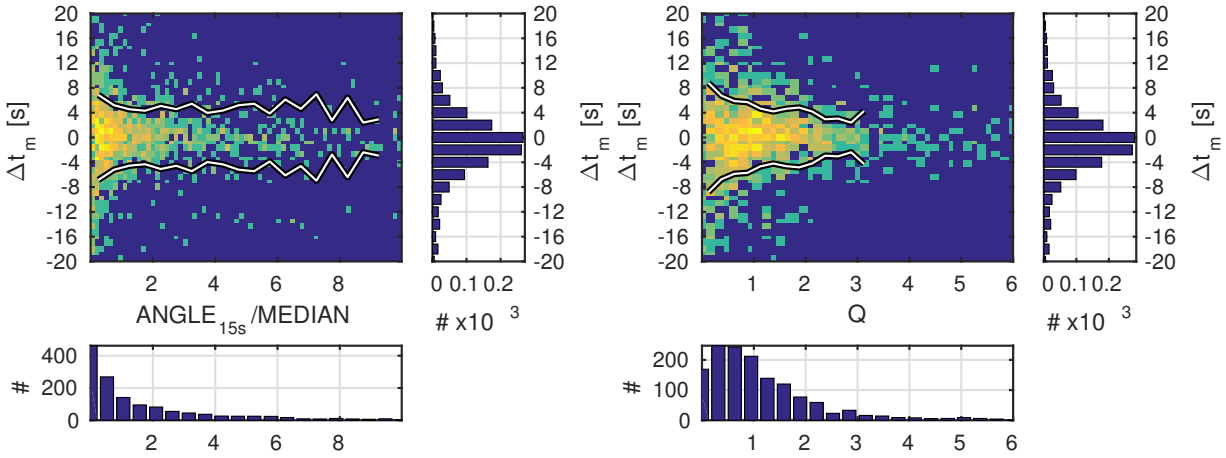

Figure 3.19.: 2D histograms of quality parameters of the S-phase picks. Left: the slope of the characteristic function is given as a function of the residuals between the automatic and manual picks (ISC, 2016). Red colors indicate large numbers. The white line indicates the standard deviation as a function of the quality measure. Right: the average quality is given as a function of the residuals between the automatic and manual picks (ISC, 2016). Red colors indicate large numbers. The white line indicates the standard deviation as a function of the quality measure.

or $Q > 1.5$ already ensure that large residual outliers, especially early automatic S-picks, are removed.

Fig. 3.20 shows the determined S-phase picks' residuals to theoretical phase arrivals (left) and manual S-phase arrival time readings (right). A positive bias is observed for the residuals between automatically determined and theoretical arrival times, similarly to the P-phase. Since the offset occurs for both phases, the one dimensional AK135-velocity overestimates the seismic velocities beneath Germany. The restrictions to different minimum quality levels, remove early automatic S-wave picks ($\Delta t_{th} < -10s$) strictly while a slightly elevated level remains for late automatic S-wave picks ($\Delta t_{th} \geq 10s$).

Comparing less than 1,500 manual phase picks results in a less sharp distribution. Steadily increasing kurtosis values with increasing minimum quality levels are evidence that more outlier residuals are removed than residuals around the mean values. Considering only determined picks with qualities $Q > 1.3$, the residuals are distributed with a standard deviation of $\pm 4.36s$ around a mean of $0.04s$. Since teleseismic S-phases show much more complex waveforms with dominant periods around $T = 10s$ the standard deviation correspond to less than half a signal period.

In Fig. 3.21 the residuals between the 1,415 manual S-time readings and theoretical travel times are shown. Similar to Fig. 3.20 (right) the distributions are shifted to positive residuals with mean values between $+1.52s$ and $+1.81s$. A prominent feature are manual picks which are more than ten seconds later than the theoretical S-phase arrival times. The absence of this feature in the previous histograms suggests strong lateral heterogeneity in a region for which only the few manual phase onset times are available but such a high number of automatic picks that this fea-

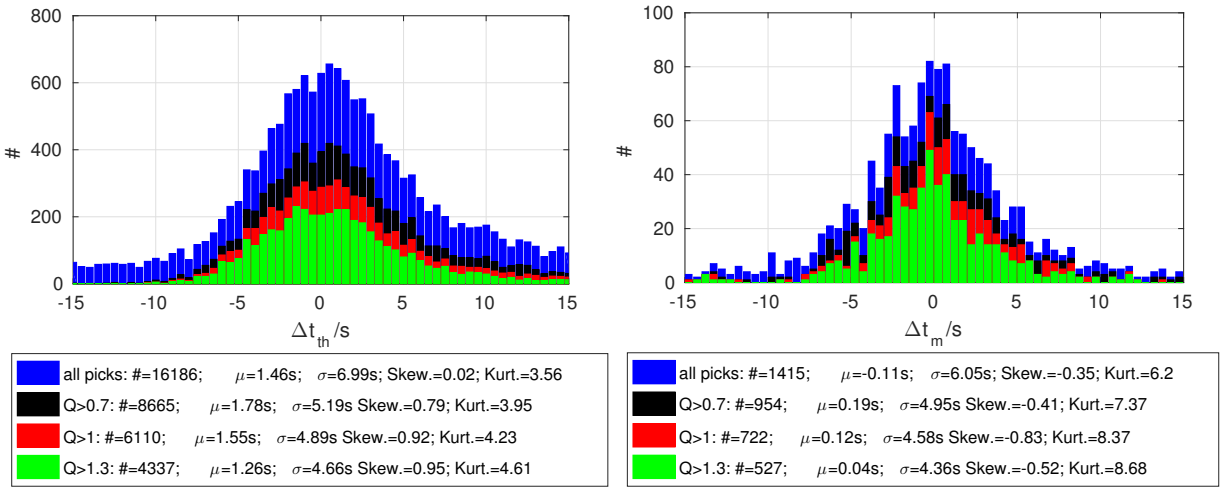

Figure 3.20.: Histograms of residuals between automatic S-phase picks and AK135 - theoretic arrival times (left) as well as automatic and manual S-phase picks (right) (ISC, 2016). Coloring indicates the quality restriction of the distributions picks according to the legend.

ture vanishes in the normal distribution in Fig. 3.20 (left). The standard deviation $\sigma = \pm 5.14s$ is about half a second larger than for the residuals between automatically and manually picked arrival times. This is an evidence that the automatically determined arrival times contain more information on the subsurface than the theoretical arrival times from the model.

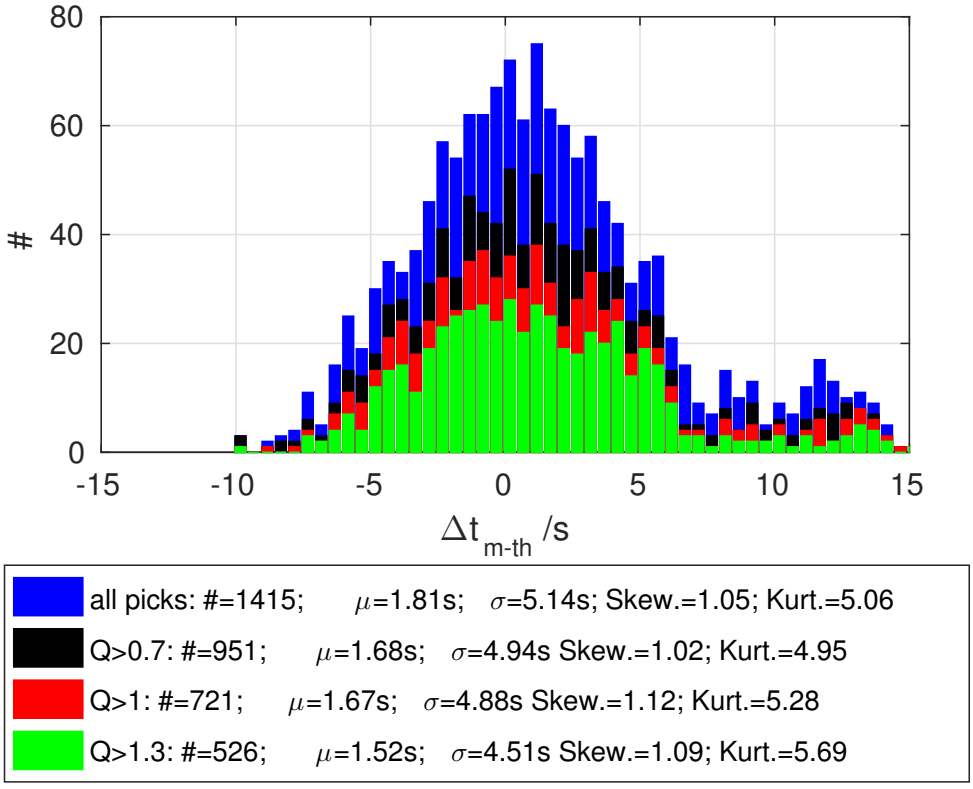

Figure 3.21.: Residuals between manually read (ISC, 2016) and theoretical S-phase onset times (AK135, Kennett et al., 1995).

In triplication distances from 15° to 30° residuals of good quality picks to theoretical arrival times vary up to $+15s$ (Fig. 3.22). Thus, the automatic algorithm picks not necessarily the first of multiple S-phase arrivals at these distances. For epicenter distances larger than 30° the determined picks with qualities $Q > 0.7$ are restricted to $\pm 5s$. More automatic picks in a certain distance range coincide with a larger number of stations and consequently with a stronger variation of residuals to theoretic times. Below approximately 15° low qualities are assigned to all determined S-wave arrival. This can be explained by higher frequency signals for short epicenter distances. In that case, long period noise superpositions the signal whereas the SNR and angle window lengths include longer parts without the actual S-wave signal.

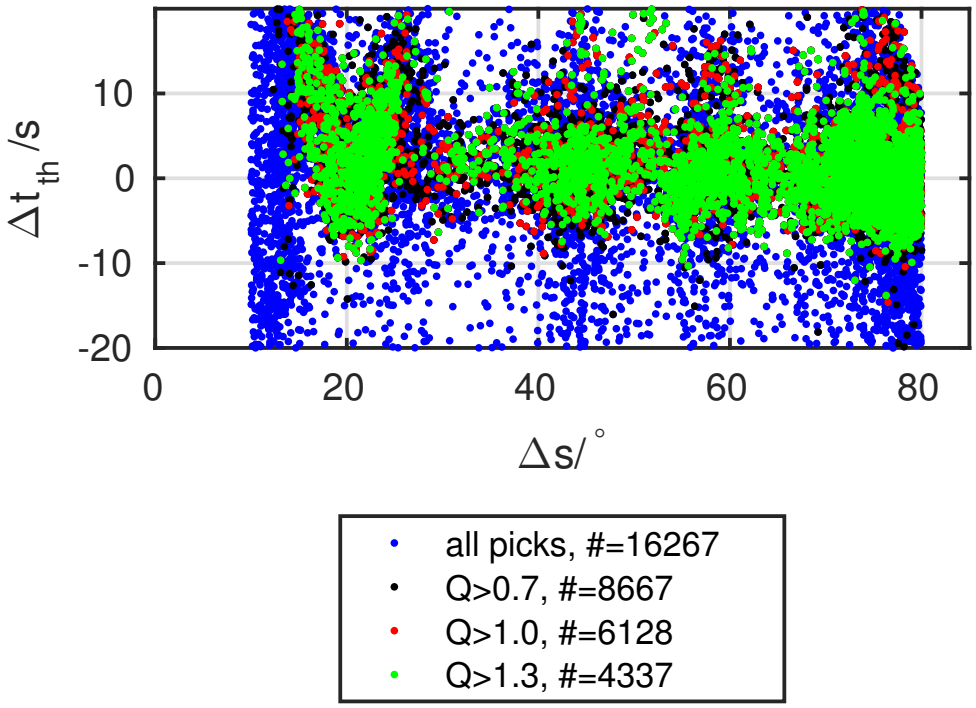

Figure 3.22.: Residual times between automatically determined S-phase picks and theoretical arrival times (AK135, Kennett et al., 1995) against the epicenter distances in degree. The colors indicate the minimum quality levels of the automatic picks according to the legend.

An analysis of the station specific residuals between the determined and theoretical S-phase onset times shows a tendency of the algorithm to pick after the theoretical time at all stations except IGAD (Fig. 3.23). In consistency with the identified offset in the overall residual distribution of P- and S-phase, it confirms that the AK135-model is overestimating velocities beneath Germany.

Mean values larger than $2.5s$ in Western and Eastern Germany can be explained by regional velocity heterogeneity in the crust and upper mantle. The outliers in the mean values and standard deviation coincide with low numbers of good quality picks.

Dismissing these outliers, the picked phase arrival times are found after the theoretical times at all stations within standard deviations around $\pm 5s$. The percentage of good picks varies strongly

but again noisy stations are distinct with very low percentages, e.g. LDAU, HLG and IGAD. As a conclusion, for the S-phase the influence of lateral heterogeneity is visible in the residuals to theoretical phase onset times for regional clusters of stations. The spatial variance of standard deviations is due to the low numbers of considered S-wave arrival times.

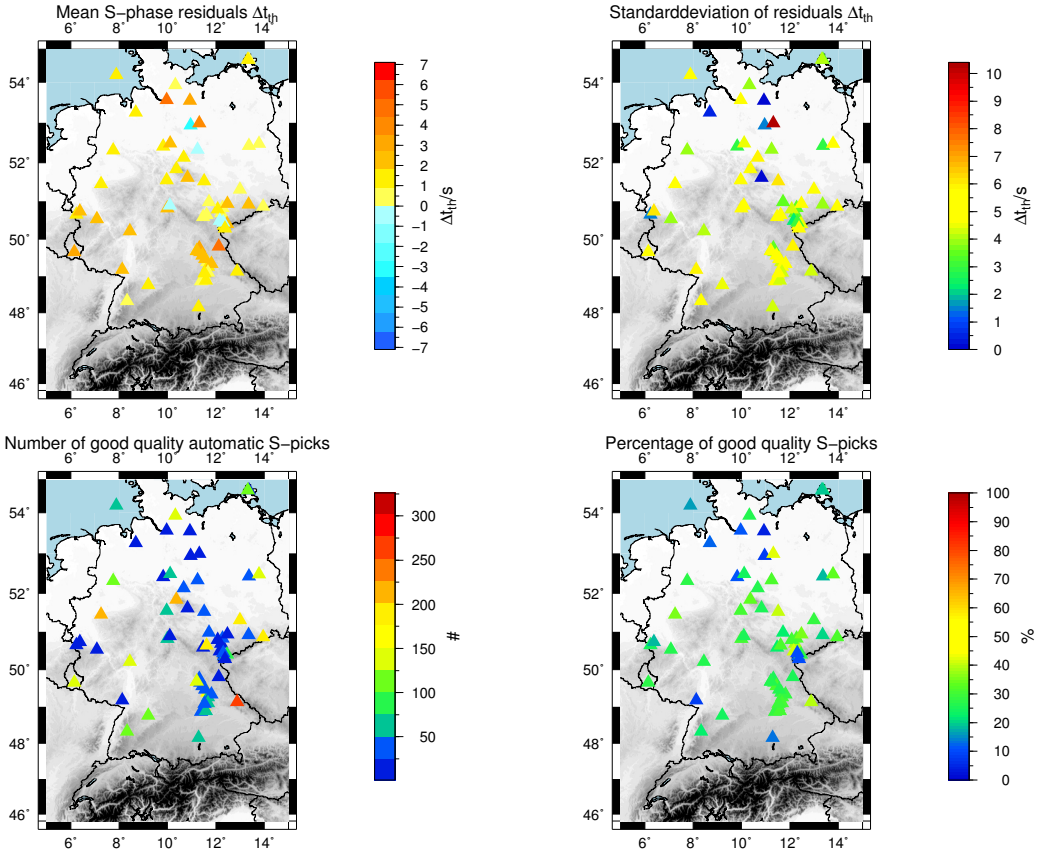

Figure 3.23.: Maps with station individual mean residuals (top left) and standard deviation of the residuals (top right) between automatically determined S-phase onset times and theoretical S-phase arrival times (AK135 , Kennett et al., 1995). The lower left image shows the number of compared phase onset times and the lower right gives the percentage of compared phase onset times ($Q > 1.3$) to all determined picks at the stations.

The same plots for the residuals between the determined good quality and the corresponding manually read S-phase arrival time readings is shown in Fig. 3.24. While the residuals' distribution over the whole network is unbiased (Fig. 3.20 right), the individual stations show residual mean values ranging from $-4s$ to $+3s$. Since the number of compared S-wave arrival times are less than 60 picks per station, the standard deviations are highly variable from $\pm 0.5s$ to $\pm 7s$. 30% to 90% of all determined automatic S-wave arrival times are evaluated reliably.

The rotation of horizontal components to radial (R) and transversal (T) components is often carried out in order to determine S-wave arrivals. It is argued that the rotation improves the SNR. However, the rotation can only be carried out if the earthquake is already located and thus it is only reasonable in post-processing applications.

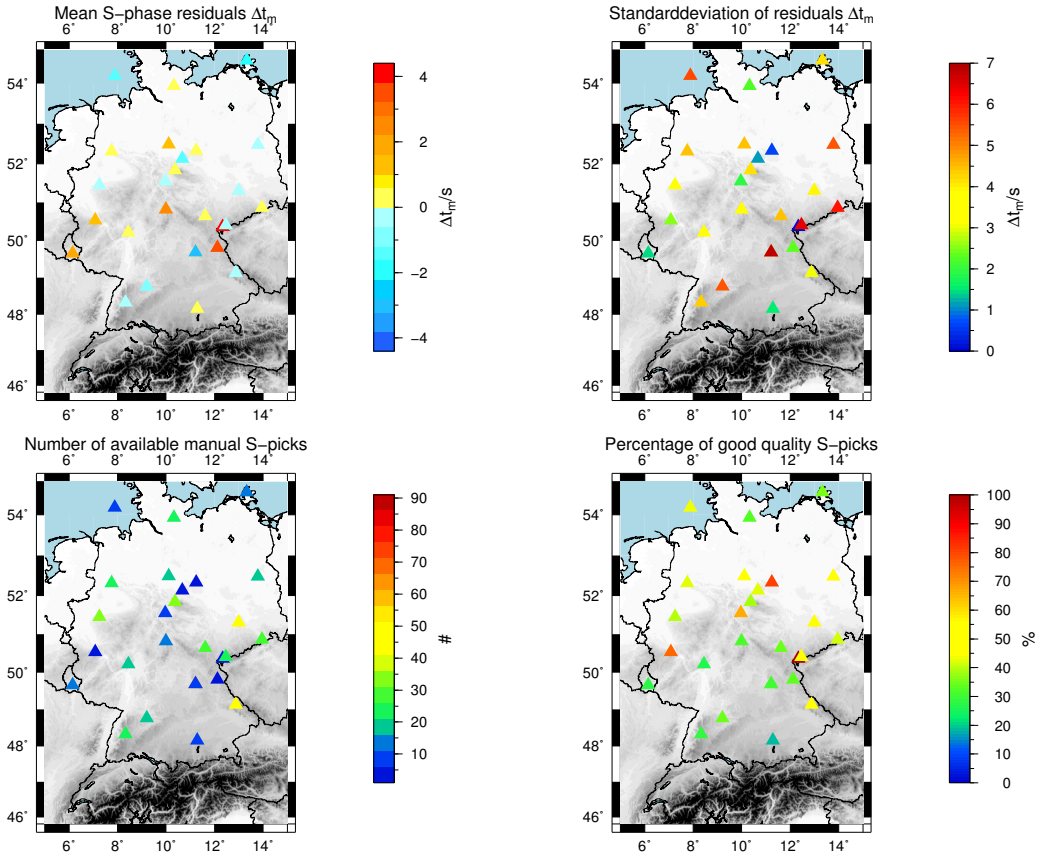

Figure 3.24.: Maps with station individual mean residuals (top left) and standard deviation of the residuals (top right) between automatically and manually determined S-phase onset times (ISC, 2016). The lower left image shows the number of compared phase onset times and the lower right gives the percentage of compared phase onset times ($Q > 1.3$) to all determined picks at the stations.

Nevertheless, comparing automatically determined S-wave picks on unrotated horizontal as well as rotated components shows that no systematic shift is observed (Fig. 3.25). High peaks at the centers of both distributions prove that most S-picks are identical or nearly identical whether determined on the R-, T- or the unrotated components. Although, a shift of $-0.26s$ of the residuals' mean value is observed for the T-component, this values appears negligible low compared to standard deviations of residuals to manual phase time readings and automatically picked arrival times (Fig. 3.20).

Finally, the determined P- as well as S-wave picks appear unbiased regarding the manual reference picks, while station dependent differences are identified. Overall, the residual distributions indicate that the algorithm performs numerically stable and the determined picks are reliable. However, this is validated by applying an accumulated catalog of manual arrival time readings which can hardly be rated a consistent reference database.

Furthermore, declining standard deviations and increasing kurtosis with larger quality restric-

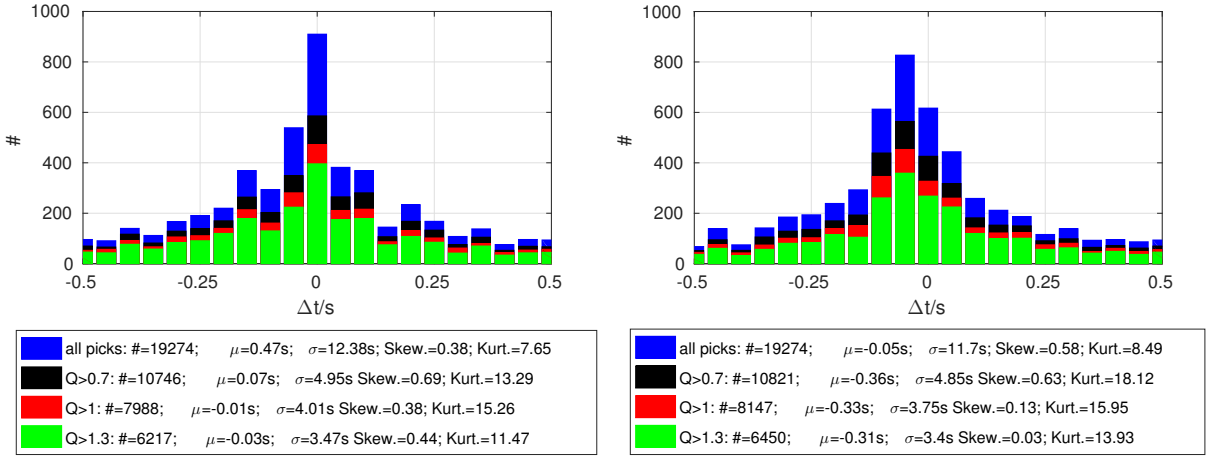

Figure 3.25.: Residuals between automatically determined S-wave picks on the E- and N-components and automatically determined S-wave picks on the radial component (R-component) (left side) as well as automatically determined S-wave picks on the transversal component (T-component) (right side). The colors indicate the minimum quality of the compared S-picks.

tions prove the good performance of the quality evaluation. These restrictions remove automatically determined picks with low residuals to manual phase time readings as well. A comparison of S-wave picks determined on rotated and unrotated components indicates that the algorithm performs rotation independent.

Before continuing with the application to induced seismicity a variation of filter bands is briefly discussed.

3.3.3. Filter dependency and component rotation

Seismic phase travel times are expected to be frequency dependent. Phase time picking assumes an infinite-frequency wave for which the arrival time depends solely on the velocity along the single line ray path. Finite-frequency theory provides another approach, which describes sensitivity of wave phase velocity to off-path heterogeneity by Fréchet Kernels (Dahlen et al., 2000). This takes waveform scattering and diffraction into account and is therefore more powerful than the ray theory (Shen, 2006).

In order to examine a frequency dependency of automatically determined phase arrival times, the picking procedure is applied using different filter frequency bands for both teleseismic P- and S-phases. Automatic P-wave arrival times are determined using three filter frequency bands: high frequency band (0.25-3 Hz), low frequency band (0.03-0.1 Hz) and a broad bandpass filter (0.03-3 Hz). The high frequency band P-picks show no bias $\Delta t_{th} < 0.1s$ to the broadband reference with variations of $\sigma = \pm 0.51s$ (Fig. 3.26). In contrast, the distribution of P-picks determined in the low frequency band are systematically shifted by $+1s$ with a standard deviation

of $\sigma = \pm 0.99s$. Although an arrival time shift with frequencies is expected from finite frequency effects and damping, it must be considered that the picking parameters have not been readjusted for the different frequency bands and hence may introduce errors.

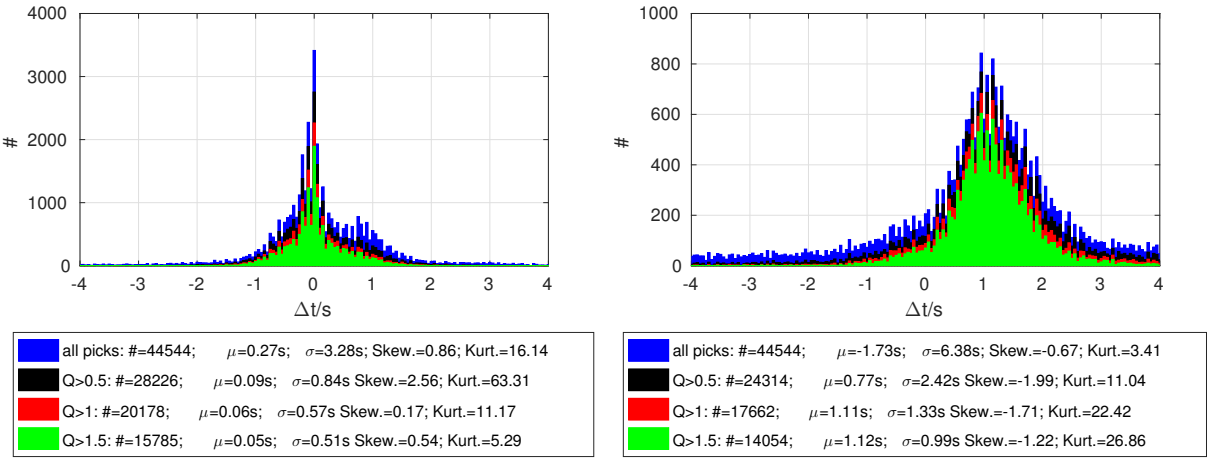

Figure 3.26.: Residuals between automatic P-picks determined in the high (0.25-3 Hz, left side) as well as low (0.03-0.1 Hz, right side) frequency bands to the broadband dataset (0.03-3 Hz). The colors indicate the minimum quality of the compared automatic picks.

A direct comparison of P-picks determined in the high frequency band to the automatic picks determined in the low frequency band provides a similar distribution bias as the broadband (Fig. 3.27). The high frequency automatic P-picks are usually determined earlier than the phase onset times in the low frequency band by an average of $-1.55s$. The quality restriction for this comparison removes especially residuals in the positive range ($> +2s$). Thus, the expected shift of phase arrival times becomes more distinct for the direct comparison of non-overlapping frequency bands.

For the S-phase a bandpass filter from 0.03 to 1 Hz, which overlaps with the primary (0.05-0.1 Hz) and the secondary (0.2-0.4 Hz) oceanic microseism, is applied above. The oceanic microseism can produce significant noise in seismic recordings. A similar comparison of S-wave arrivals determined applying a high frequency band filter from 0.25 to 1 Hz (above oceanic microseism), a low frequency band filter from 0.03 to 0.1 Hz (below oceanic microseism) and the reference broadband from 0.03 to 1 Hz dataset is performed (Fig. 3.28).

In consistency to the automatically determined P-wave picks, the residuals' distribution is shifted stronger for the low frequency band. However, the mean values in both cases are positive between $+1s$ and $+3s$.

Fig. 3.29 shows the residuals between automatic S-phase picks determined in the low frequency band to automatic picks determined in the high frequency band. A negative bias ($\approx -1s$) is visi-

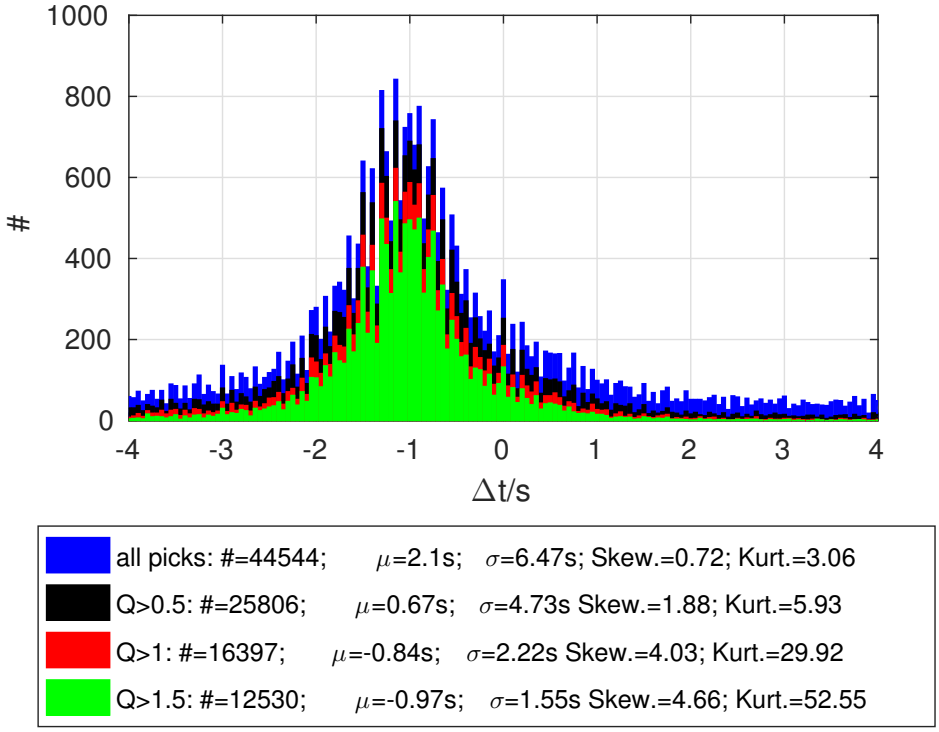

Figure 3.27.: Residuals between automatic P-picks determined in the high (0.25-3 Hz) and in the low (0.03-0.1 Hz) frequency bands. The colors indicate the minimum quality of the compared automatic picks.

ble indicating that the phase arrivals are picked earlier in the high frequency band. Furthermore, the variance or residuals is large even for good quality picks. Applying the quality restriction reduces the residuals' mean value from $-4.83s$ to $-0.94s$.

Summarizing, a strong frequency dependency is observed. The observed frequency shifts are approximately $-1s$ from teleseismic P-phase picks at 0.25-3 Hz with respect to teleseismic P-picks at 0.03-0.1 Hz as well as from teleseismic S-wave picks 0.25-1 Hz with respect to 0.03-0.1 Hz.

Although the phase arrival time picking is originally based on an infinite-frequency approximation, consistent automatic picking appears to be a useful tool to observe the phenomena. The results, however, are not sufficient to define absolute frequency dependent relative times since it is difficult to distinguish between the picker-dependent sensitivity to high frequencies and the actual shifts due to frequency-dependent travel times. To quantify the actual travel time shift a set of manual reference picks in the individual frequency bands must be determined. The automatic picks determined here can provide a selection of arrival times worth looking at by quality and residuals. If the offset is verified, it may be possible to systematically analyze spatial frequency dependent damping.

Nevertheless, an absence of high frequency signal parts may significantly vary results of the au-

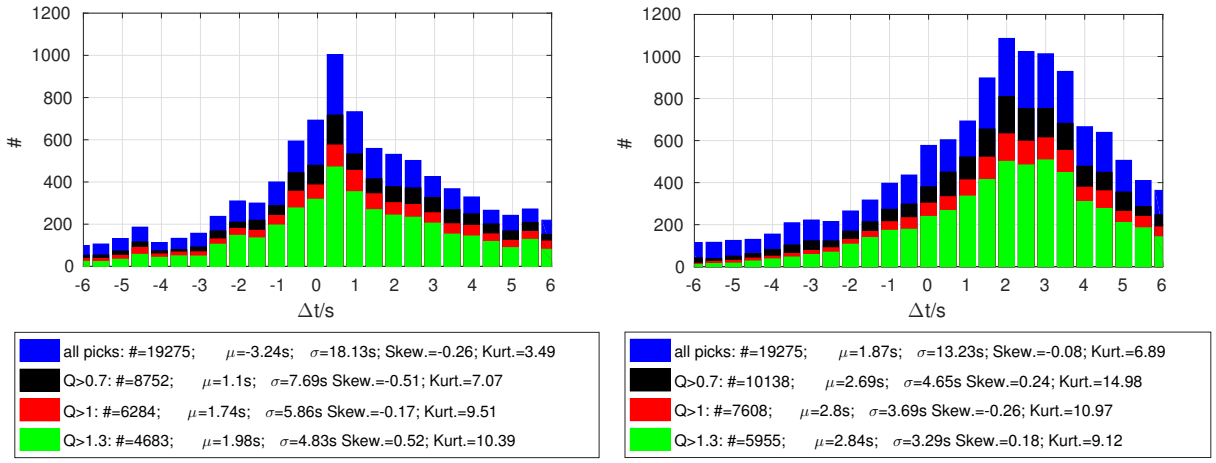

Figure 3.28.: Residuals between automatic picks determined in the high (0.25-1 Hz) (left side) as well as low (0.03-0.1 Hz) (right side) frequency bands to the broadband dataset (0.03-1 Hz). The colors indicate the minimum quality of the compared automatic picks.

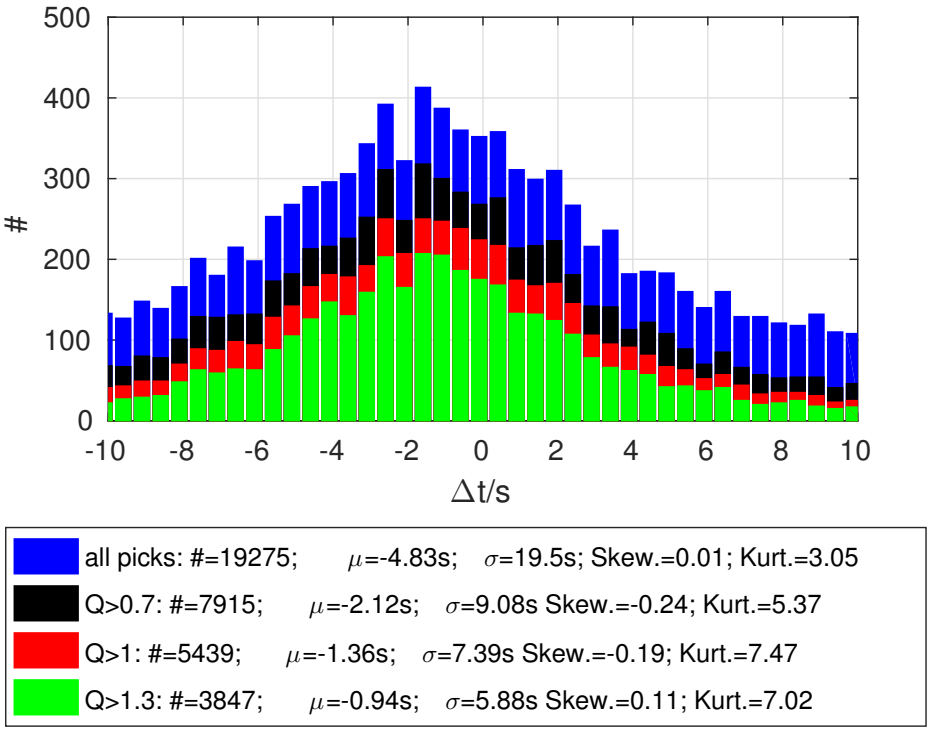

Figure 3.29.: Residuals between automatic S-picks determined in the high (0.25-1 Hz) and in the low (0.03-0.1 Hz) frequency bands. The colors indicate the minimum quality of the compared automatic picks.

tomatic picking algorithm, if the parameters are not adjusted. In consistency to the filtering band the noise frequency changes. An increase of the AR-determination and -prediction windows lengths is thus required in order to predict the noise patterns properly. Furthermore, small

scale CF variations are expected to be stretched to more long-periodic undulations requiring a review on the meaningfulness of the "waterlevel". For the SNR determination, the maximum value of the signal amplitude in a given time after the arrival time is considered. Hence, while the determination of the SNR is only slightly time window length dependent, the slope of the CF is highly sensitive to the length of the window over which it is fitted. In case of low frequency bands, much longer time windows must be selected in order to evaluate the CF slope of the actual phase arrival. Therefore, a careful selection of parameters dependent on the applied filtering is recommended.

Finally, these variations point out an important feature in accumulated catalogs of manual arrival time readings. Different agencies and even processors in individual agencies determine phase arrival times by applying customized parameters and filter settings. Consequently, it is problematic to access the reliability of individual picks if not all parameters are provided. In order to investigate these observations further consistently determined manual time readings with transparent reading settings in different filtering bands are required. It could be useful to use arrays or close-by stations to determine relative arrival times at neighboring stations to check the consistency of determined arrival times. For applications with large station separations like global body wave tomography, the absolute arrival time data picking is important and a study including automatic and manual picks and comparing tomographic results could give answers how strong the picking errors influence the results considering other error sources (e.g. locations errors).

3.4. Application to induced seismicity

After showing good performance on global scale seismicity, the algorithm is applied to the local induced seismicity recorded around Landau and Insheim. Before results of automatically picked arrival times are presented and discussed, the database is introduced and a picking parameter optimization for this example is discussed.

3.4.1. Local induced database

Situated on the western margin of the URG, the geothermal reservoirs Insheim and Landau are located in a complex tectonic environment. The Landau geothermal power plant has been operating since 2007 while the Insheim plant has been started in 2012. Both reservoirs, which are approximately 5 km apart, show continuously occurring seismicity below magnitudes of Ml2.7 in Landau and Ml2.1 in Insheim.

692 induced earthquakes between 2009 and 2016, taken from the catalog by the monitoring company Bestec GmbH (pers. comm. Dr. L. Küperkoch, Bestec GmbH, Landau i.d. Pfalz, Germany), are considered. 296 of these are located at the Landau reservoir and 396 at the Insheim reservoir. As the operating and monitoring company of the Landau power plant changed in 2014, the event catalog contains Landau events only up to 2014. For the Insheim reservoir, only well located events are considered. The event locations and magnitudes reported in the catalog are shown in Fig. 3.30. Since the Insheim events have been reprocessed and an improved minimum 1D-velocity model has been developed by the Bestec GmbH, locations are much less spread than at the Landau reservoir (pers. comm. Dr. L. Küperkoch, Bestec GmbH, Landau i.d. Pfalz, Germany).

As discussed in the previous chapters, few natural earthquakes occur in the region. The number of stations in the area surrounding Landau and Insheim increased since the Ml2.7 event occurred at the Landau reservoir in 2009. Increasing from a single station before 2010, now up to 50 seismic stations are recording simultaneously within 15 km around both power plants. Hypocenter locations from routine processing do not outline fault systems or clusters while both reservoirs can be seismically distinguished. Epicenters spread approximately 3 km around the Landau and 1 km around the power plant locations. The majority of detected events have magnitudes below Ml1 although individual events larger than and up to Ml2 occur occasionally.

Similar to the teleseismic application, theoretical wave arrival times are calculated. The software Hypomod (Schweitzer, 1997, 2001) is applied using the local 1D-velocity models for Landau (Bönnemann et al., 2010) and Insheim (pers. comm. Dr. L. Küperkoch, Bestec GmbH, Landau i.d. Pfalz, Germany). Around these arrival times symmetric time windows of $\pm 5s$ are placed in which the picking algorithm is applied. In the following, the induced P- and S-phases are referred to as P1- and S1-phase, indicating that the determined picks are the first arriving P- and

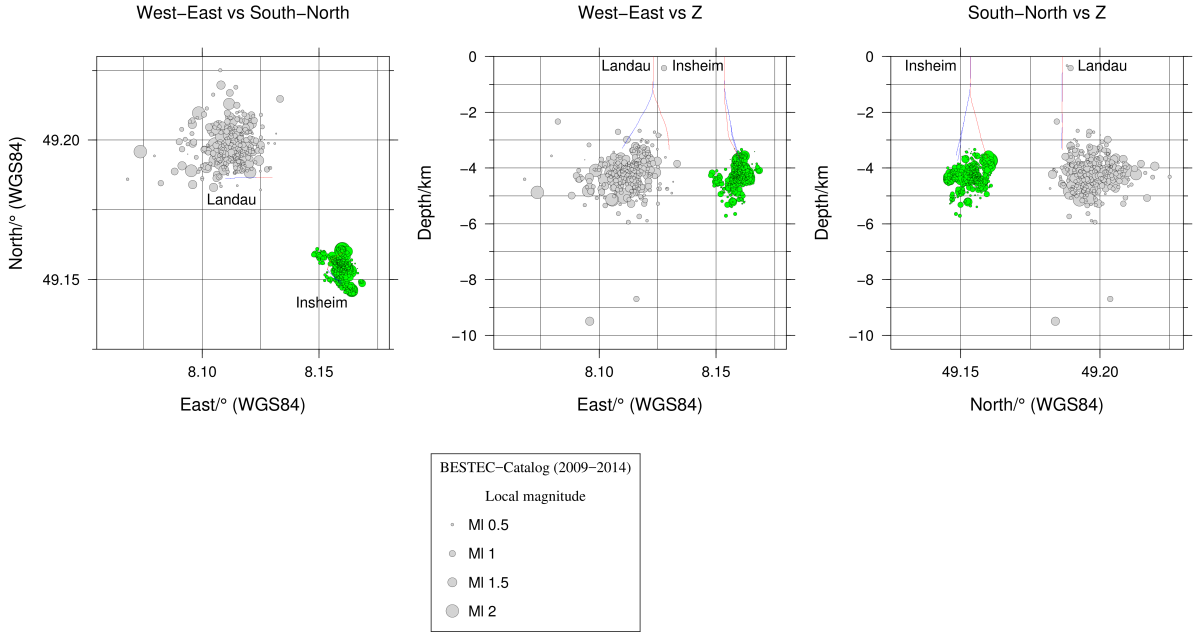

Figure 3.30.: Locations and magnitudes of induced seismicity at the Landau (gray) and Insheim (green) geothermal reservoirs (Bestec catalog). Injection and production wells of the Insheim and Landau power plants are shown as blue and red lines.

S-phases. Furthermore, a dataset of manually read phase arrival times for P1- and S1-phases are considered as reference times. The manual phase arrival time readings are obtained by a single processor using constant filter settings for each phase (pers. comm. Dr. L. Küperkoch, Bestec GmbH, Landau i.d. Pfalz, Germany). Hence, it provides an excellent reference dataset to evaluate the automatically determined phase arrival times. For the precise relocated events at Insheim, between 16 and 72 manual P1- and S1-picks are available per event.

3.4.2. Parameter optimization

Before applying the algorithm to the induced seismic dataset a systematic parameter optimization is carried out. Since the Insheim dataset provides more events and manual arrival times, it is selected as reference database for the optimization.

While the AR prediction and its parameters are discussed in various studies (e.g. Küperkoch et al., 2012; Leonard and Kennett, 1999), the cost function weighting provides a simple optimization opportunity for different datasets. As discussed in section 3.2.3, the different cost function parameters $C_{1,2,3}$ (see eq. 3.3,3.4,3.5) characterize different aspects of the waveforms or its transformations.

For the purpose of optimizing the cost function weighting, the algorithm is applied repetitively with changing weighting parameters $w_{1,2,3}$ (see eq. 3.3,3.4,3.5). Measure of goodness for each setting is the distribution of residuals between determined and reference manual phase time

readings. Aim is to reduce the residuals standard deviation around mean values of 0s. However, before optimizing the cost function weighting, the quality calculation windows are optimized.

The SNRs and the CFs slope are calculated using time windows of predefined lengths. In case of the SNRs the signal amplitude is calculated as maximum of the waveforms' root-mean-square amplitudes or the CF amplitude within a predefined time window of length Δt_{SNR}. Consequently, the length of this time window should be adapted to varying signal lengths over the dataset.

Similarly, the window length over which the slope is fitted to the CF is the second parameter which is optimized here. Since it shall evaluate the impulsiveness, the fitting-window must be long enough to avoid minor undulations of the CF, yet short enough to not consider low CF amplitudes following the phase waveform.

Expecting that the manual phase arrival times evaluated as most reliable coincide with impulsive waveforms, the quality measures are repeatedly calculated for manually read P1- and S1-picks from the Bestec catalog. Only picks with the lowest assigned uncertainties of $\epsilon = \pm 0.04s$ are considered. The right side plots in Figs. 3.31 and 3.32 show the median SNRs of waveforms around 3,000 manually determined P1- and 2,000 S1-phase arrival times for different signal window lengths. Concluding from the curves running against saturation values a window length of 0.5 s is selected.

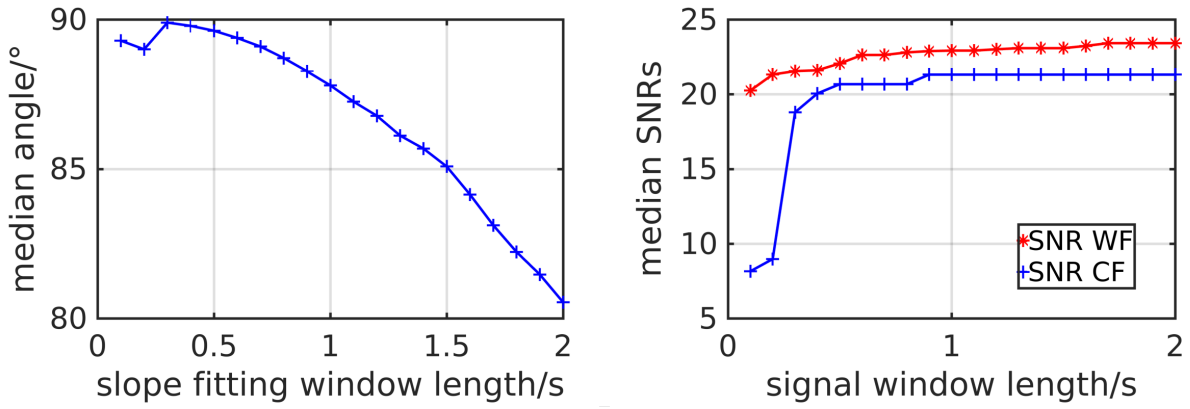

Figure 3.31.: Left plot: Median angle of slopes fitted to CF after good quality manual P1-wave arrival time readings over different time window lengths (left side).
Right plot: Median signal-to-noise ratio of the waveforms (WF) and CF around the good quality manual P1-wave arrival time readings calculated over different signal window lengths.

In corresponding manners, the test is carried out for the window length of slope fitting (left side plots in Figs. 3.31 and 3.32). The curves increase until window lengths of 0.3s. Consequently, the maximum P1-waveform amplitude is reached within 0.3s after the phase time readings, which is selected as slope fitting window length.

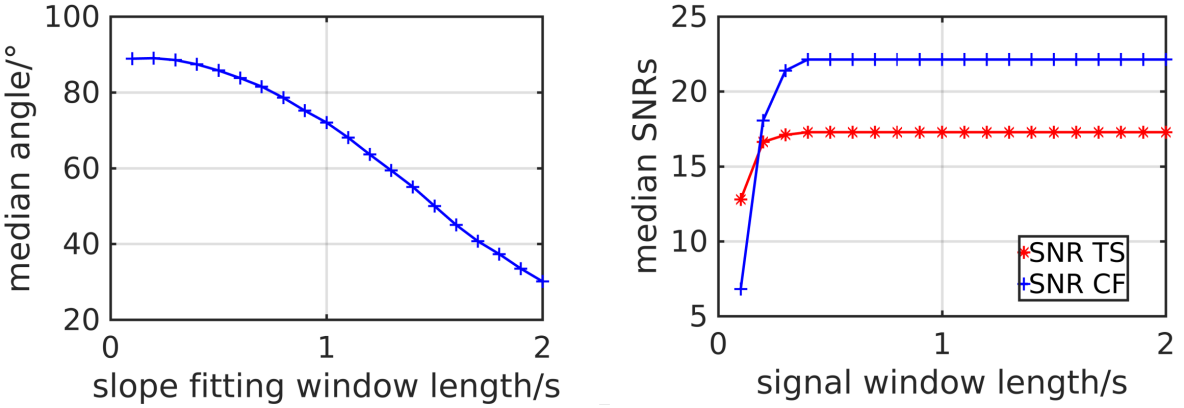

Figure 3.32.: Left plot: Median angle of slopes fitted to CF after good quality manual S1-wave arrival time readings over different time window lengths (left side).
Right plot: Median signal-to-noise ratio of the waveforms (WF) and CF around the good quality manual S1-wave arrival time readings calculated over different signal window lengths.

Steadily decreasing median slope angles and a SNR value saturation after short time window lengths, indicates that the S-waves of the Insheim events show impulsive waveforms. Although the maximum is found at the shortest window length of $0.1s$, a fitting length of $0.3s$ is selected to avoid false weighting due to small scale CF undulations. At a signal window length of $0.4s$, both SNRs reach their saturation levels. Consequently, it is the selected signal window length for automatic S1-wave picking.

As discussed in the previous chapters, other parameters are sensitive to different frequency bands of considered data. Adopting the frequency bands applied in manual processing, the AR-parameters are empirically adjusted. It is found, that the picking results of induced seismicity are not very sensitive to variations of the AR-parameters in such high frequency ranges (1-25/30 Hz).

After determining reasonable quality calculation window lengths, the automatic picking cost function parameters are optimized. For this purpose, arrival times are determined automatically and for each pick a single quality Q is calculated according to equ. 3.6.

Applying these quality values only reliable automatic picks are compared to reference manual picks in order to optimize the cost function weighting. Between 60% and 80% of the determined automatic picks are evaluated reliable for the comparison. For both, the P- as well as the S-phase arrivals, a shift towards later mean residuals and decreasing standard deviations correlates with increasing CF "waterlevels" w_1 (Fig. 3.33). In comparison, the weighting of the AIC-residual penalty (w_2) and the low-gradient penalty (w_3) have similar yet less strong effects. The grid-searches using alternating w_3-settings are provided in Appendix B.

Parameter combinations which result in mean values close to zero and low standard deviations are optimal settings for the picking procedure. Within an accepted mean value range $-0.02s \leq \Delta t_m \leq +0.02s$ the minimum standard deviation decides which weighting parameter

combination is selected. For the P1-phase these are $w_1 = 1.5$, $w_2 = 0.5$ and $w_3 = 0.5$ and for the S1-phase $w_1 = 1.2$, $w_2 = 0.5$ and $w_3 = 0$ are found to provide a desirable residual distribution.

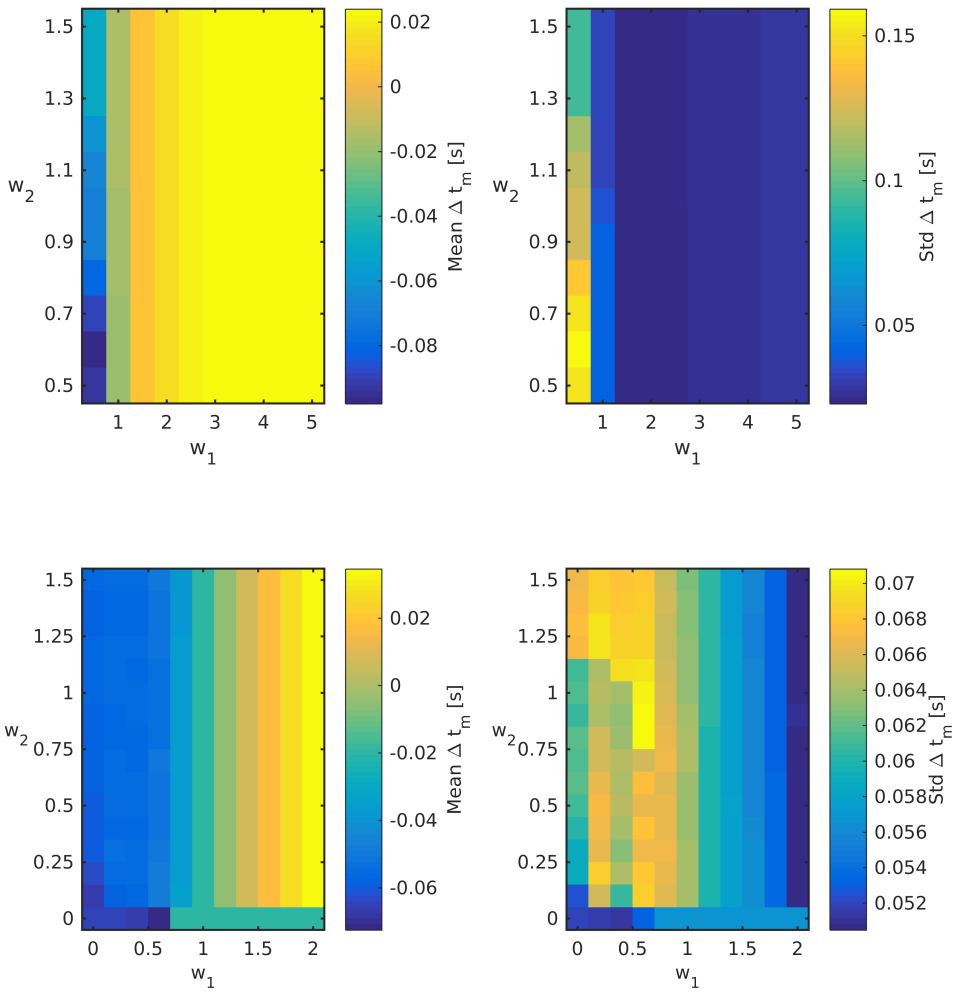

Figure 3.33.: Means and standard deviations of residuals between manually picked reference phase arrival times and automatic P1-(top panels)/S1-phase picks (bottom panels) determined by applying different cost function weightings w_1, w_2, $w_3 = 0.5$ (top) and $w_3 = 0$ (bottom).

3.4.3. Results

After introducing the dataset and selecting the best parameter combinations, the AR-AIC-costfunction picking approach is applied to the complete Insheim and Landau event catalog. A total number of about 40,000 phase arrival times are processed. In this section the automatically determined induced seismic phase arrivals are presented and compared for different quality levels against the reference database of manual phase time readings. First the distributions of qualities and residuals to manual reference time readings are discussed for Insheim and Landau, respectively.

For the Insheim P1- and S1-arrival times a distinct decrease of large residuals between automatically determined and manually read arrival times with increasing qualities Q is observed (Fig. 3.34 and 3.35).

The white lines, indicating the residuals' standard deviations, show a steadily decreasing slope towards lower residuals in both cases. Automatically determined P1-picks which are too late ($\Delta t_m > 0.1s$) are limited to qualities $Q \leq 3$ while too early determined P1-picks are found up to qualities ($Q \leq 8$). The P1-picks are separated into two quality ranges separated by a gap between $Q \geq 0$ and $Q = 0.5$.

A broader distribution of residuals for the S1-picks is justifiable by lower filter frequencies and ergo longer periods as well as more complex, partially emergent waveforms and S-wave splitting. The lower histograms indicate that a high number of automatically determined phase arrival times receive low quality values while the histograms on the right side show that the vast majority of automatic picks are within $\pm 0.1s$ to the manual phase time readings. Again a gap of automatic pick qualities around $Q \approx 0.5$ is observed although it is less distinct than for the P1-phase. These distributions verify on the one hand high precision of the picking algorithm and show on the other hand a very strict quality evaluation.

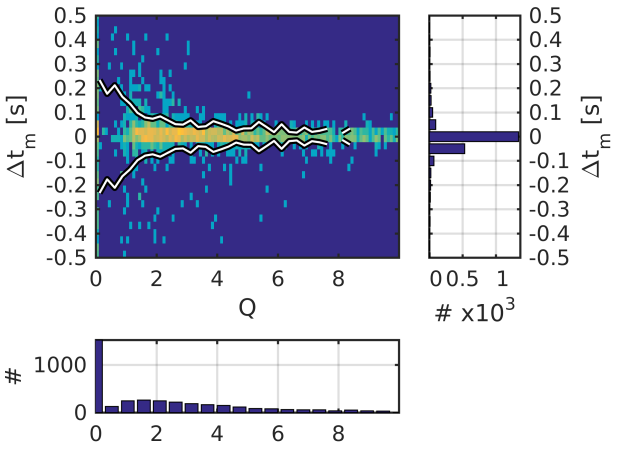

Figure 3.34.: 2D-histogram of residuals between automatic and manual P1-picks vs. automatic pick qualities for the Insheim dataset. The white line shows the residuals standard deviation.

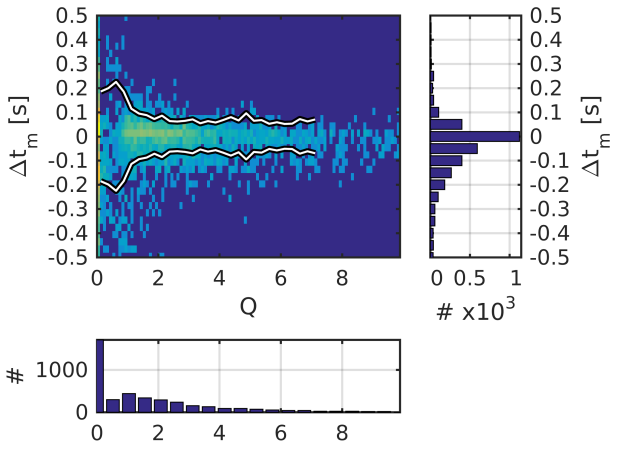

Figure 3.35.: 2D-histogram of residuals between automatic and manual S1-picks vs. automatic pick qualities for the Insheim dataset. The white line shows the residuals standard deviation.

Using the quality evaluation to identify reliable arrival times requires a comparison of residual distributions for different minimum quality levels.

The 2D-histograms (Fig. 3.34) indicate that the majority of picks have qualities less than $Q = 0.5$ and the residuals to manual picks vary beyond $\Delta t_m = \pm 0.5s$. As a result, the distribution of

residuals between automatically determined and manually read P1-arrival times changes only negligible from $Q \geq 0$ and $Q > 1$ (Fig. 3.36). Applying even stricter minimum quality levels results in a slight decrease of residuals' standard deviations down to $\sigma = \pm 0.02s$ and increasing kurtosis (18.63).

Although the distribution is broader and a long tail towards negative residuals is visible for S1-picks, the same distribution behavior is observed with increasing quality restrictions. It shows a tendency that S1-wave picks are determined before the manual reference times. Since the S-waveforms are usually more complicated and S-wave splitting observable for the induced seismicity, it may be that the algorithm identifies the actual onset while manual processing identifies it just before the main amplitude rise. However, a high percentage of determined picks with small residuals to manual reference times are evaluated with such a low quality that the distribution kurtosis decreases from $Q > 1$ to $Q > 2$.

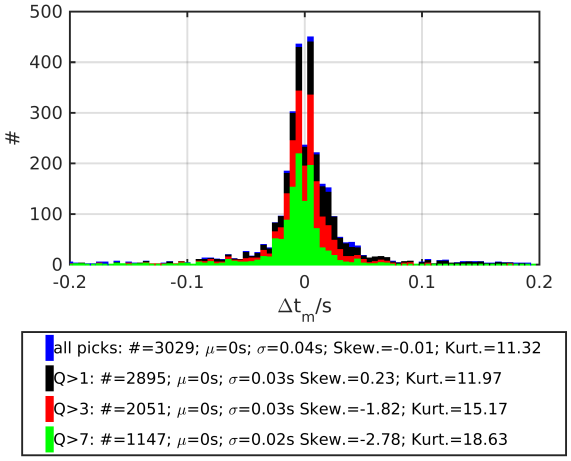

Figure 3.36.: Histograms of residuals Δt_m between automatically determined and manual P1-picks for the Insheim dataset. The color indicate different minimum quality restrictions for the histogram distributions.

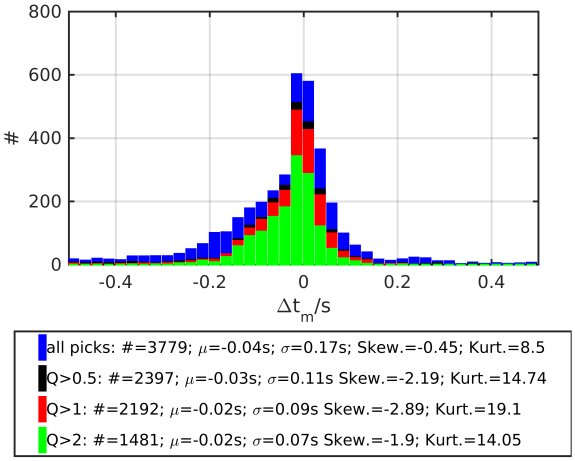

Figure 3.37.: Histograms of residuals Δt_m between automatically determined and manual P1-picks for the Insheim dataset. The color indicate different minimum quality restrictions for the histogram distributions.

Results for Landau appear consistent with the Insheim dataset. Figs. 3.38 and 3.39 show the 2D histograms of the residuals Δt_m between determined and reference manual P1- and S1-picks against the automatic pick qualities Q for Landau.

Residuals' standard deviations (white) decline with increasing qualities, steeply in low quality ranges and flattening in larger quality ranges. The distribution of qualities is shifted stronger towards larger values than for the Insheim data. Eye-catching are the approximately 500 determined P1-picks with qualities $Q \geq 8$ and very low residuals. This feature is caused by a number of impulsive onsets of strong Landau events. The residuals Δt_m are distributed around $\Delta t_m = 0s$ for the P1-phase, while a shift to positive tail is observed for the S1-phase. A higher percentage of qualities Q larger than the median ($Q = 1$) is observed although a large quantity

below $Q < 0.5$ is still dominant.

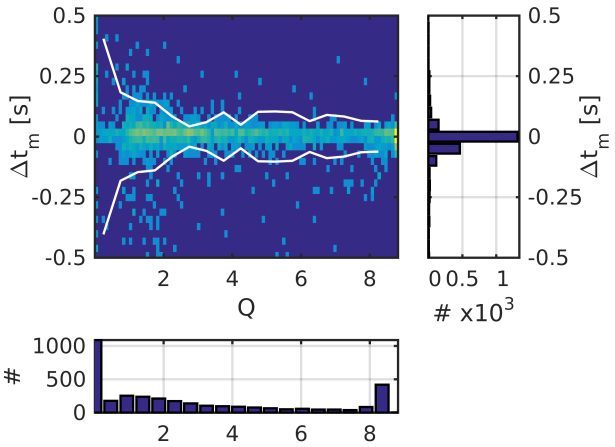

Figure 3.38.: 2D-histogram of residuals between automatic and manual P1-picks vs. automatic pick qualities for the Landau dataset. The white line shows the residuals standard deviation.

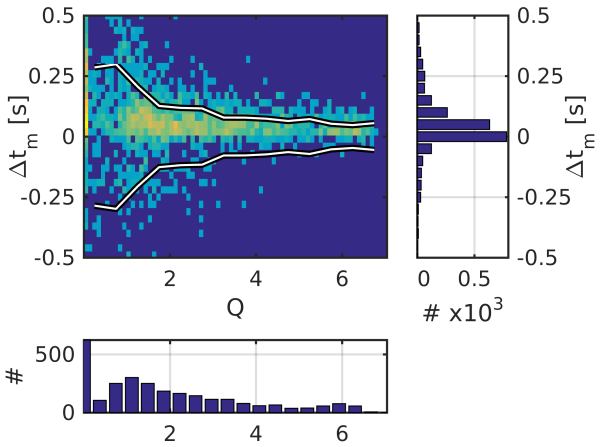

Figure 3.39.: 2D-histogram of residuals between automatic and manual S1-picks vs. automatic pick qualities for the Landau dataset. The white line shows the residuals standard deviation.

Similarly to the Insheim dataset, automatically picked P1-phase onset times of the Landau database with qualities $Q \leq 0.5$ vary stronger than $\pm 0.2s$. As a consequence, displayed residual distributions between automatically and manually determined P1-wave arrivals show only minor changes if the minimum quality restriction is set to $Q > 1$ (Fig. 3.40).

While the residuals between automatically determined and manual reference P1-phase arrival times are unbiased, a shift by $\Delta t_m \approx +0.05s$ is observed for the Landau S1-phase residuals. Consequently, while Insheim automatic S1-phases tend to be too early the Landau S1-phases are picked later than the corresponding manual picks.

An explanation could be that the cost function optimization considering only Insheim S1-waveforms as reference dataset is insufficient to provide high precision S1-phase arrival times in the Landau dataset. However, the residuals distribution still shows low standard deviations of $\pm 0.08s$ for $Q > 2$. Hence, two conclusions can be drawn: 1. S1-phase waveforms of events at the Landau and Insheim reservoir appear to be significantly different. 2. Even without special cost function parameter optimization for the Landau dataset, the phase picking algorithm identifies and picks reliable, yet slightly too late in case of the Landau database.

Summarizing the results, consistent automatic P1-picks show similar unbiased residual distributions for Landau and Insheim events with low standard deviations $\sigma = \pm 0.02 - 0.03s$. Thus, the majority of these automatically determined P1-wave arrival times are within the lowest manual picks uncertainty ($\epsilon = \pm 0.04s$).

Since the standard deviation of the residuals between automatically determined and reference

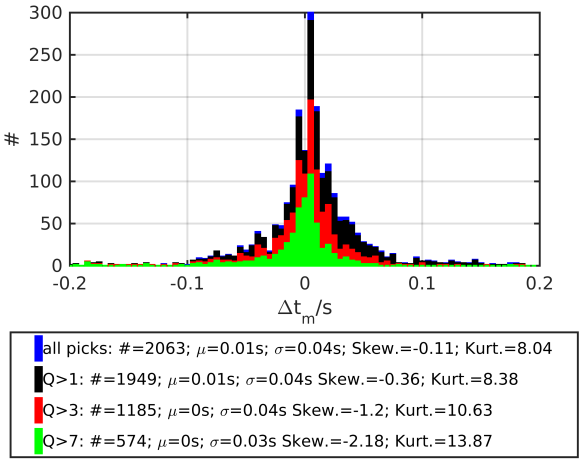

Figure 3.40.: Histograms of residuals Δt_m between automatically determined and manually read P1-picks for the Landau dataset. The color indicate minimum quality restrictions for the histogram distributions.

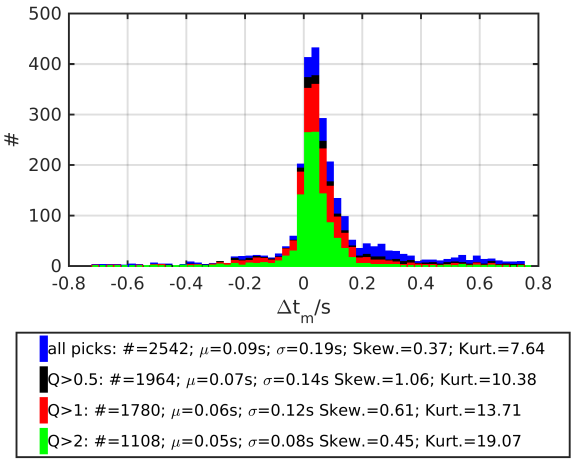

Figure 3.41.: Histograms of residuals Δt_m between automatically determined and manually read S1-picks for the Landau dataset. The color indicate minimum quality restrictions for the histogram distributions.

manual arrival time readings decreases only incrementally from $\pm 0.04s$ to $0.02s$ for Insheim and to $0.03s$ for Landau, the lowest restriction is already sufficient to identify reliable arrival times. However, a systematic increase of quality restrictions is applicable to estimate the arrival time errors. An alternative approach to quantitatively access the automatic picks uncertainties could be the combination of the quality values Q with other measures such as Wadati-plots, earliest- and latest likely phase arrivals (Diehl et al., 2009), or iterative relocating - picking procedures (Li and Peng, 2016).

Although minor systematic bias regarding reference manual S1-picks are apparent for both automatically determined S1-phase datasets, the low residuals mean values and standard deviations identify also automatic S-wave picks as reliable. An interesting feature are the opposite directions of the shifts for the different source regions which are to be investigated further.

After comparing the determined arrival times of Insheim earthquakes to 3,029 routine manual picks, which have a high reliability potential as reference value, Fig. 3.42 shows the qualities and residuals of 12,457 automatically determined Insheim P1-picks to theoretical P1-phase arrival times sorted by epicenter distances. Nearly all automatic P1-picks with residuals to calculated arrival times $\Delta t_{th} > \pm 0.5s$ have an assigned quality $Q \leq 1$. The variance of good quality picks increases beyond approximately 1 km epicenter distance splitting nearly into two branches beyond 4 km distance. Beyond 10 km, the good quality picks are about $1 - 1.5s$ earlier than the theoretical reference times since the optimized minimum 1D-velocity model is applicable only within a few kilometers around the reservoir.

For the Insheim S1-phase arrival times the determined good quality picks are systematically ear-

lier than the theoretical arrival time (Fig. 3.43). It indicates that the velocity model is too slow. The large amount of low quality automatic picks of both phases are due to many low magnitude events, high amplitude and noise from urban sources. The possible two branches, separated by approximately 0.1-0.2 s, indicated by the good quality automatic P1-picks arrivals may be evi-
5 dence for the complicated tectonic structure, e.g. a tectonic stratification offset between Landau and Insheim due to different segments in the URG, and the distribution of stations on different fault segments to the north and south. The absence of a second branch in the S1-phase travel time curve can be explained by an overall broader distribution.

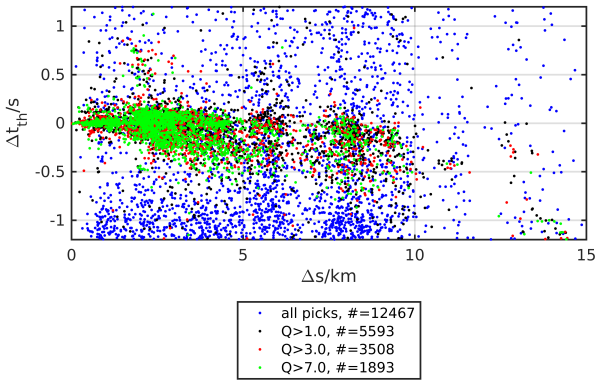

Figure 3.42.: Relative travel times of automatic P1-picks to theoretical P1-phase arrival times according to the Insheim 1D-velocity model (Bestec GmbH). The colors indicate different quality levels of picks.

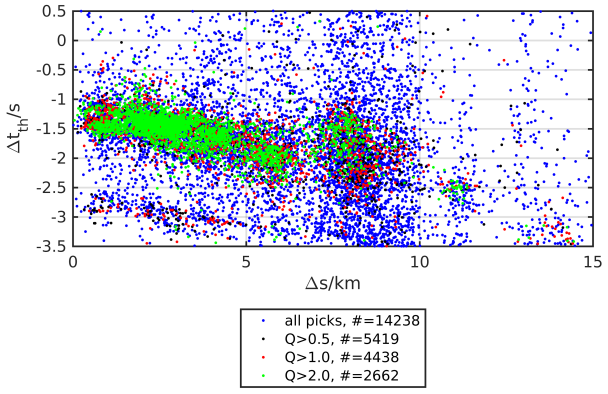

Figure 3.43.: Relative travel times of automatic S1-picks to theoretical S1-phase arrival times according to the Insheim 1D-velocity model (Bestec GmbH). The colors indicate different quality levels of picks.

3.5. Discussion and conclusion

As shown by previous studies (Di Stefano et al., 2006; Diehl et al., 2009, e.g.), for any body wave tomography or earthquake location study automatic phase arrival time determination should be considered.

We propose a new picking algorithm, which is applicable to both P- and S-phases on local and teleseismic scales. It takes advantage of the findings of previous studies, such as the superiority of the AR-AIC algorithm (Küperkoch et al., 2012) which it incorporates. Beyond that it utilizes the knowledge obtained on the difficulty to train algorithms on new datasets (Rawles and Thurber, 2015), the theoretical time as reference for a picking window (Li and Peng, 2016) or the tendency of the AIC to be too late (Leonard and Kennett, 1999; Küperkoch et al., 2012). These issues are addressed by combining the AR-AIC algorithm with an easily optimized cost function. Furthermore, a single quality value is automatically assigned to all determined phase arrival times, assessing the quality of each pick for further analysis. It has successfully been applied on both a large- (teleseismic) as well as a small-scale (local) earthquake seismology setting.

44,761(19,359) teleseismic P-(S-)phase arrivals are automatically determined and statistically compared to a dataset of compiled manually read picks. It becomes evident that by applying the quality restriction, the residuals' variances can be reduced significantly. Standard deviations of both, the residuals between automatically determined and manually read P-picks, as well as automatically determined and theoretical calculated P-picks, decrease to $\sigma = \pm 0.49s$ and $\sigma = \pm 0.77s$, respectively. Comparing the manual picks from the ISC-catalog, which is often considered for tomographic studies, to calculated arrival times a much broader distribution is found, $\sigma = 1.08s$. This hints to possible inconsistencies of such an accumulated arrival time catalog and the goodness of the picking algorithms performance. Assuming the dominant frequency of P-phases around 1 Hz, the majority of determined picks are within less than half a period difference to the corresponding manual picks, which coincides with the definition of picking uncertainties to earlier times, i.e. earliest likely pick, by Diehl et al. (2009).

Considering the lower signal periods of S-phases (5-10 s) compared to teleseismic P-phases, the standard deviations of $\sigma = \pm 4.36s$ and $\sigma = \pm 4.66s$ of residuals between automatically determined and manually read and automatically determined and theoretical S-picks, respectively, are consistent. The evidently more disrupted distribution of residuals to manually determined arrival times can be explained by a low number of manually picked S-phases as well as by the larger inconsistencies among the manually and automatically more difficult to identify S-phase arrival times. While for teleseismic P, as well as induced P1- and S1-arrivals, the number of automatic picks with an assigned high quality is equal or slightly less than what was found in the manual catalog, the good quality automatic teleseismic S-phase picks exceed the manual database by a factor of 2.5. This result makes the newly developed algorithm highly valuable for tomography and location studies since it increases the overall data which can be included. Especially in location applications, including S-phase arrivals improves the vertical resolution.

The utilization of such a automatically determined teleseismic dataset in tomographic studies is highly recommended as consistency is ensured and a weighting concerning the reliability of arrival times can be incorporated.

Applying the algorithm to the teleseismic data provides many phase arrivals at low computational cost. Processing the whole dataset of approximately 60,000 teleseismic P- and S-wave picks takes less than 6 hours on one single CPU. However, the value of these automatic phase picks is difficult to assess by only comparing them to manual picked catalogs. Since different parameter settings result in inconsistent manually read reference databases (Grand, 1990; Douglas et al., 1997), the residuals of automatic picks to manual picks are not the automatic picking uncertainty. Instead it indicates a combined picking error of automatic and manual arrival time readings. In order to investigate the picking uncertainty further a consistent reference database with a fully transparent and comprehensible workflow is required.

Within tomographic studies, the finding of frequency dependent shifts of P- and S-phase arrival times should be considered as well. Automatic re-processing of earthquake datasets by applying different filter bands offers the opportunity to find frequency dependent travel time variations of body waves. The quick processing of automatic picking may thus provide the opportunity to access the Fréchet kernels by body wave arrival time observations and thus increase the tomography resolutions. However, preceding such a study a systematic analysis of the automatically determined picks in different bands is required to ensure that the shifts actually result from frequency dependent phase velocities. For this purpose reference datasets of manually phase time readings in the individual frequency bands and frequency dependent parameter selection and optimization are recommended.

Various aspects of wave arrival time determination change significantly, when moving from the larger scale to small scale microseismicity. Signal frequencies increase strongly, there are locally varying noise sources causing low SNR and the objective is to process both, small and large amplitude earthquake signals. Nevertheless, the phase arrival times determined by the algorithm are very precise. Using the quality evaluation, the residuals between the automatic and the manual picks show a low variability around $\pm 0.02/0.03s$ for the P1-phases at Insheim and Landau as well as $\pm 0.05s$ for the S1-phases. A minor distribution bias for the distributions of determined S1-arrival times at Insheim ($-0.02s$) and Landau ($+0.05s$) indicates that the source processes and Green's function between the individual reservoirs and stations vary strongly. Although the low standard deviation is an indicator for the reliability of the automatic P1- and S1-picks, as a result of the identified shifts, we recommend to repeat the cost function training for each reservoir individually.

A decrease of standard deviations of residuals between automatic and manual phase picks with increasing automatically derived qualities is evident and considered as an indicator for the good working quality control. Nonetheless, a significant number of automatic picks are assigned a low

quality, although they show low residuals around $0s$. Such a loss of potentially valuable data is problematic since the dataset shrinks dramatically and the stability of subsequent location or tomography studies may be affected. Especially, hypocenter locations of low magnitude events, which are recorded at only a few stations, can be lacking a proper azimuthal coverage of arrival times.

On the other side, individual as good quality evaluated outliers of residuals between automatic and reference manual picks indicate that the algorithm occasionally reacts to noise bursts or other misleading signals, e.g. when the originally requested phase is not observed or has an extremely low SNR. When applied in consequent studies, these can introduce artificial offsets in locations or tomographic results. However, since the number of the residual outliers are negligible low ($\approx 1\%$) a statistical edge-cutting, Wadati-plots or similar measure can be able to remove them.

Concluding, the proposed algorithm proves to be robust and precise. For the quality evaluation, additional measures are required to access the actual timing uncertainty and to avoid loosing a high number of low residual picks. In what follows, the determined phase arrival times of the induced earthquakes at the Insheim plants are utilized to relocate the hypocenters and retrieve information on the applicability of automatic picking results in routine processing.

4. Location precision using automatic phase time readings

4.1. Introduction

Following the detection of induced seismicity and the determination of phase arrival times of induced earthquakes, the location is the consequential next step of processing. In this chapter two aspects are discussed. First, the automatically determined phase arrivals are used to relocate induced events. The results are compared to locations derived from manually read phase onset times. Secondly, precise relative locations are determined in order to retrieve information from the hypocenter distribution. In contrast to the preceding chapters, only data from the Insheim reservoir is considered here.

4.1.1. Motivation

Earthquake location is a challenging task and results depend strongly on two aspects: data coverage (seismic phase arrival times) and a well resolved velocity models.

Seismic events locations provide insights into geodynamic processes and in which volumes inside the earth body energies are released. Besides the energy release by earthquake nucleation, the structural orientation of seismicity allows the development of physical models for tectonics. Major tectonic boundaries, e.g. mid-oceanic ridges or subduction zones, are characterized by enhanced seismicity. From the locations of earthquakes within subduction zones, locked subduction interfaces can be identified. The interface seismicity in subduction zones is defined by the Wadati-Benioff-Zone which thus describes the range where temperature, pressure and material allows the brittle failure of rock and the nucleation of earthquakes. Identifying the Wadati-Benioff zone by tracing earthquakes to the correct locations provides therefore an estimation on temperature and pressure gradients as well as material properties in the appropriate depths (e.g. Husen et al., 1999; McCrory et al., 2012). In addition, valuable information on locked segments, where mega-thrust earthquakes occur, are retrieved by the absence of seismicity in these gaps. Other tectonic examples are the tracing of earthquake hypocenter to resolve fault geometries (e.g. San Andreas fault, Hauksson and Shearer, 2005) or identifying melts and melt migration in volcanic areas (e.g. Lahr et al., 1994).

A non-earthquake related, yet highly important application of the seismological location process

is related to the nuclear weapon test ban (e.g. Waldhauser et al., 2004). Since the international test-ban of nuclear weapons has been decided in 1996, the Comprehensive Nuclear-Test-Ban Treaty Organization (CTBTO) monitors the compliance of signed members by analyzing seismic recordings globally.

Event locations are also required for nearly every seismological analysis besides the indicated direct interpretation. Tomographic inversions require well located events such that the travel time residuals depend solely on velocity distributions. Errors of the location may change velocity perturbation amplitudes as well as spatially shift the determined perturbations.

In case of induced seismicity, earthquake locations provide the basis for studying responses of earth materials to anthropological influences. The interference with a system under certain initial conditions, i.e. effective stress condition, material properties, pore-filling, etc., results in changes of these conditions which are indicated by the induced/triggered seismicity. By analyzing the nucleated seismic events and released energy, the initial volume conditions may be reconstructed and future response may be predicted. In order to distinguish naturally occurring and induced seismicity, precise locations may be able to differentiate events spatially (Wehling-Benatelli et al., 2013). Although naturally occurring seismicity is not known in the vicinity of the geothermal reservoirs Landau and Insheim, precise earthquake locations are required in order to assign the energy release to one of the reservoirs as well as to certain parts of the individual reservoirs.

While the amount of seismic data increases constantly, the reading of seismic phase arrival times is still carried out manually. Diehl et al. (2009), Husen et al. (2009) and Scafidi et al. (2016) use automatically determine phase arrival times in consecutive applications like tomography and locations. Scafidi et al. (2016) finds that the locations retrieved by using automatic picks vary less than 2 km from the hypocenters determined from manual phase time readings. However, it is difficult to access the actual precision since no uncertainties of hypocenters are provided.

As shown in chapter 2.4.3 different clusters of induced events within the individual geothermal reservoirs can be distinguished by their waveform similarities. Following this lead, precise locations may also be able to identify sub volumes within the reservoirs which differ in spatial locations.

Thus, two aspects are discussed in this chapter. First, the phase arrival times determined using the AR-AIC-costfunction approach discussed in chapter 3 are applied to relocate earthquakes at the Insheim geothermal reservoir. These relocations are compared to hypocenter positions retrieved from the reference manual pick catalog by the Bestec GmbH, Landau Germany. Second, precise relative relocations of Insheim earthquakes are calculated in order to resolve spatial seismicity patterns in the Insheim reservoir. However, before assessing these aspects, a brief introduction to the seismic event location procedure is given in the next section.

4.1.2. Hypocenter location of seismic events

In general, the event location process presents a coupled problem (Kissling et al., 1994; Husen and Hardebeck, 2010). Given the setting of an earthquake, a volume through which the seismic waves propagate and seismic stations, the event location procedure can be described as following. Starting at source time t_0 at the the event hypocenter x_0 the seismic waves travel through the medium of certain velocities. Depending on the stations locations, these seismic waveforms are recorded at a certain time which is defined by the source time t_0 plus the travel time Δt_{tt}. The travel time depends in the high frequency approximation applied to ray tracing, arrival time picking and locating, solely on the source - receiver geometry and the velocity along the wave ray path.

If the velocity distribution in the subsurface is known, travel times can be calculated from each point in the subsurface to each considered station. The actual event location can be retrieved by minimizing the residuals between calculated and observed travel times. However, the calculated arrival times do not change linearly by shifting the source location (x,y,z) since the ray path itself is velocity and thus start point dependent. Consequently, the problem of determining the four unknowns (source location in three dimensions and source time) must be solved either by a statistical or an linearly approximated inversion.

Various aspects of the solution processes lead to accessible and not accessible uncertainties in the locations. The velocity model is the essential basis of the location procedure (Gomberg et al., 1990). Usually it is determined up-front from seismic studies or as an estimation of other geophysical studies. Since velocity heterogeneities differ in scale and amplitude and their impact depends on wavelengths, the selection of proper models is case dependent and may differ between complex three dimensional models and simple one dimensional velocity distributions. Both 1D- and 3D-models may be deficient depending on the structural complexity of the investigated volume. 3D-models may provide better earthquake locations if sufficient information on the velocity distribution are available. Otherwise, a 1D-velocity model avoids the introduction of artificial velocity perturbations at the accepted cost of larger location uncertainties. These can be reduced by determining source and/or station corrections which account for local velocity perturbations beneath the individual stations (Douglas, 1967; Shearer, 1997).

Other sources of location uncertainties are the network geometry, the availability of phase arrivals and the errors of phase time readings (Waldhauser and Ellsworth, 2000). A network geometry should cover the range around earthquake locations systematically such that no large azimuthal gaps ($>120°$, Bondár et al., 2004) remain. These may lead to large epicenter errors in preferred directions. Since four unknowns are given a set of at least four observed phase arrivals is required to solve the location problem. With increasing numbers of phase arrivals, the solution space is expected to decrease. Including S-wave arrivals in addition to the commonly applied P-wave arrivals improves especially the vertical resolution (Gomberg et al., 1990).

4. Location precision using automatic phase time readings

Finally, the effect of phase arrival time errors results in 3D location uncertainties, hence an error ellipsoid. This timing error describes the uncertainty range around the determined phase arrival time in which the phase arrival time is certainly found. Incorporating this uncertainty can provide the actual location error if an optimal velocity model as well as a proper azimuthal and data coverage is given. However, many algorithms do not evaluate the precision of locations. Commonly applied location software tools are e.g. HYPO71 (Lee et al., 1972), Hypoellipse (Lahr, 1999), Hyposat (Schweitzer, 1997) or NonLinLoc (Lomax et al., 2000).

Besides these algorithms which determine the absolute locations, relative location procedures provide an alternative approach. Assuming that the inter-event separation may be sufficient for analyzing e.g. earthquake re-occurrences or earthquake interactions, these approaches determine the locations of earthquakes relative to each other (Pavlis, 1992; Got et al., 1994; Waldhauser and Ellsworth, 2000). The advantage of the relative location is that it is independent of velocity distributions along the ray paths. Instead the relative travel time differences of a seismic phase from two events to a single station depends solely on the offset of the hypocenters. However, this is only valid under the assumption, that the velocity in the source region of the compared events is constant (Pavlis, 1992; Waldhauser and Ellsworth, 2000).

Since the location procedures is an essential routine processing step in common seismological practice, the future consideration of automatically determined arrival times as replacement or supplement to manual routine picking depends strongly on the reliability of hypocenter locations retrieved from these. Especially for induced seismicity with a broad public and economical interest, automatically determined phase arrivals could be used for locations if sufficient precision and robustness are confirmed. However, in order to study the seismicity distribution in more detail, routine locations are insufficient. Since the similarity detection in Chapter 2 indicates several earthquake clusters in the Insheim and Landau reservoir, a relative relocation of the induced earthquakes can likely provide insights into spatial patterns and migration paths of seismicity in the reservoirs.

4.2. Location methods

4.2.1. Probabilistic hypocenter relocation

The uncertainty of location has an important role and the representation of a complex tectonic structure using a minimum 1D-velocity model provides a possibly unstable or ill-conditioned location problem. Hence, the relocation of absolute hypocenters is done using the non-linear, probabilistic earthquake location software NonLinLoc (Lomax et al., 2000). This approach solves the inverse problem by calculating a source time first and determining a probability-density function afterwards. Tarantola and Valette (1982) provide a probabilistic formulation of inversion which states that if theoretically calculated and observed arrival times have Gaussian uncertainties and the origin time is uniform, the location density function can be calculated analytically. Consequently, instead of determining a single-point solution by assuming a linearization of the problem, Lomax et al. (2000) assumes Gaussian arrival time errors to provide the likeliness of many source point solutions.

In order to reduce calculation time during the location procedure, the software NonLinLoc calculates first arriving, infinite frequency P- and S-wave travel times between each station and all pre-defined grid nodes beforehand. For this purpose it uses the Eikonal finite-difference scheme by Podvin and Lecomte (1991). The software provides three search algorithms to determine the probability density function: a Grid-Search algorithm, a Metropolis-Gibbs Sampling algorithm and an Oct-Tree Importance Sampling algorithm.

The Grid-Search uses the whole volume as solution space and calculates the probability on each node of an initially defined grid. In order to get precise locations, finer grids with reduced cell sizes are defined within the initial grids and the probability is recalculated in all cells of the finer grid. Consequently, it is a exhaustive yet time-consuming approach and the resulting probability function may vary strongly dependent on the grid size and spacing Lomax et al. (2000).

The Metropolis-Gibbs Sampling algorithm defines three sampling stages during which it tracks the region of highest probability. Following these stages the search step size decreases. In the first stage, regions of high probability are identified. During the second stage the step size is iteratively adjusted according to standard deviations of the probable locations spatial distribution. In the final stage the actual probability density function is determined from probabilities in the final search region. While the starting step size must be large enough to actually cover the whole search volume, the final final step size must be small enough to resolve the location probability function(Lomax et al., 2000).

Finally, the Oct-Tree Importance Sampling algorithm uses subdivision of the grid cell with highest probability to determine the probability density function. After identifying the cell with the highest probability, it is divided into eight new cells. The probability is calculated in these sub-cells and considered with all previously known probabilities when choosing the cell of highest

probability again. In optimal cases, the region of high probability is well resolved providing many small sub-cells with high probabilities (Lomax et al., 2009).

While all algorithms can achieve more or less the same precision and resolution in optimal location cases, each algorithm has advantages and drawbacks. Both, the Metropolis-Gibbs Sampling and the Oct-Tree Importance Sampling algorithm are faster than the Grid-Search by a factor of 100 (Lomax et al., 2000, 2009). Furthermore, the Oct-Tree algorithm is independent of the initial step size selection and more global than the Metropolis-Gibbs algorithm. This means, that while the Oct-Tree Algorithm refines the probability grid calculation independent on the region, the Metropolis-Gibbs algorithm can be trapped at regions of high likeliness missing a possible second likeliness maximum. However, the Oct-Tree algorithm is computational expensive when considering large observation datasets and 3D travel time grids. Yet, the number of observations is limited for the induced seismicity since the magnitudes do not allow many observations. Therefore, the Oct-Tree Importance Sampling algorithm is selected as the best approach to relocate the absolute hypocenters of induced Insheim earthquakes using manual phase arrival time readings and automatically determined picks, respectively.

4.2.2. Double-difference hypocenter relocation

In addition to the absolute location methods described above, the double-difference approach provides a method to reduce the relative location uncertainties significantly. For this purpose, the software hypoDD by Waldhauser and Ellsworth (2000) is applied. In contrast, to absolute location approaches, the hypoDD algorithm aims to minimize the difference between observed and calculated travel time differences between event pairs. Following Geiger (1910), a linearization of the inverse location problem is applied. It works without the station correction assuming that relative travel time differences of seismic waves from neighboring events to a station result only from the hypocenter offsets. In order to apply this method two conditions need to be fulfilled:

1. The hypocentral separation between the two events must be small compared to the event - station distance and the scale length of velocity heterogeneities, respectively.
2. The velocity distribution must be homogeneous within the source region.

If these conditions are fulfilled, the absolute locations of close-by earthquakes are moved to minimize relative travel time differences for each event pair. A large advantage of this method is that it is independent of the velocity distribution between source and receivers. The velocity considered for the relative hypocenter location is solely the velocity within the source region. If not all earthquakes in the catalog fulfill the criteria of low hypocenter separation, the algorithm provides threshold flags such that only events which are separated by less than the threshold values are considered for the relative relocation process.

A drawback of this method is that the absolute locations may be misleading. While the relative location uncertainty decrease significantly during the relative relocation process, the absolute locations may be shifted systematically (Waldhauser and Ellsworth, 2000).

HypoDD has become a commonly used relative relocation tool used in various studies (e.g. Zhang, Haijiang and Thurber, Clifford H., 2003; Thurber et al., 2006; Grund et al., 2016). Especially in studies about locations of microseismic events as well as locations in regions with poorly resolved velocity models, it is a very useful tool to resolve spatial features (e.g. faults or Wadati-Benioff zones, Kuochen et al., 2007; Grund et al., 2016), differentiate between event clusters (e.g. induced and tectonic events, Wehling-Benatelli et al., 2013) or identify seismic evolution patterns (e.g. aftershock distributions, Wang et al., 2013; Bounif et al., 2004).

In the following, the relocation of induced seismic events at the Insheim reservoir is carried out with two objectives. First, the determination of the absolute hypocenter locations using NonLinLoc aims to understand how results differ if automatically determined phase arrival times are applied instead of manually determined picks. Second, HypoDD relative relocations of Insheim earthquakes are calculated to provide a better understanding of spatial distributions of induced seismicity.

4.3. Location precision using automatic arrival times

After introducing the considered location methods, the relocation of hypocenters using the software NonLinLoc by Lomax et al. (2000) is discussed in this section.

4.3.1. Absolute hypocenter relocation database

For the relocation a grid of 30x30x10 km is defined with a cubic 100 m grid cell size. Consistently to routine manual processing the refined minimum-1D P- and S-wave velocity models (Fig. 4.1) for the Insheim reservoir are used (pers. comm. Dr. L. Küperkoch, Bestec GmbH, Landau i.d. Pfalz, Germany). Since it is an inverted one dimensional velocity model its representative meaning for tectonic or geological features is highly questionable. Nevertheless, the high velocity zone between 1 and 2 km depth correspond to the depth of a Muschelkalk horizon at the Insheim wells.

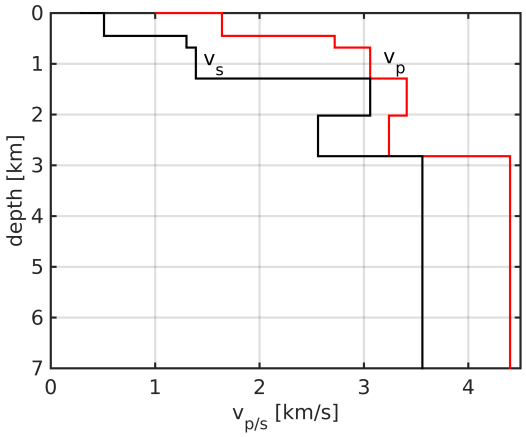

Figure 4.1.: Minimum 1D-velocity models for the region around Insheim including compressional (v_P) and shear wave (v_S) velocities. The model has been inverted using approximately 13.500 induced earthquake phase arrivals and geological a priori information (pers. comm. Dr. L. Küperkoch, Bestec GmbH, Landau i.d. Pfalz, Germany).

The hypocenter relocation is carried out keeping the parameter settings constant while utilizing different phase arrival times data. Six datasets of phase arrival times are considered:

- Only manually read P-wave arrival times.
- Only automatically read P-wave arrival times.
- Only manually read P- and S-wave arrival times.
- Only automatically read P-wave arrival times.
- Only manually read P- and S-wave arrival times.
- Both, manually and automatically determined P- and S-wave arrival times.

The automatically determined arrival times are retrieved from the application of the AR-AIC-costfunction algorithm to the Insheim dataset as described in Chapter 3.

The combination of both, the manually and automatically determined arrival time datasets is carried out under the assumption that the manual phase picks are more reliable than the automatically determined arrival times, since the manually read phase picks have been reviewed. Hence, the automatically determined arrival times are regarded as a complementary dataset. In order to simplify the reading, hypocenter locations determined by using automatically read phase picks are referred to as *automatic locations/hypocenters* hereafter and locations using only manual phase time readings as *manual locations/hypocenters*, respectively.

Not all event hypocenters are successfully or reliably relocated. Different aspects of the input data and the final location need to be fulfilled in order to be accepted. A location result is defined as unreliable if the maximum azimuthal gap from hypocenters to stations exceeds 120° (Bondár et al., 2004), if the resulting most likely epicenter is positioned outside the source region around Insheim ($49.1° \leq latitude \leq 49.2°$ and $8.1° \leq longitude \leq 8.2°$) as well as if the depth of the most likely hypocenter is positioned on an extreme depth ($z \geq 0km$ and $z \leq 9km$).

An important aspect of the comparison is that the automatically and manually determined datasets do not necessarily include the same station-event combinations. As a result, the data coverage and azimuthal gaps may differ. Fig. 4.2 shows the number of arrival times per chronologically sorted hypocenter relocation. Events for which no phase arrival time data is displayed are either not relocated or declared to be unreliable relocations.

Approximately 64.7% (262) of the automatic most likely hypocenters located with P1-wave picks fulfill these conditions. Applying automatically determined P1- and S1-wave picks, 90.86% (368) are reliably located. Using the manually read P1-phase arrival times 89.6% (363) are reliably located and 91.6% (371) using the manual P1- and S1-wave picks, respectively. The overall numbers of manually read arrival times per event are slightly higher (ca. 10-50/event) than for automatically determined picks (ca. 10-40/event). However, after 2014 ($\approx Eventno.250$) the number decreases with the selling of the Landau power plant including several monitoring stations.

The comparison of manual and automatic relocations determined using only P1-phase arrival times and using P1- and S1-phase arrival times is discussed in the next section followed by a presentation of the relocations applying combined arrival time data. For the comparison, the most likely hypocenter location is considered instead of the center of the error ellipsoid.

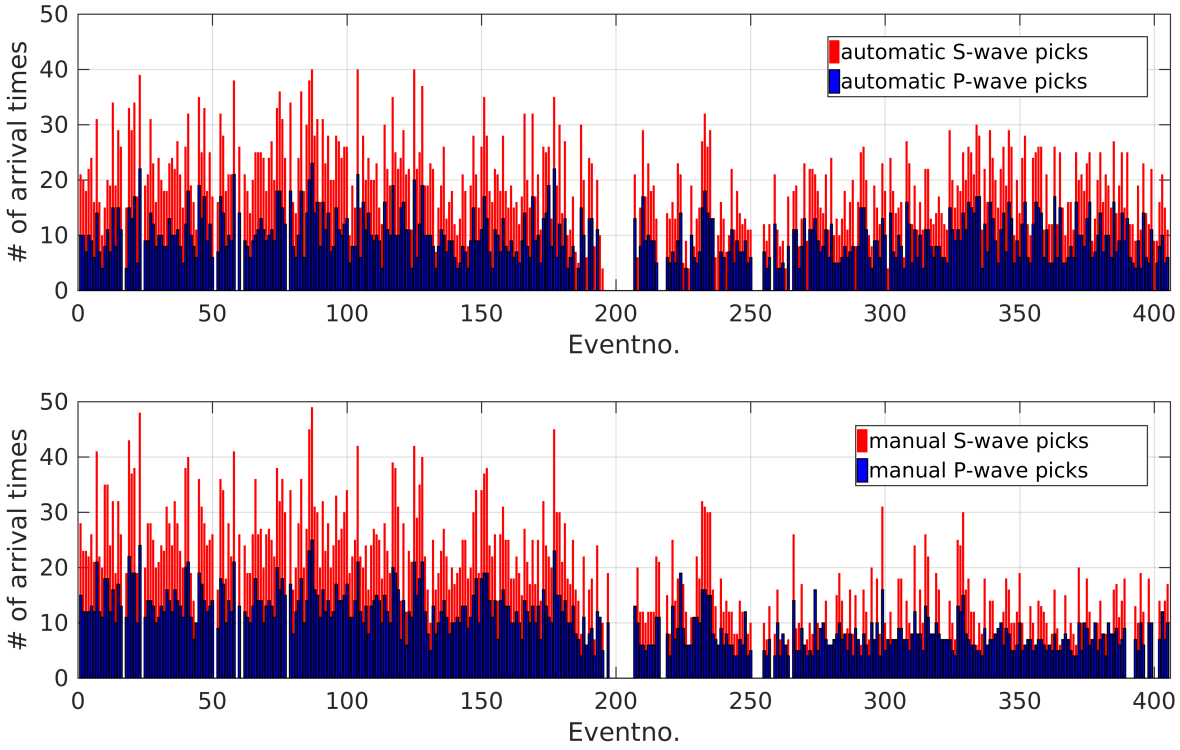

Figure 4.2.: Number of automatically (top) and manually (bottom) read P- and S-wave arrival times per chronologically sorted relocated earthquakes of the geothermal reservoir, Insheim. Included are only the arrival time picks which are considered in the relocation process.

4.3.2. Comparison of relocations using P1-phase arrival times

Fig. 4.3 shows the absolute hypocenter locations using automatically (top) and manually (bottom) determined P1-phase arrival times. In consistency to the higher number of manual P1-phase arrival time readings, the absolute number of manual locations is higher and epicenter separations are smaller. The distribution of epicenters using automatic phase time readings show several outliers towards the north. Although the overall vertical distribution of hypocenters are similar, about 5-10% of the automatic locations tend towards unrealistic shallow depths.

No systematic hypocenter bias is observed when comparing manual to automatic locations (Fig. 4.4). Most automatic locations are within 1 km horizontally and 2 km vertically to the corresponding manual hypocenter. Although 64% of the automatic hypocenters which are within the error ellipsoid of the manual locations (green) are close-by ($\leq 0.5km$), low offset automatic locations outside the manual error ellipsoids (red) as well as far offset automatic locations within the manual error ellipsoids are observed. These information hint towards heterogeneous error ellipsoid dimensions or at least orientations.

The resulting histograms of absolute offsets in horizontal and vertical dimensions confirm that the majority of automatic hypocenters are within 1 km offset to manual locations (Fig. 4.5). Including only the automatic locations within the manual error ellipsoids, the offset standard

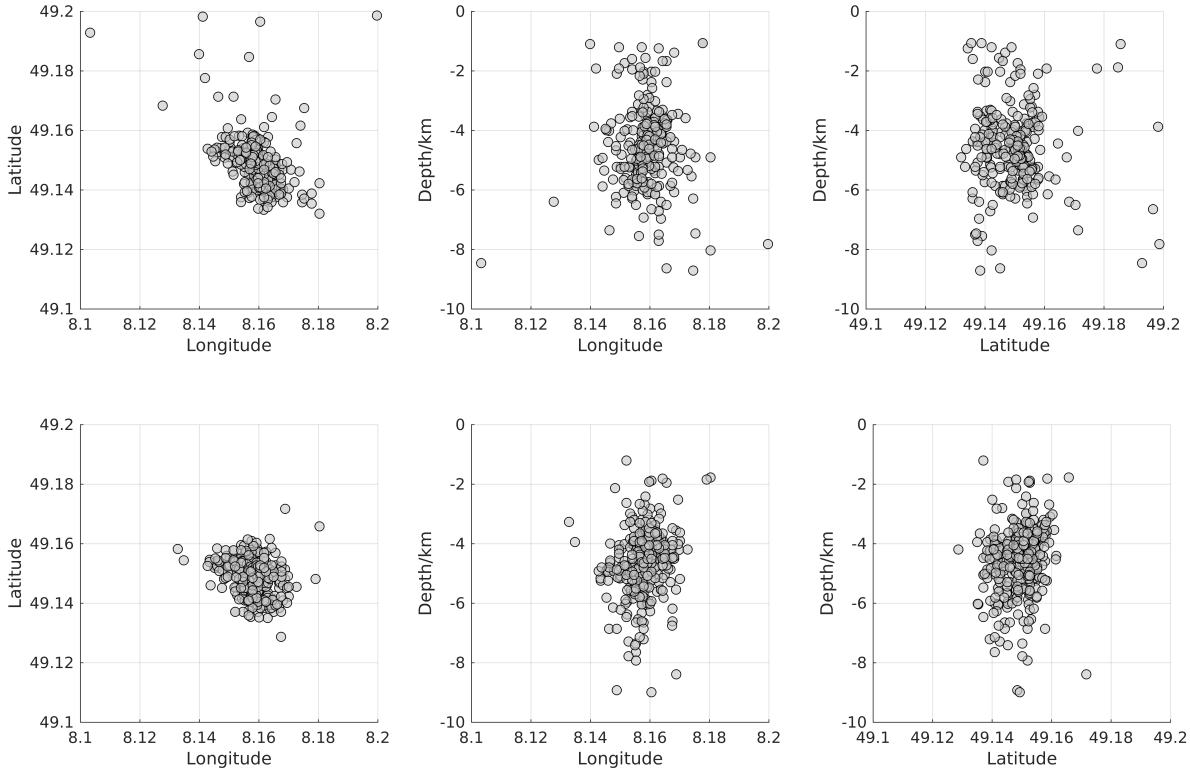

Figure 4.3.: Top view (left), North-Depth cross-section (center) and East-Depth-cross-section (right) of absolute hypocenter locations of 262 (64.7%) reliable automatic (top) and 363 (89.6%) manual (bottom) most likely hypocenters considering only the P-wave arrival times.

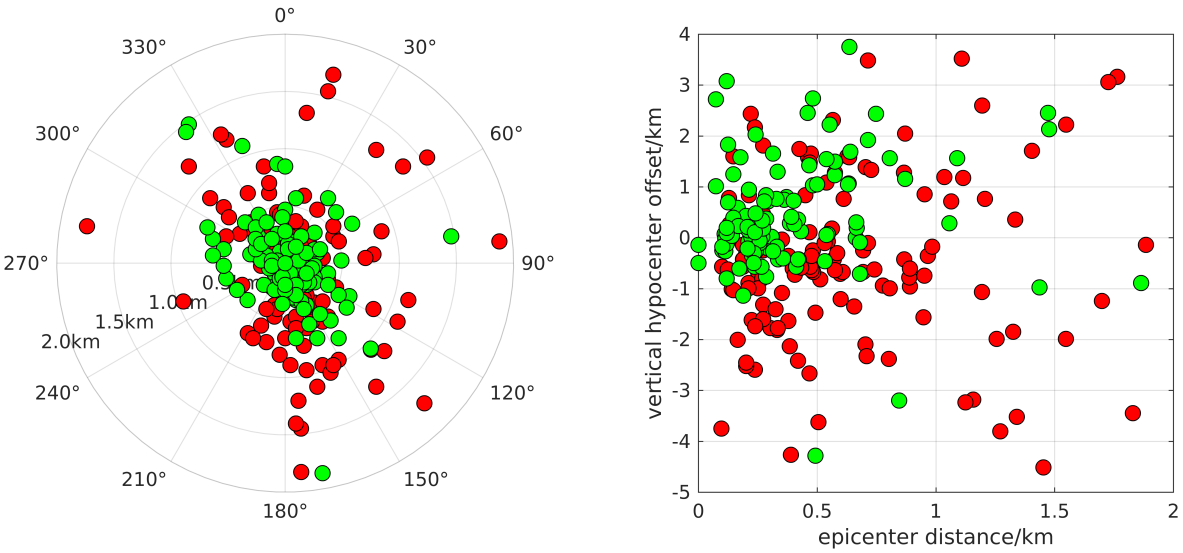

Figure 4.4.: Relative epicenter (left and right) and hypocenter depth (right) offsets between automatic and manual hypocenters using P-wave arrivals. Green filling indicates that the automatic hypocenters are within the manual location error ellipsoid and red filling means that the automatic hypocenter is outside the ellipsoid, respectively.

deviations are about $\pm 0.5km$ horizontally and $\pm 1km$ vertically (green lines).

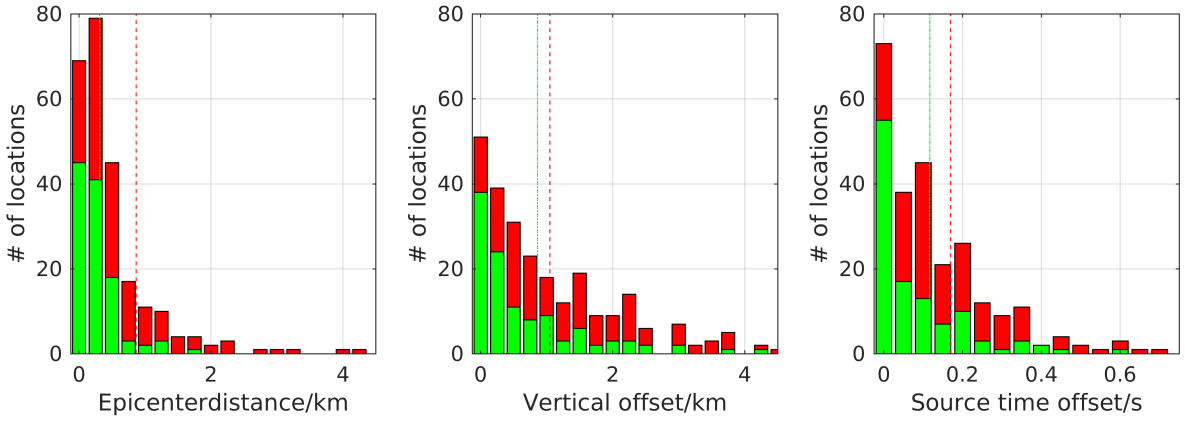

Figure 4.5.: Histograms of absolute epicenter (left), hypocenter depth (center) and source time (right) offsets between automatic and manual hypocenters determined from P-wave arrival times. Green filling indicates that the automatic hypocenters are within the manual location error ellipsoid and red filling means that the hypocenter is outside the ellipsoid, respectively. Red- and green line indicate the residuals standard deviations.

4.3.3. Comparison of relocations using P- and S-wave arrival times

Taking S-wave arrivals into consideration more hypocenters are reliably located (Fig. 4.6). The positions of automatic most likely epicenters vary in equal scales as the automatic locations considering only P-wave arrivals (Fig. 4.3). While the core epicenter area appears stricter outlined using only P-wave arrivals, the automatic hypocenters from P- and S-wave arrival times show less variance regarding the depths between -3 and -7 km.

Likewise, the introduction of manual S-wave arrivals results in a stronger concentration of manual hypocenters within the same depth range while not changing the epicenter distribution. Shallower concentrations of automatic as well as manual hypocenters appear unrealistic and indicate an artificial effect introduced by the v_S velocity model.

While the epicenter offsets are more variable than before, the hypocenter depth offsets are concentrated within $\pm 1km$ (Fig. 4.7). Two trends are observable. First, a preferred epicenter offset direction running from north-west to south-east is apparent. Second, with increasing epicenter offsets, the automatic hypocenter depths tend towards shallower depths than the manual hypocenters. In consistency to the location offsets considering only P-wave arrival times, automatic locations within the manual error ellipsoids are visible for the whole offset range.

The stronger variation of epicenters is supported by the offset histograms (Fig. 4.8). While the peak of hypocenter depth offsets remains at 0 to 0.2 km, more automatic epicenters are off by 0.2 to 0.4 km than by 0 to 0.2 km. Thus, the epicenter offset increases to approximately $\pm 1km$ while the vertical offset remains constant.

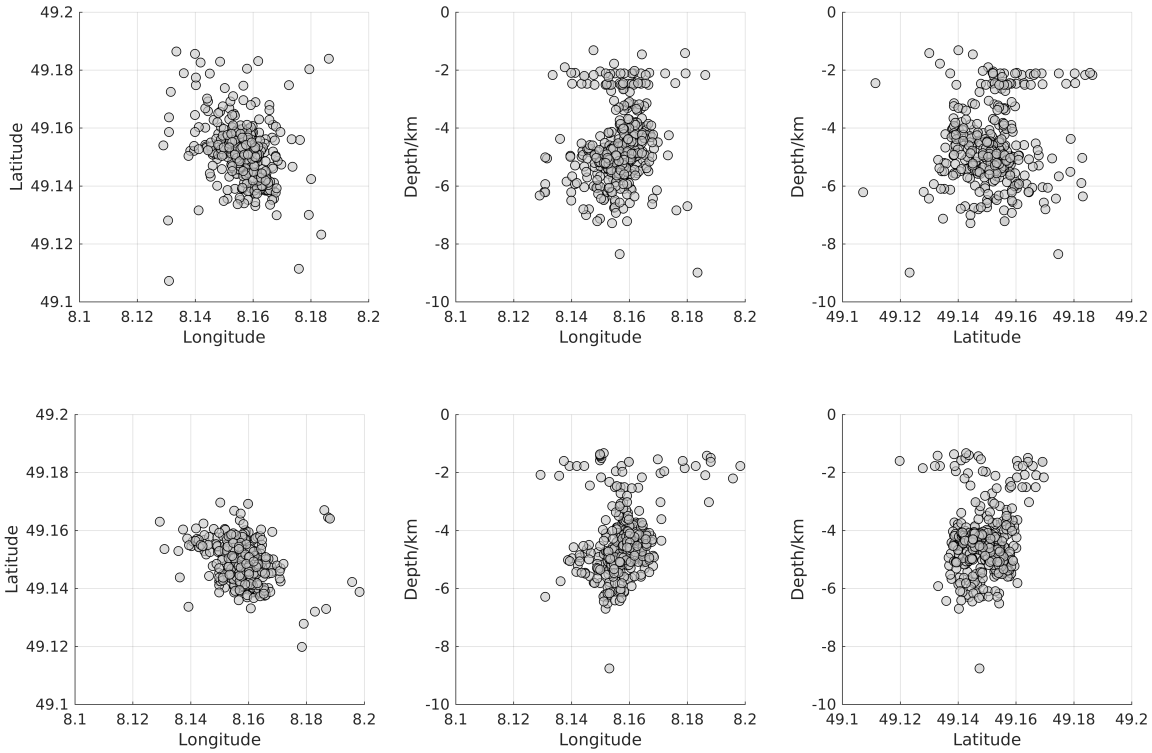

Figure 4.6.: Top view (left), North-Depth cross-section (center) and East-Depth-cross-section (right) of absolute hypocenter locations of 368 (90.7%) reliable automatic and 371 (91.6%) manual most likely hypocenters considering P- and S-wave arrival times.

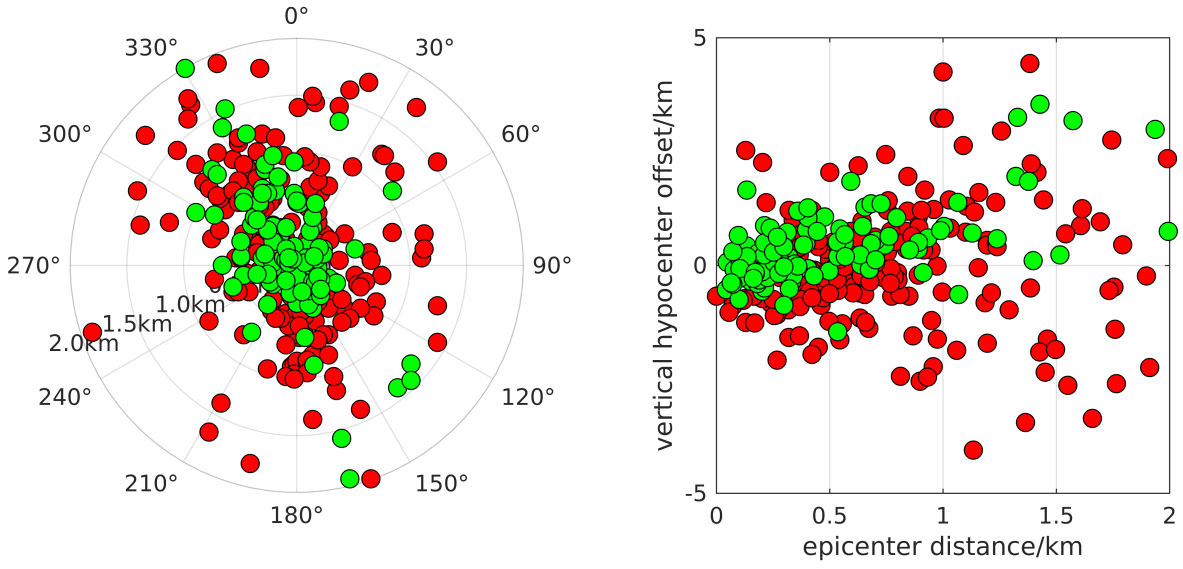

Figure 4.7.: Relative epicenter (left and right) and hypocenter depth (right) offsets between automatic and manual hypocenters using P- and S-wave arrivals. Green filling indicates that the automatic hypocenters are within the manual location error ellipsoid and red filling means that the hypocenter is outside the ellipsoid, respectively.

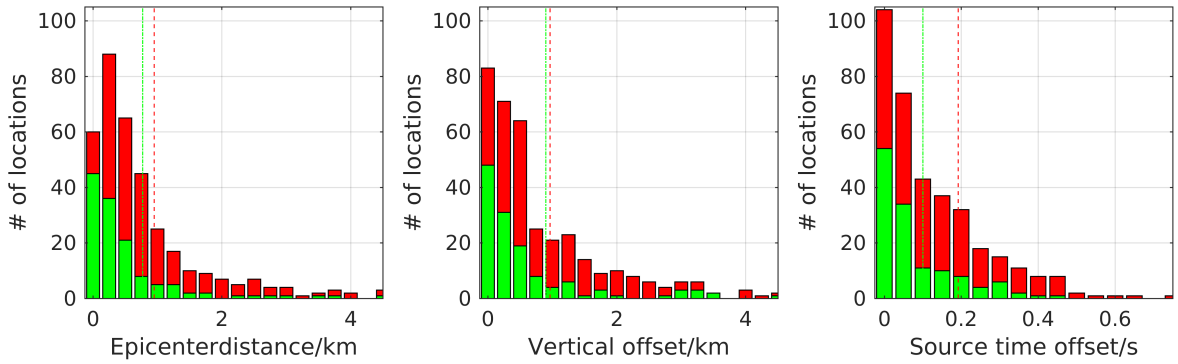

Figure 4.8.: Histograms of absolute epicenter (left), hypocenter depth (center) and source time (right) offsets between automatic and manual hypocenters determined from P- and S-wave arrival times. Green filling indicates that the automatic hypocenters are within the manual location error ellipsoid and red filling means that the hypocenter is outside the ellipsoid, respectively. Green and red line indicate the offset standard deviations.

4.3.4. Comparison of relocations combining manually and automatically determined arrival times

Finally, the question how automatically determined phase arrival times perform as complementary information to the manually read arrival time catalog is discussed. Fig. 4.9 shows the number of manual and complementary automatic picks considered for each relocation. Until event 175 only individual automatically read arrival times are added. For later events up to 20 complementary picks are used outnumbering the manual arrival time data in individual cases.

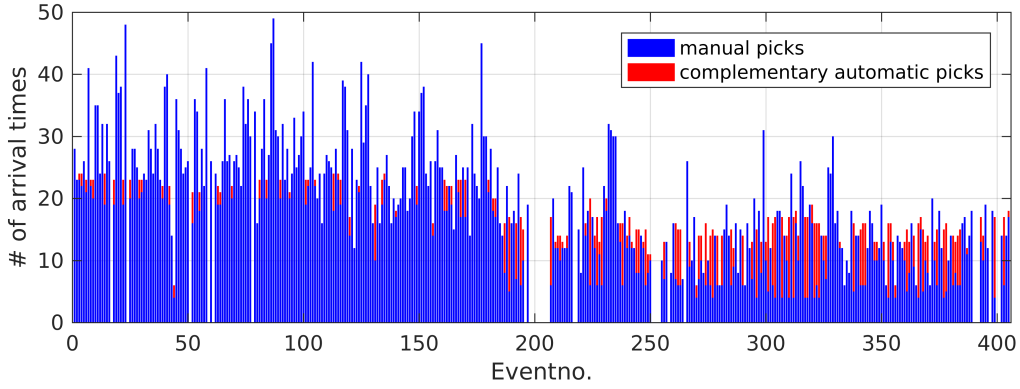

Figure 4.9.: Histogram with total number of P- and S-wave phase arrival times considered for each event relocation. Blue filled areas indicate the number of manual phase time readings and red filled areas mark the number of complementary automatically determined picks.

374 (92.4%) induced events are reliably relocated considering the combination of arrival time datasets. In reference to the manual relocations considering P1- and S1-phase arrivals, the core volume of the locations appears better refined using both databases (Fig. 4.10). Several outlier hypocenters are observed as well. The vertical concentration of hypocenters ranges from -6 to -3 km. Furthermore the number of shallow hypocenters above -2.5 km is reduced.

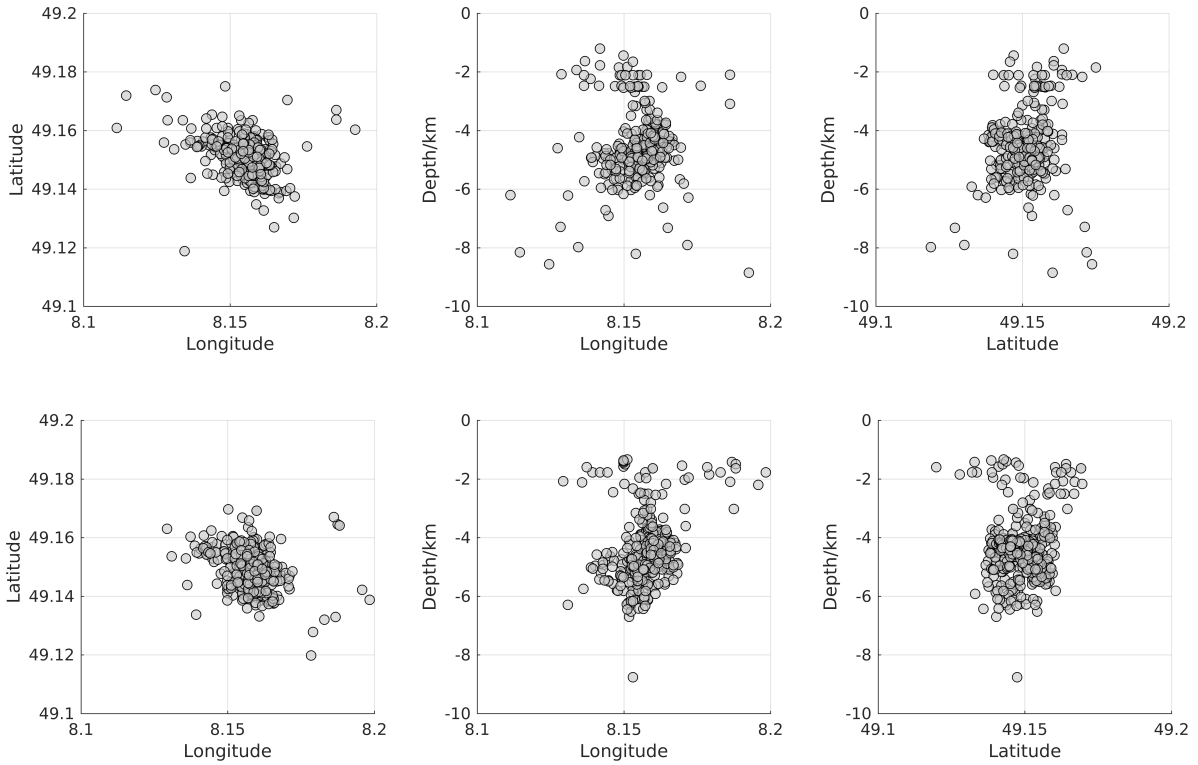

Figure 4.10.: Top view (left), North-Depth cross-section (center) and East-Depth-cross-section (right) of absolute hypocenter locations of 374 (92.4%) reliable hypocenters determined using manually and automatically read P- and S-wave arrival times and 371 (91.6%) manual most likely hypocenters considering P and S-wave arrival times.

Since the main data source of both locations processes are identical, the offsets are focused within $\pm 0.5km$ (Fig. 4.11). Consequently, the vast majority of relocated events are within the error ellipsoids of manual locations. Nevertheless, individual outliers spread up to $\pm 2km$ horizontally and $\pm 4km$ vertically. The previously identified trends for automatic relocations offsets are not recognizable. Since a few additional arrival times change the location results of the outlier so drastically, the reference manual locations appear to be unstable. This explains why large location offsets are at least partially within the manuals locations error ellipsoid.

Overall, approximately 90% of the relocated hypocenter using combined datasets are within close proximity ($< 1km$) to the manual locations (Fig. 4.12). The standard deviations of horizontal and vertical offsets are less than 1 km with a clear maximum between up to 200 m.

The results show that hypocenter locations derived from automatically determined phase arrival times tend to a higher variability than those from manual time readings. However, the majority of automatic locations are within the error ellipsoids of manual locations and consequently less separated than the manual location probability variance. Results show that the majority of manual error ellipsoids have maximum vertical extensions less than $\pm 1km$ and horizontal extensions

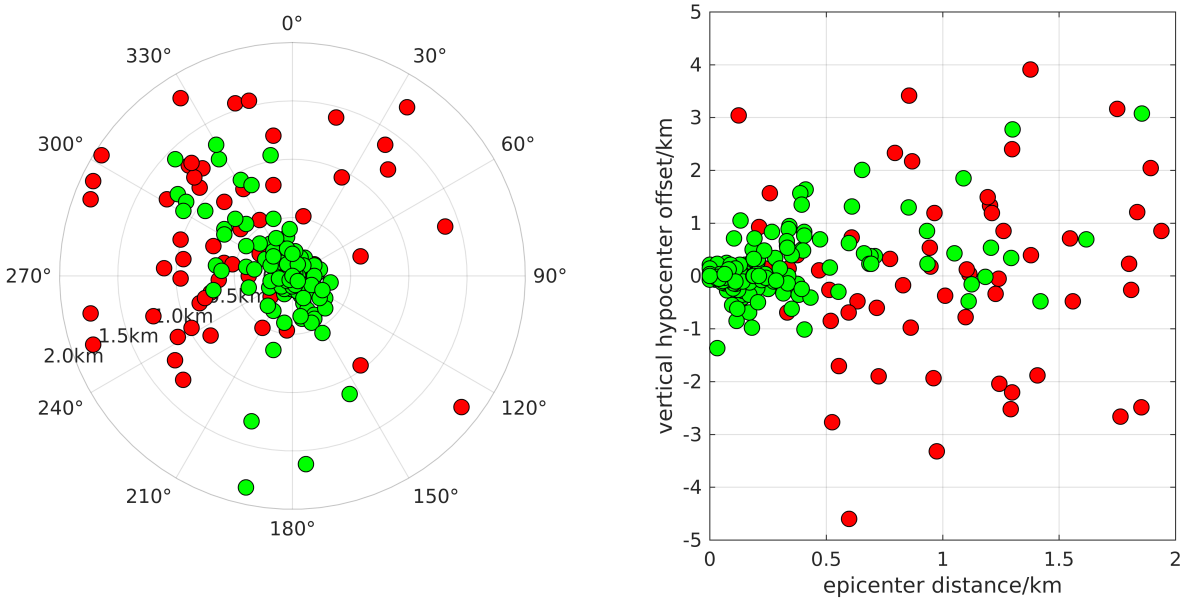

Figure 4.11.: Relative epicenter (left and right) and hypocenter depth (right) offsets between most likely locations from combined manually and automatically determined P- and S-picks and manual hypocenters using P- and S-wave arrivals. Green filling indicates that the hypocenters from combined datasets are within the manual location error ellipsoid and red filling indicates that the hypocenter is outside the ellipsoid, respectively.

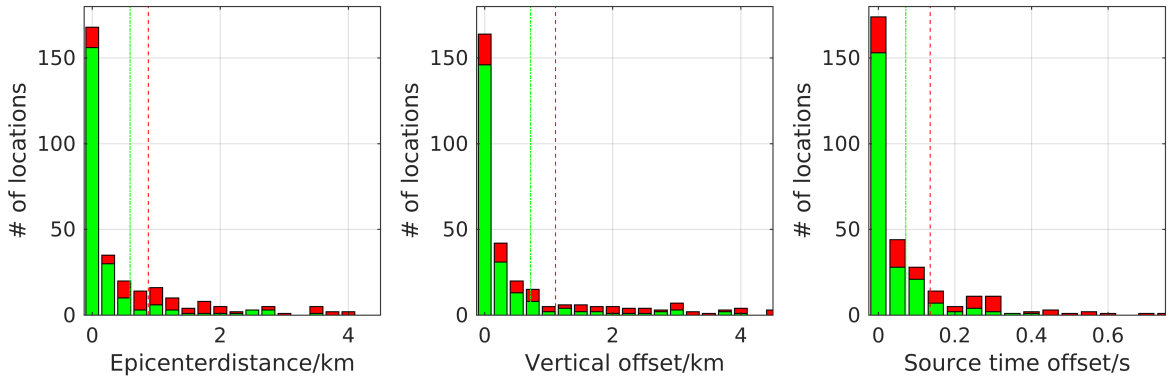

Figure 4.12.: Histograms of absolute epicenter (left), hypocenter depth (center) and source time (right) offsets between most likely locations from combined manually and automatically determined P- and S-picks and manual hypocenters using P- and S-wave arrivals. Green filling indicates that the hypocenters from combined databases are within the manual location error ellipsoid and red filling means that the hypocenter is outside the ellipsoid, respectively. The green and red lines indicate the standard deviations.

less than $\pm 2km$.

Including the induced S1-phase arrival times led to a more refined depth distribution of automatic locations on the one hand and a concentration of shallow hypocenters on the other hand. Since these shallow locations are observed for both, automatic and manual arrival time data, it is probable a result of an insufficient v_S-model. The preferred offset directions towards the

north-west/south-east as well as to shallower depth may be the result of a minor bias ($-0.02s$ between automatically and manually determined arrival times.

Finally, using the automatic phase time readings complementary to the manual pick catalog results in an overall better resolved source volume and a reduction of the shallow hypocenters. However, individual outlier are evidence for unstable location solutions. A Jack knife procedure should be able to identify these outliers and is hence recommended for further studies on this topic.

4.4. High-precision relative relocations

After comparing location results derived from automatically and manually determined phase arrival times, in this section relative earthquake locations are determined using the software HypoDD (Waldhauser and Ellsworth, 2000).

In order to retrieve relative locations for as many events as possible, travel time differences from manually read routine P1- and S1-phase arrival times as well as cross-correlations of phase arrivals are considered. The two fundamental assumptions for the double-difference relative relocations process are assumed to be fulfilled for the Insheim reservoir: event separations are expected to be small (<200 m) compared to event - stations offsets and lateral heterogeneities and since the events separations are small, the source region can be expected to have a homogeneous velocity.

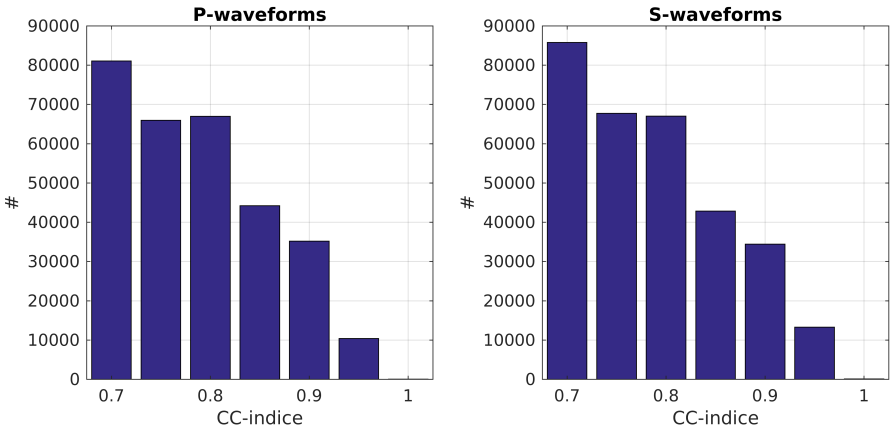

Figure 4.13.: Histogram of correlation indices determined between P1- (left) and S1-phase (right) waveforms of different events at individual stations.

P1- and S1-phase waveforms are cut over 0.6 s and 1 s around the phase arrival times to perform a cross-correlation. Fig. 4.13 shows the number of correlation indices for approximately 300,000 correlated P- and S-waveforms above $cc \geq 0.7$. Manually read arrival times and complementary automatically read arrival times are applied as the reference times for these correlation windows. The data is filtered applying a third order bandpass filter from 1 to 25 Hz. These parameters have been determined empirically. Further criteria to determine neighboring induced earthquake are:

- A maximum distance between event pair and stations of 15 km.
- A maximum hypocentral separation of 0.5 km.
- A maximum of 20 neighbors per event.
- At least 8 links required to define a neighbor.
- At least 8 and a maximum of 30 observations to be selected for each event pair.

- Case 1: Cross-correlation indices $cc \geq 0.7$ for P- and S-wave arrivals.
- Case 2: Cross-correlation indices $cc \geq 0.8$ for P- and S-wave arrivals.

The conjugate gradient method (LSQR, Paige and Saunders, 1982) is used to minimize the double-difference residuals for pairs of earthquakes at each station.

As starting location of the induced earthquakes, 405 routinely processed hypocenter locations by the company Bestec GmbH are used (Fig. 4.14). These hypocenters have been determined using the software VELEST including station corrections (pers. comm. Dr. L. Küperkoch, Bestec GmbH, Landau i.d. Pfalz, Germany). All hypocenters are found within a close range around production and injection wells of the Insheim power plant. The location depths range from -6 km to the well feet at approximately -3.5 km depth with a cluster of events ranging between -2.5 and -3 km depth.

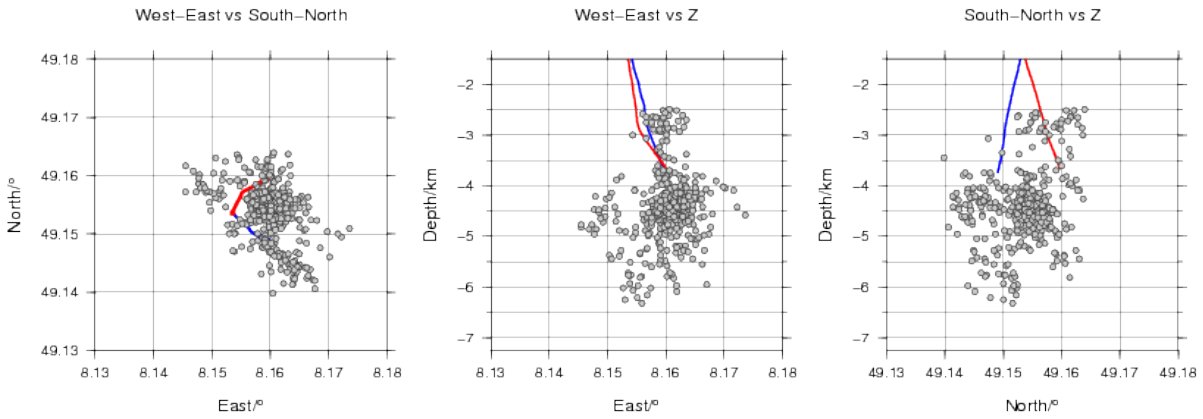

Figure 4.14.: Hypocenter locations in plane view and vertical sections of 405 Insheim earthquakes. The locations are derived from manually processed wave arrival times using the location software VELEST (pers. comm. Dr. L. Küperkoch, Bestec GmbH, Landau i.d. Pfalz, Germany).

In the first case ($cc \geq 0.7$) 399 of the 405 induced earthquakes are successfully relocated relative to neighboring events. The hypocenter distribution variance declines although the overall distribution does not change (Fig. 4.15). The shallow cluster of events (2.5 - 3 km depth) as well as individual deeper hypocenters (>5 km depth) are not observable anymore. Hypocenter locations are compressed to the volume between the injection and production wells in depths between -5 and -3.5 km. West of the main body of accumulated locations, a cluster of hypocenters remains while surrounding outliers are relocated closer to the wells.

Increasing the cross-correlation indices threshold to $cc \geq 0.8$ shows no significant changes in the distribution of hypocenters (Fig. 4.16). Minor differences along the edges of the main accumulation of hypocenters are apparent as well as a shift towards shallower hypocenter locations ($\approx 0.5km$). Consequently, an increase of the minimum correlation thresholds does not lead to a

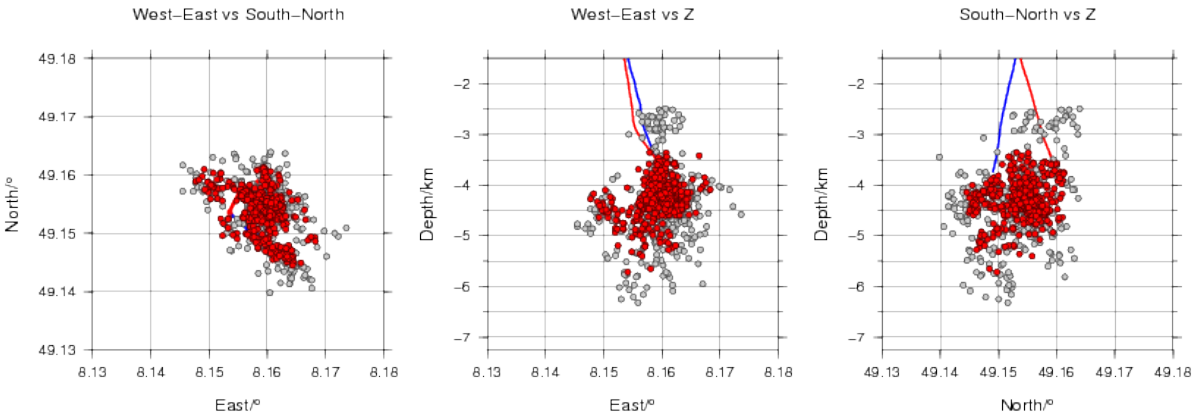

Figure 4.15.: Original hypocenters (gray) and double-difference relocations (red) in plane-view and vertical sections. Arrival time differences from absolute arrival time picks and relative times of P1- and S1-phase waveforms with $cc \geq 0.7$.

significant improvement of location precision.

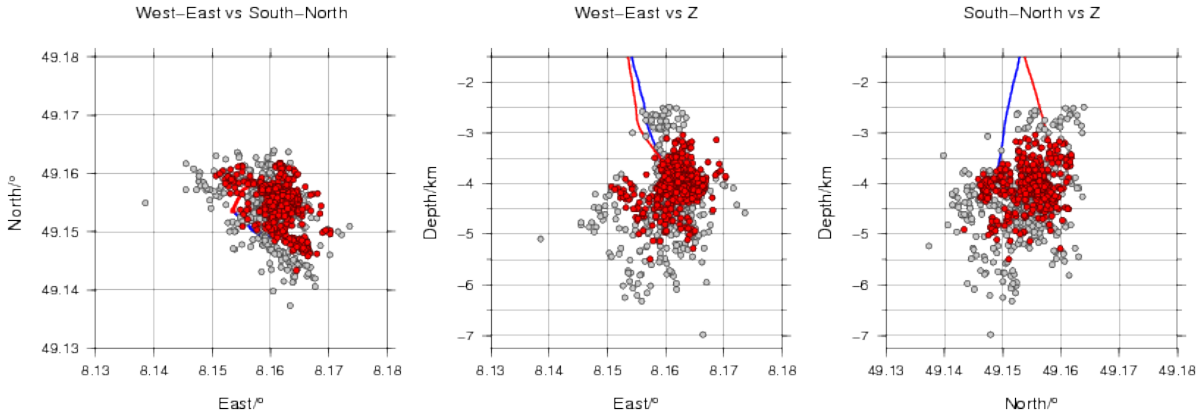

Figure 4.16.: Original hypocenters (gray) and double-difference relocations (red) in plane-view and vertical sections allowing arrival time differences from absolute arrival time picks and cross-correlations with indices $cc \geq 0.8$.

Since the relocated hypocenters do not vary significantly (<1 km) from the input locations and the main body of the hypocenter distribution remains approximately the same, the routine locations can be described as reliable.

An application of the double-differential relocation removes the shallow cluster as an artifact. In consistency with the observation from the previous section, the shallow locations are likely introduced by the 1D-velocity model approximation of shear wave model. A cluster west of the wells at 8.15° is verified by relative relocations. Instead of a depth variation from -2.5 to -6.5 km the relative hypocenters are distributed between -3 and -5 km depth. The remaining horizontal variation of epicenters is less than 1.5 km and positioned between the two production and injection wells.

4.5. Discussion and conclusion

Two aspects of the relocations processes have been investigated in this chapter. While the first one addresses the automatic processing aspect, the second part aims to optimize hypocenter locations and to retrieve geothermal reservoir information.

Applied location methods are up to date and continuously used in publications. For this reason, possible inaccuracies of these algorithms are not discussed in detail. However, two aspects must be mentioned. Investigating the relative offsets of probabilistic most likely locations has one major flaw. The most likely hypocenters are not necessarily at the center of the error ellipsoids nor within the error ellipsoids at all. The interpretation that the error ellipsoids of manual relocations are very large is thus only valid if the manual most likely locations are positioned in or close-by the actual ellipsoid centers. Nevertheless, the error ellipsoids are statements on the uncertainty incorporating possibly multi-modal probability location distributions. Thus, even if the most likely hypocenters are separated from the ellipsoid center or even outside the ellipsoid, the locations probability distributions can be unstable (multi-modal) or have a large error ellipsoid in other orientations.

The observed hypocenter offsets between automatic and manual locations are small enough to result from small arrival time pick errors or changing spatial data coverage. Especially the northwest to south-east running preferred offset direction, which is observed for P- and S-wave arrival time data, indicates that the resolution in this azimuths change between the datasets. Although the manual locations appear horizontally and vertically well refined, the stability of these locations is questionable considering the low total number of available arrival times for some events.

Furthermore, single large-offset hypocenter outliers in horizontal as well as vertical directions may have another cause. The automatic arrival time error estimation may allow individual unreliable arrival time picks. In case of low total number of arrival times this may lead to large variation in hypocenter locations or unstable multi-modal probability functions. Relocated hypocenters from small numbers of manual arrival times complemented with single individual automatic picks coincide with outstanding large hypocenter offsets. This support the unstable manual location assumption.

Finally, the resulting approximately 1 km standard deviations of hypocenter offsets account for different manually and automatically determined arrival time datasets. Therefore a subsequent study using arrival times of the same stations for the relocation should provide less biased offsets. Nevertheless, excluding outlying hypocenter location, using the automatically determined arrival times as a complementary dataset results in a better resolved location volume. Manually processing of standard dataset of the best SNR stations in combination with automatically de-

termined arrival times may be able to reduce the manual processing workload while being able to reproduce results of similar or even higher precision. Such a procedure could be tested in a similar study based on these results.

Since a remaining uncertainty is still too large to resolve a seismically active structure like a fault, the double-difference method provides a useful tool to improve at least the relative location accuracy of induced earthquakes. Although the number of included cross-correlation arrival time differences decreases by one third if the threshold is raised from $cc \geq 0.7$ to $cc \geq 0.8$, the relative locations do not vary significantly. This can be an indication, that the number of absolute arrival times, which are taken into account, are too dominant. However, the overall number of cross-correlation time lags is large. Therefore, it is more likely that the time lags are consistent with arrival time differences and the main reason for reduced cross-correlation indices are lower SNR. Thus, the neighboring event combinations vary insignificantly.

Although the variance of locations is reduced strongly, the hypoDD-relocations do not fully resolve the fault system within the Insheim reservoir. However, induced seismicity locations extend from injection to production well and vertically from -5 to -3 km depth. A cluster of events east of the production well is recognizable as a differentiable seismic feature. Seismic activity at the production well is counter intuitively since a pore pressure reduction in the wells vicinity is expected. However, one of the events relocated at the well feet shows a signal in the production pressure recording indicating that its hypocenter is in the immediate vicinity (pers. comm. Dr. L. Küperkoch, Bestec GmbH, Landau, Germany). This supports the absolute hypocenter relocations found in this study. Thus, while the locations appear to be precise, the lack of observed fault geometry indicates a complex fracture structure in the reservoir.

A benefit of location processes including automatically determined arrival times has been pointed out. However, in order to map the reservoir from induced events locations absolute locations are insufficient due to the large hypocenter variations. On the contrary, relative relocations are able to reduce the variation and determined the seismicity in the volume between the Insheim wells.

An interpretation of the seismic reservoir behavior follows in the next section including the cluster analysis determined by the similarity detector in Chapter 2.4.3 and the here discussed relative relocations.

5. Interpretation of the seismic behavior at the Insheim reservoir

Three processing steps are discussed in this thesis: the similarity detection of induced seismicity, the automatic phase arrival time determination using an AR-AIC-costfunction approach and the relocation of induced earthquakes. Objectives of the automatic processing are to provide reliable results with improved or at least comparable accuracy to manual processing.

In this section, the performance of the automatic processing is briefly summarized before the results are interpreted regarding the geothermal reservoir Insheim. Since the location precision of the Landau induced seismicity is rather low and no plant operational information are shared, the Landau reservoir is excluded from the interpretation.

5.1. Summary of performance of automatic processing

Based on the requirement for complete seismic catalogs for geodynamic modeling purposes and for the hazard risk assessment, detection algorithms are essential. Since it is one of the oldest topics in seismology, plenty of approaches exist. The applicability and sensitivity of algorithms depends on the settings. A complementary similarity approach has been successfully applied to the induced seismicity at Landau and Insheim. High similarities among induced earthquake waveforms give hints on close hypocenter locations and related source processes. The approach to use multiple master events per reservoir identifies 20 earthquake clusters at the Insheim and 12 clusters at the Landau reservoir. These cluster point out temporal changing seismic characteristics at both reservoirs. Furthermore, the re-occurrence of swarm events is observed at the Landau reservoir. In comparison to other detection catalogs, 70-90/680 newly found induced earthquakes at the Insheim/Landau reservoir and the ability to perform a cluster analysis provides a good argument for this algorithm to be used in addition to online detection algorithms.

Following the detection, an automatic picking algorithm is proposed and applied to a teleseismic as well as to the induced dataset of the geothermal reservoirs Landau and Insheim. Since an AR-AIC approach by (Küperkoch et al., 2012) is more sensitive than HOS- or STA/LTA-based algorithms, we use the AR-prediction error of the waveform and the AIC to identify wave arrivals. In order to simplify the applicability to different seismic phases as well as the parameter training of the algorithm to new datasets, a cost function provides an excellent tool. Its application to teleseismic mantle phases results in residuals to manual arrival time readings with standard de-

viations of $\pm 0.47s$ for P- and $\pm 4.54s$ for S-waves, respectively. Regarding the induced seismicity, the residuals' standard deviations are lower with $\pm 0.02 - 0.03s$ for P-waves and $\pm 0.07 - 0.08s$ for S-waves. A systematic cost function training, a consistent manually read arrival time database and higher frequencies are reasons for the much lower standard deviations of the induced seismic phases. Since the same parameter training results in slight negative shifts ($-0.02s$) for Insheim S-wave residuals and a positive shift ($+0.05s$) for Landau S-wave residuals, the first arriving S-phase waveforms between both reservoirs are expected to differ significantly.

Determined phase arrival times are applied to relocate the induced earthquakes. Aim of this analysis is to understand how consistent and accurate locations from automatically determined phase arrival times are. The majority of relative hypocenter offsets are less than 2 km with a standard deviation of approximately 1 km independent of the considered seismic phases. Consequently, automatically determined arrival time data provide overall consistent results although individual hypocenters are falsely located. If automatically determined arrival times are used as complementary database, similar outliers are observed. The conclusion from these findings is that the probability density functions are bi- or multi-modal and therefore highly sensitive to individual added or removed arrival times and azimuthal coverage. Nevertheless, the main concentration of hypocenter locations is better outlined if automatically determined phase arrival times are included complementary to manual picks.

Finally, hypoDD-relative relocations of induced Insheim earthquakes are determined to improve location accuracy. While the fault system is not resolved by the relative hypocenter relocations, the volume including hypocenters is reduced to the range between the injection and the production well at depths between 3 and 5 km and individual clusters at the production well and west off it can be distinguished.

5.2. Interpretation of seismic behavior at the Insheim reservoir

Besides the performance of automatic processing in comparison to manual processing results, insights into the seismic behavior of the Insheim reservoir are gained in this thesis. In the following, learnings from the previously presented processing steps are combined and interpreted.

While the hypoDD-relative relocations provide sufficient precision to differentiate two seismicity clusters from hypocenter locations, the combination of detected clusters and relative locations is able to distinguish more earthquake groups spatially (Fig. 5.1). For at least eleven of the detected clusters of similar events accumulations of hypocenters are observed: at the injection well (green), south-east off the injection well (navy blue), 1 to 2 km beneath the injection well (light blue), at the production well (blue), between the production and injection wells (light green, orange, red, yellow, dark blue) and west off the production well (azure).

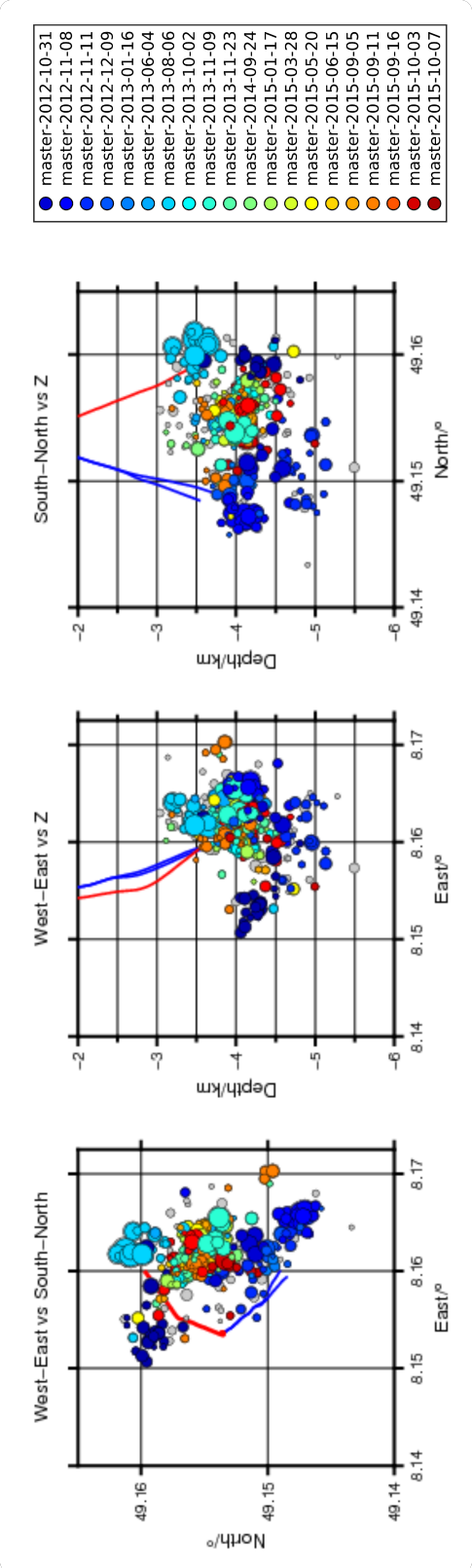

Figure 5.1.: HypoDD relative relocations (circles) and magnitudes (Ml, Bestec catalog) of 395 induced earthquakes at the Insheim reservoir. Colors indicate the affiliation to 20 Insheim clusters determined from similarity detection.

The majority of detected earthquakes are less than 300 m away from the corresponding relocated similar master event hypocenter, for $cc \geq 0.9$ even less than 150 m. While earthquakes of the blue marked clusters show an increasing hypocenter offset with declining similarity, earthquakes of the clusters in between the wells (yellow, red, orange) have low offsets ($< 200m$) for all shown similarity values. Assuming that the relative relocations have a resolution better than approximately 100 m, the earthquake hypocenters of clusters close to the wells (blueish) vary over time. On the contrary, earthquakes of clusters in between the wells (light green, yellow, red, orange) are re-occurring at approximately the same source locations with possibly slightly alternating mechanisms.

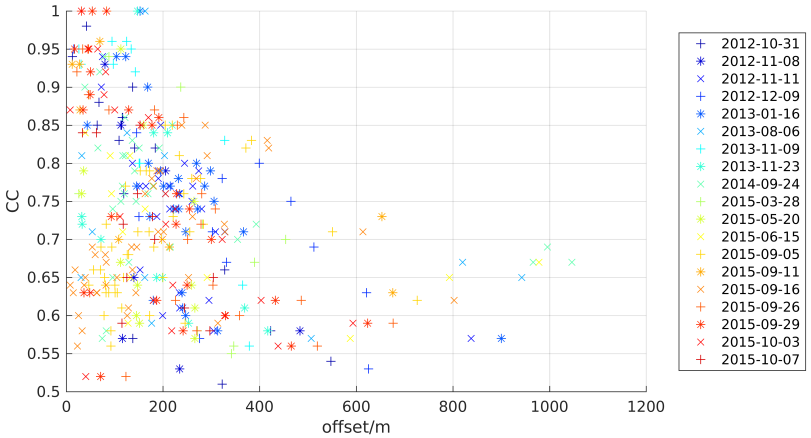

Figure 5.2.: Hypocenter offsets of detected and relative relocated cluster earthquakes to corresponding master events against the maximum station correlation between the detected event and master event *cc*.

The temporal distribution of seismicity in the individual clusters and the hypoDD-relocations of the cluster events indicate a migration of seismicity over time. Blue marked clusters are associated to early master events (before 2014) and thus to an early production stage. Similar to earthquakes induced during stimulation of rocks at other geothermal plants (e.g. Basel or Soultz-sous-Forêtz, Bachmann et al., 2011; Grünthal, 2014; Zang et al., 2014), the events at the beginning of production are likely dominated by the local increase of pore pressure, the reduction of effective normal stress and hence fault-slip. Since the injection pressure during production is much lower than during stimulation (pers. comm. Dr. L. Küperkoch, Bestec GmbH, Landau i.d. Pfalz, Germany), the fracturing of rock in the immediate vicinity of the injection well due to rapid pressure perturbations, as observed by Bachmann et al. (2012) at Basel, is unlikely.

The seismicity at the production well feet is characterized by the largest magnitudes registered at the Insheim reservoir ($\leq Ml2.1$). Mechanisms associated with fluid extraction like elastic impoundment (e.g. Kisslinger, 1976) of the reservoir rock or the locking and stick-slip of formerly creeping faults (e.g. Segall and Fitzgerald, 1998) are questionable in this case. Impoundment related seismicity is expected in the material surrounding the reservoir while the cluster, as far as

the absolute positions of the relocations are correct, is situated at the production well foot. Since the cluster occurs within the first year of production, a creeping fault must have been creeping at a significant rate to release the seismic energy of several events with magnitudes between Ml1.5 and Ml2. Thus, an alternative mechanism which is not documented at other geothermal systems to our notice so far is required to explain these earthquakes.

A possible solution approach could be a sort of backlog of fluids at the well foot. During production a stable production pressure creates a pressure gradient in the rock surrounding the production well foot. Fluids flow from the surrounding rock towards the well. This flow creates local enhanced pore-pressure regimes and thus may lead to the nucleation of earthquakes close to the production well. Such an enhanced pore-pressure can be cause by local variations of reservoir rock permeability and the induced seismicity indicates the opening of pathways towards the well. Furthermore, especially the large magnitudes indicate that fluids may be flowing through stressed fault interfaces which have been dry or at least contained less fluids.

Induced events located deeper than the actual reservoir has been observed at other geothermal plants as well (e.g. Basel or The Geysers, Bachmann et al., 2011; Eberhart-Phillips and Oppenheimer, 1984). Minor changes in the pressure regime can drive the fluid into deeper regions where higher pore pressure together with stress corrosion might trigger earthquakes (Kisslinger, 1976). Thus, the tendency to deeper events below the Insheim injection well can be explained. However, the number of earthquakes in depths around 4.5 to 5 km is rather small and the magnitudes less than Ml1. These cluster play thus only a minor role for seismicity interpretation and seismic hazard assessments.

The cluster west off the production well is another distinct feature. Activity at this location is focused at the beginning of injection (Fig. 5.3). The isolated location and the early activity period indicate that this seismicity is related to a fast propagation of fluids from the injection well. While the main distribution direction of seismicity is oriented north-south, a secondary strike may be interpreted from south-east (navy blue/orange cluster) to this isolated cluster in the north-west (azure cluster).

While the primary orientation of seismicity reflects the currently dominant stress regime in the URG, the southeast-northwest branch coincides with the approximate extensional direction of the URG rift valley. Consequently, this cluster could be evidence for two crossing fault systems of which the secondary fault (north-west to south-east) is characterized by seismicity during early operation stages. While no precise fault geometries are available for the immediate vicinity of the Insheim reservoir, both fault orientations are observed in the northern URG (Illies and Greiner, 1978; Peters and van Balen, 2007).

The permeability on fault surfaces is expected to be larger and therefore fluids under pressure migrate faster along the interfaces. This could explain why this cluster, which is far-off the injec-

tion point, is triggered already after short production time ($< 1month$) whereas other clusters between the wells show main activity between 2013 and 2016. The fact that various clusters can be differentiated within a small volume may be another indication for differently oriented fracture systems. Differing source mechanisms would be a simple explanation for dissimilar waveforms of events with low hypocenter separations.

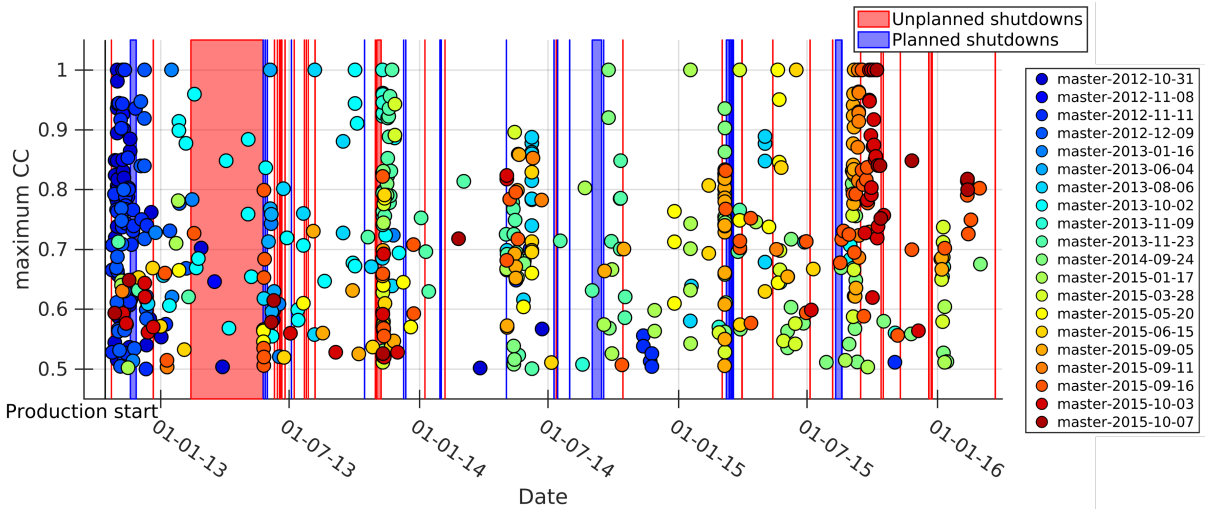

Figure 5.3.: HypoDD relative relocations (circles) and magnitudes (Ml) of 395 Insheim events. Colors indicate the events cluster affiliation determined from similarity detection with the corresponding cross correlation indices (cc).

From 2012 to 2016 the Insheim power plant has stopped production several times. At planned downtimes, the production has been reduced step-wise whereas failures of systems resulted in accidental shut-ins and thus unplanned downtimes (pers. comm. Dr. L. Küperkoch, Bestec GmbH, Landau i.d. Südpfalz). The distribution of seismicity in reference to planned and unplanned downtimes of the Insheim power plant reveals that enhanced seismic energy release occurs after production re-starts. However, a strict correlation is not revealed since some downtime periods are not followed by any seismicity while after others an intense seismic response of the reservoir is detected. This observation accounts for both planned and accidental shut-ins.

After a planned eight day shut-down in August 2015, a sequential activation of different clusters is observed. Following earthquakes at the green and blue clusters between the wells, events of the yellow, orange and red clusters (between the wells) are triggered within one month. While a slowly propagating pore-pressure frontier after the re-start of production is a likely explanation, the small cluster separations and the consequent activation may also indicate subsequent failures of different volumes triggered each by previous clusters. Considering that this systematic migration over a short periods is observed only once, an analysis on production parameters may give information on enhanced injection pressure after the start-up or similar relations to production parameters.

Nevertheless, the long-term migration of seismicity from the injection point towards the production well indicates that fluid pathways are created by a propagating pore-pressure front such that segment after segment between the wells reaches critical pore-pressure and thus fault-slip earthquake nucleation. Since no real reservoir stimulation is performed, fracture extensions due to an initial steep pressure rise at the well is unlikely to occur. This is supported by the over time declined seismicity at the injection well where, according to the Kaiser effect, no earthquakes nucleate until a higher pressure than before is induced.

Finally, in order to characterize the seismic response of the Insheim reservoir, Fig. 5.4 and 5.5 show the relative source times of induced earthquakes at the Insheim reservoir after the last preceding production shut-in or last preceding production re-start, respectively. After shut-ins the overall detected seismicity declines. Therefore, only a few events occurred during the actual downtimes. In case of planned shut-ins the events occur up to 10 days after the controlled reduction of production, whereas the reservoir remains seismically active for more than a month following accidental shut-ins. However, the total number of events detected during downtime periods is low and the single cluster (azure) identified before may bias this result.

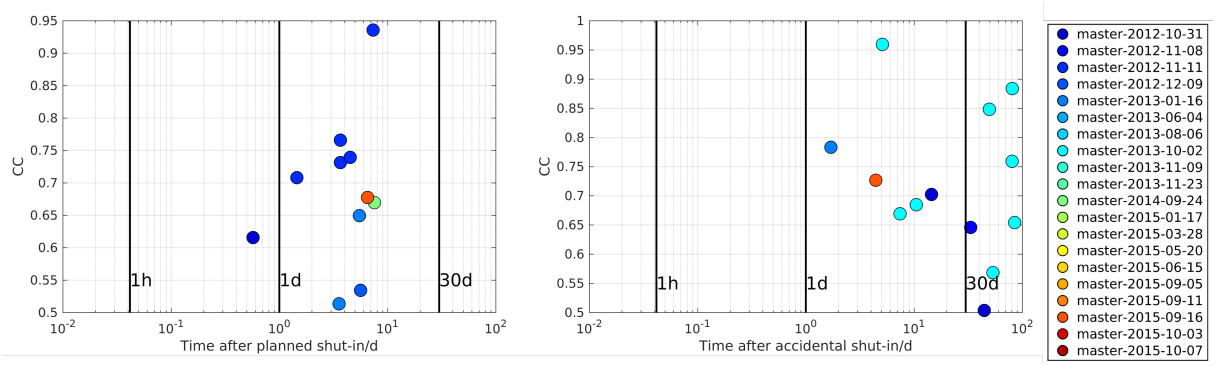

Figure 5.4.: Relative source times of induced earthquakes at the Insheim reservoir after controlled (left side) and unplanned (right) shut-ins of the Insheim geothermal power plant. Only events before the re-start of production are considered. The colors indicate the cluster to which the events can be assigned by the cross-correlation indices on the y-axis.

Following the start-up of production, the reservoir responds differently whether the production was was decreased regulated or shut-in accidentally due to a system malfunction. After planned downtimes, the first infrequently occurring earthquakes are detected after 2.5 hours. In the following, the number of events increases and shows temporal maximum intensity between 10 to 30 days after production start. Following accidental shut-ins on the other side, nearly no induced seismicity is observed within the first day after the production re-start.

Since approximately the same production starting procedure is performed whether the shut-in was planned or unplanned, it is likely that the regulated shut-down reduces the effective stress in the reservoir. Early earthquakes after start-up may then be the result of step-wise pore-pressure increases in the reservoir. The main seismicity though starts only after more than 10 days. On

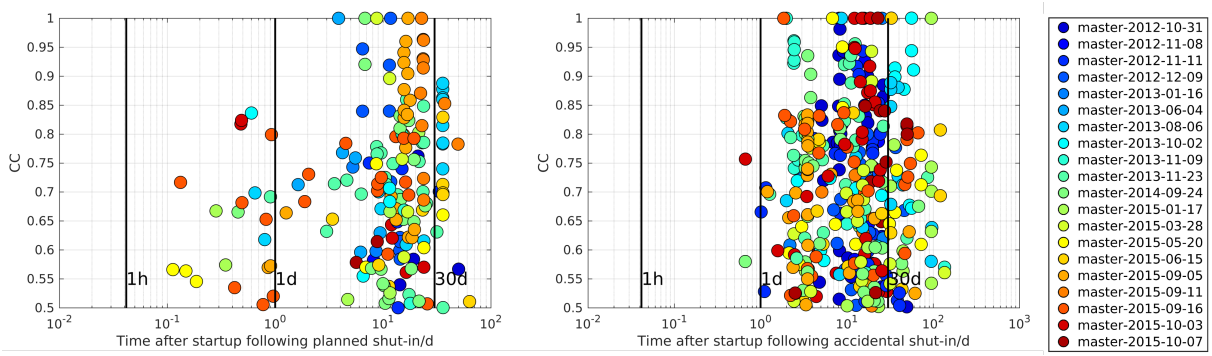

Figure 5.5.: Relative source times of induced earthquakes at the Insheim reservoir after re-start of production at the Insheim power plant following controlled (left side) and unplanned (right) down times. The colors indicate the cluster to which the events can be assigned by the cross-correlation indices on the y-axis.

the contrary, the sudden shut-in of production leaves the reservoir in a high stress situation such that enhanced seismicity starts only two days after production re-start.

Finally, first steps in understanding seismicity in geothermal systems in the northern URG are taken. The automatic processing approaches prove to be useful providing consistent results although showing higher variation if sparse data coverage is available. Nevertheless, especially the similarity detection analysis provides a good assessment to induced seismicity with poor background data.

Concluding, several hints are identified that the majority of induced earthquakes at the Insheim geothermal reservoir are triggered by enhanced pore pressure due to injection. However, the earthquake cluster at the production well requires special notice since formerly proposed fluid extraction mechanisms do not fit. In order to understand the effect of earthquake nucleation here, a study connecting operational and reservoir rock parameters is required. Verifying that the backlog of fluids flowing towards the well can trigger earthquake nucleation with magnitudes up to Ml2.1 needs laboratory experiments and hydro-geological modeling studies.

The result of relative hypocenter relocations and the distinguishable clusters with low hypocenter earthquake separations indicate complex fault geometries of which two overall directions can be distinguished but no individual lines can be mapped. Thus, it is likely that the earthquakes occur on a web of fractures which follow the main fault orientations. One segment follows the URG rift valley orientation while the other is oriented according to the younger stress regime resulting from the Alpine denudation. The consequential interpretation that two differently oriented faults are intersecting at the reservoir is ambiguous, although spatial and temporal distribution of seismicity favor it. Nevertheless, additional studies are necessary to verify the existence and resolve the geometry of these fracture webs. The activation of clusters over time from injection towards the extraction point may coincide with a loss of energy production efficiency in future. If these clusters map the fluid pathways creation, cold reinjected fluid may migrate faster to the

production well and thus decrease the production temperature. However, approximate stationarity of earthquakes in the clusters between the wells indicates that the pressure front is currently not strong enough to initiate fracture opening beyond this volume.

The Landau and Insheim power plants are currently the only operating geothermal power plants in the German part of the URG. Since the failure of the Basel EGS in 2006, the understanding of induced seismicity in deep geothermal systems has become essential for this industry. Determining the inducing mechanism at the Insheim production well may be able to reliably identify maximum magnitudes that are likely to occur in this reservoir. Furthermore, the automatic processing steps proposed here are able to reduce the routine monitoring workload and provide resources for further seismic analysis, e.g. focal mechanisms or stress release calculations.

6. Acknowledgments

Ich danke Thomas Meier, der mich in den letzten drei Jahren betreut hat. Seine herzliche Art, mitreißende Begeisterung und seine Geduld Wissen zu vermitteln führten zum Gelingen dieser Arbeit.

Ich danke Ludger Küperkoch, der mich erst als Mentor und später auch als Kollege und Freund begleitete. Er begeisterte mich für die Thematik und war stets ein guter Gesprächspartner für seismologische und nicht-seismologische Themen.

Auch meinem Kollegen Christian Weidle möchte ich danke. Er bot mir in den letzten Jahren stets ein offenes Ohr für Probleme, Ideen und ein Schnack beim Mittagessen.

Für ihre liebevollen Korrekturen, Motivation und ihre Freundschaft möchte ich Nadine Mengis danken. Sie ist mir nicht nur eine gute Freundin sondern von ihren Anlagen her die fähigste Wissenschaftlerin, die ich kenne.

My thanks goes to my dear colleague and office mate Marija Ruščić. Many long productive chats, exchanges of opinions, ideas, jokes and hundreds desk-delivered coffees deserve all my gratitude.

Ich danke meinen Eltern, meinen Geschwistern und ihren Partnern für ihre fortwährende Unterstützung und die Ablenkung in den richtigen Momenten.

Ich danke Florian Schütte und Rebecca Hummels. Sie standen mir mit Hilfsbereitschaft und Freundschaft in den stressigsten Phasen zur Seite.

Zu guter Letzt danke ich Anna-Marie Schütte. Ich danke ihr für ihre unerschütterliche Geduld im Umgang mit meiner Prokrastination, das rücksichtsvolle Übernehmen der vielen, vielen Dinge, die ich im Alltag liegen ließ und ihren liebevollen Umgang mit meinen wirren Gedankengängen nach durchgearbeiteten Nächten.

References

Akaike, H. (1973). Maximum Likelihood Identification of Gaussian Autoregressive Moving Average Models. *Biometrika*, 60(2):255–265.

Aldersons, F. (2004). *Toward a Three-Dimensional Crustal Structure of the Dead Sea region from Local Earthquake Tomography*. PhD-Thesis, Tel-Aviv University.

Allen, R. (1982). Automatic phase pickers: Their present use and future prospects. *Bulletin of the Seismological Society of America*, 72(6B):S225–S242.

Allen, R. V. (1978). Automatic earthquake recognition and timing from single traces. *Bulletin of the Seismological Society of America*, 68(5):1521–1532.

Allis, R. (1982). Mechanism of induced seismicity at The Geysers geothermal reservoir, California. *Geophysical research letters*, 9(6):629–632.

Anstey, N. A. (1966). The sectional auto-correlogram and the sectional retro-correlogram *. *Geophysical Prospecting*, 14(4):389–426.

Aster, R. C. and Scott, J. (1993). Comprehensive characterization of waveform similarity in microearthquake data sets. *Bulletin of the Seismological Society of America*, 83(4):1307–1314.

Augliera, P., Cattaneo, M., and Eva, C. (1995). Seismic multiplets analysis and its implication in seismotectonics. *Tectonophysics*, 248(3):219 – 234.

Bachmann, C. E., Wiemer, S., Goertz-Allmann, B. P., and Woessner, J. (2012). Influence of pore-pressure on the event-size distribution of induced earthquakes. *Geophysical Research Letters*, 39(9):n/a–n/a.

Bachmann, C. E., Wiemer, S., Woessner, J., and Hainzl, S. (2011). Statistical analysis of the induced basel 2006 earthquake sequence: introducing a probability-based monitoring approach for enhanced geothermal systems. *Geophysical Journal International*, 186(2):793.

Baer, M. and Kradolfer, U. (1987). An automatic phase picker for local and teleseismic events. *Bulletin of the Seismological Society of America*, 77(4):1437–1445.

Bai, C.-Y. and Kennett, B. L. N. (2000). Automatic Phase-Detection and Identification by Full Use of a Single Three-Component Broadband Seismogram. *Bulletin of the Seismological Society of America*, 90(1):187–198.

Baillard, C., Crawford, W. C., Ballu, V., Hibert, C., and Mangeney, A. (2013). An Automatic Kurtosis-Based P- and S-Phase Picker Designed for Local Seismic Networks. *Bulletin of the Seismological Society of America*, 104(1):394–409.

Baisch, S., Ceranna, L., and Harjes, H.-P. (2008). Earthquake Cluster: What Can We Learn from Waveform Similarity? *Bulletin of the Seismological Society of America*, 98(6):2806–2814.

Bertani, R. (2016). Geothermal power generation in the world 2010 - 2014 update report. *Geothermics*, 60:31 – 43.

Bommer, J. J., Oates, S., Cepeda, J. M., Lindholm, C., Bird, J., Torres, R., Marroquín, G., and Rivas, J. (2006). Control of hazard due to seismicity induced by a hot fractured rock geothermal project . *Engineering Geology*, 83(4):287 – 306.

Bondár, I., Myers, S. C., Engdahl, E. R., and Bergman, E. A. (2004). Epicentre accuracy based on seismic network criteria. *Geophysical Journal International*, 156(3):483.

Bönnemann, C., Schmidt, B., Ritter, J., Gestermann, N., Plenefisch, T., Wegler, U., Schulz, R., Heidbach, O., Erbas, K., Baisch, S., et al. (2010). Das seismische Ereignis bei Landau vom 15. August 2009. *Abschlussbericht der Expertengruppe „Seismisches Risiko bei hydrothermaler Geothermie“. Hannover2010*, page 55.

Bounif, A., Dorbath, C., Ayadi, A., Meghraoui, M., Beldjoudi, H., Laouami, N., Frogneux, M., Slimani, A., Alasset, P. J., Kharroubi, A., Ousadou, F., Chikh, M., Harbi, A., Larbes, S., and Maouche, S. (2004). The 21 May 2003 Zemmouri (Algeria) earthquake Mw 6.8: Relocation and aftershock sequence analysis. *Geophysical Research Letters*, 31(19).

Catalli, F., Meier, M.-A., and Wiemer, S. (2013). The role of Coulomb stress changes for injection-induced seismicity: The Basel enhanced geothermal system. *Geophysical Research Letters*, 40(1):72–77.

Catalli, F., Rinaldi, A. P., Gischig, V., Nespoli, M., and Wiemer, S. (2016). The importance of earthquake interactions for injection-induced seismicity: Retrospective modeling of the Basel Enhanced Geothermal System. *Geophysical Research Letters*, 43(10):4992–4999.

Charléty, J., Voronin, S., Nolet, G., Loris, I., Simons, F. J., Sigloch, K., and Daubechies, I. C. (2013). Global seismic tomography with sparsity constraints: Comparison with smoothing and damping regularization. *Journal of Geophysical Research: Solid Earth*, 118(9):4887–4899.

Cristiano, L., Meier, T., Krüger, F., Keers, H., and Weidle, C. (2016). Teleseismic P-wave polarization analysis at the Gräfenberg array. *Geophysical Journal International*, 207(3):1456.

Crotwell, H. P., Owens, T. J., and Ritsema, J. (1999). The TauP Toolkit: Flexible Seismic Travel-time and Ray-path Utilities. *Seismological Research Letters*, 70(2):154–160.

Dahlen, F. A., Hung, S.-H., and Nolet, G. (2000). Fréchet kernels for finite-frequency traveltimes - I. Theory. *Geophysical Journal International*, 141(1):157.

Dahm, T., Becker, D., Bischoff, M., Cesca, S., Dost, B., Fritschen, R., Hainzl, S., Klose, C., Kühn, D., Lasocki, S., Meier, T., Ohrnberger, M., Rivalta, E., Wegler, U., and Husen, S. (2012). Recommendation for the discrimination of human-related and natural seismicity (Letter to the Editor). *Journal of Seismology*, 17:197–202.

Deichmann, N. and Giardini, D. (2009). Earthquakes Induced by the Stimulation of an Enhanced Geothermal System below Basel (Switzerland). *Seismological Research Letters*, 80(5):784–798.

Di Stefano, R., Aldersons, F., Kissling, E., Baccheschi, P., Chiarabba, C., and Giardini, D. (2006). Automatic seismic phase picking and consistent observation error assessment: application to the Italian seismicity. *Geophysical Journal International*, 165(1):121–134.

Diehl, T., Kissling, E., Husen, S., and Aldersons, F. (2009). Consistent phase picking for regional tomography models: application to the greater Alpine region. *Geophysical Journal International*, 176(2):542–554.

Douglas, A. (1967). Joint Epicentre Determination. *Nature*, 215:47–48.

Douglas, A., Bowers, D., and Young, J. B. (1997). On the onset of P seismograms. *Geophysical Journal International*, 129(3):681–690.

Earle, P. S. and Shearer, P. M. (1994). Characterization of global seismograms using an automatic-picking algorithm. *Bulletin of the Seismological Society of America*, 84(2):366–376.

Eberhart-Phillips, D. and Oppenheimer, D. H. (1984). Induced seismicity in the geysers geothermal area, california. *Journal of Geophysical Research: Solid Earth*, 89(B2):1191–1207.

Ellsworth, W. L. (2013). Injection-Induced Earthquakes. *Science*, 341(6142):1225942–1225942.

Engdahl, E. R. and Ritzwoller, M. H. (2001). Crust and upper mantle P- and S-wave delay times at Eurasian seismic stations. *Physics of the Earth and Planetary Interiors*, 123(2-4):205–219.

Engdahl, E. R., van der Hilst, R., and Buland, R. (1998). Global teleseismic earthquake relocation with improved travel times and procedures for depth determination. *Bulletin of the Seismological Society of America*, 88(3):722–743.

Federal Association Geothermal Energy (2017). Tiefe Geothermieprojekte in Deutschland. Technical report, Federal Association Geothermal Energy.

Federal Ministry for Economic Affairs and Energy (BMWi) (2016). Renewable Energy Sources in Figures. Technical report, BMWi, Berlin, Germany.

Federal Ministry for Economic Affairs and Energy (BMWi), Federal Ministry for the Environment, Nature Conservation and Nuclear Safety (BMU) (2011). The Federal government's energy concept of 2010 and the transformation of the energy system of 2011. Technical report, Federal Ministry of Economics and Technology and Federal Ministry for the Environment, Berlin.

Flanagan, M. P., Myers, S. C., and Koper, K. D. (2007). Regional Travel-Time Uncertainty and Seismic Location Improvement Using a Three-Dimensional a priori Velocity Model. *Bulletin of the Seismological Society of America*, 97(3):804–825.

Freiberger, W. F. (1963). An approximate method in signal detection. *Quarterly of Applied Mathematics*, pages 373–378.

Fuchs, K., Bonjer, K.-P., Gajewski, D., Lüschen, E., Prodehl, C., Sandmeier, K.-J., Wenzel, F., and Wilhelm, H. (1987). Crustal evolution of the Rhinegraben area. 1. Exploring the lower crust in the Rhinegraben rift by unified geophysical experiments. *Tectonophysics*, 141(1):261 – 275.

García, L., Alvarez, I., Benítez, C., Titos, M., Bueno, A., Mota, S., de la Torre, A., Segura, J. C., Alguacil, G., Díaz-Moreno, A., Prudencio, J., García-Yeguas, A., Ibáñez, J. M., Zuccarello, L., Cocina, O., and Patané, D. (2016). Advances on the automatic estimation of the P-wave onset time. *2016*, 59(4).

Geiger, L. (1910). Herdbestimmung bei Erdbeben aus den Ankunftszeiten. *Nachrichten von der Gesellschaft der Wissenschaften zu Göttingen, Mathematisch-Physikalische Klasse*, 1910:331–349.

Geller, R. J. and Mueller, C. S. (1980). Four similar earthquakes in central California. *Geophysical Research Letters*, 7(10):821–824.

Gentili, S. and Michelini, A. (2006). Automatic picking of P and S phases using a neural tree. *Journal of Seismology*, 10(1):39–63.

geox GmbH (2016). Sketch of Landau power plant facitily. `http://www.pfalzwerke.de/3901.php`. Accessed: 2017-05-10.

Gibbons, S. J. and Ringdal, F. (2006). The detection of low magnitude seismic events using array-based waveform correlation. *Geophysical Journal International*, 165(1):149–166.

Gibbons, S. J., Ringdal, F., and Kvaerna, T. (2012). Ratio-to-moving-average seismograms: a strategy for improving correlation detector performance. *Geophysical Journal International*, 190:511–521.

Goforth, T. and Herrin, E. (1981). An automatic seismic signal detection algorithm based on the Walsh transform. *Bulletin of the Seismological Society of America*, 71(4):1351–1360.

Gomberg, J. S., Shedlock, K. M., and Roecker, S. W. (1990). The effect of S-wave arrival times on the accuracy of hypocenter estimation. *Bulletin of the Seismological Society of America*, 80(6A):1605–1628.

Got, J.-L., Fréchet, J., and Klein, F. W. (1994). Deep fault plane geometry inferred from multiplet relative relocation beneath the south flank of Kilauea. *Journal of Geophysical Research: Solid Earth*, 99(B8):15375–15386.

Grand, S. P. (1990). A possible station bias in travel time measurements reported to ISC. *Geophysical Research Letters*, 17(1):17–20.

Grund, M., Groos, J. C., and Ritter, J. R. R. (2016). Fault Reactivation Analysis Using Microearthquake Clustering Based on Signal-to-Noise Weighted Waveform Similarity. *Pure and Applied Geophysics*, 173(7):2325–2355.

Grünthal, G. (2014). Induced seismicity related to geothermal projects versus natural tectonic earthquakes and other types of induced seismic events in Central Europe. *Geothermics*, 52:22–35.

Gudmundsson, O., Davies, J. H., and Clayton, R. W. (1990). Stochastic analysis of global traveltime data: mantle heterogeneity and random errors in the ISC data. *Geophysical Journal International*, 102(1):25–43.

Häring, M. O., Schanz, U., Ladner, F., and Dyer, B. C. (2008). Characterisation of the Basel 1 enhanced geothermal system. *Geothermics*, 37(5):469 – 495.

Harris, D. (1991). A waveform correlation method for identifying quarry explosions. *Bulletin of Seismological Society America*, 81(6):2395–2418.

Hauksson, E. and Shearer, P. (2005). Southern California Hypocenter Relocation with Waveform Cross-Correlation, Part 1: Results Using the Double-Difference Method. *Bulletin of the Seismological Society of America*, 95(3):896–903.

Hemmann, A., Meier, T., Jentzsch, G., and Ziegert, A. (2003). Similarity of waveforms and relative relocalisation of the earthquake swarm 1997/1998 near Werdau. *Journal of Geodynamics*, 35(1-2):191–208.

Homuth, B., Rümpker, G., Deckert, H., and Kracht, M. (2014). Seismicity of the northern Upper Rhine Graben - Constraints on the present-day stress field from focal mechanisms. *Tectonophysics*, 632:8 – 20.

Husen, S., Diehl, T., and Kissling, E. (2009). The effects of data quality in local earthquake tomography: Application to the Alpine region. *Geophysics*, 74(6):WCB71–WCB79.

Husen, S. and Hardebeck, J. (2010). Earthquake location accuracy. *CORSSA*.

Husen, S., Kissling, E., Flueh, E., and Asch, G. (1999). Accurate hypocentre determination in the seismogenic zone of the subducting Nazca Plate in northern Chile using a combined on-/offshore network. *Geophysical Journal International*, 138(3):687.

Illies, J. H. and Greiner, G. (1978). Rhinegraben and the Alpine system. *Geological Society of America Bulletin*, 89(5):770–782.

Illies, J. H. and Greiner, G. (1979). Holocene movements and state of stress in the rhinegraben rift system. *Tectonophysics*, 52(1):349 – 359.

International Seismological Centre (2009). *EHB Bulletin*. Internatl. Seismol. Cent., Thatcham, United Kingdom. http://www.isc.ac.uk.

International Seismological Centre (2016). *On-line Bulletin*. Internatl. Seismol. Cent., Thatcham, United Kingdom. http://www.isc.ac.uk.

Israelsson, H. (1990). Correlation of waveforms from closely spaced regional events. *Bulletin of Seismological Society America*, 80(6):2177–2193.

Ito, A. (1990). Earthquake swarm activity revealed from high-resolution relative hypocenters - clustering of microearthquakes. *Tectonophysics*, 175(1):47 – 66.

Jayaraman, T. and Kanitkar, T. (2016). The Paris Agreement. *Economic and Political Weekly*, 51(3).

Jeanne, P., Rutqvist, J., Dobson, P. F., Walters, M., Hartline, C., and Garcia, J. (2014). The impacts of mechanical stress transfers caused by hydromechanical and thermal processes on fault stability during hydraulic stimulation in a deep geothermal reservoir . *International Journal of Rock Mechanics and Mining Sciences*, 72:149 – 163.

Joswig, M. (1990). Pattern recognition for earthquake detection. *Bulletin of the Seismological Society of America*, 80(1):170–186.

Kennett, B. L. N., Engdahl, E. R., and Buland, R. (1995). Constraints on seismic velocities in the earth from traveltimes. *Geophysical Journal International*, 122(1):108–124.

Kind, R., Handy, M. R., Yuan, X., Meier, T., Kämpf, H., and Soomro, R. (2017). Detection of a new sub-lithospheric discontinuity in Central Europe with S-receiver functions . *Tectonophysics*, 700-701:19 – 31.

Király, E., Zechar, J. D., Gischig, V., Karvounis, D., Heiniger, L., and Wiemer, S. (2015). Modeling and forecasting induced seismicity in deep geothermal energy projects. In *Proceedings of the World Geothermal Congress*.

Kissling, E., Ellsworth, W. L., Eberhart-Phillips, D., and Kradolfer, U. (1994). Initial reference models in local earthquake tomography. *Journal of Geophysical Research: Solid Earth*, 99(B10):19635–19646.

Kisslinger, C. (1976). A review of theories of mechanisms of induced seismicity. *Engineering Geology*, 10(2-4):85–98.

Koulakov, I. and Sobolev, S. V. (2006). A tomographic image of Indian lithosphere break-off beneath the Pamir-Hindukush region. *Geophysical Journal International*, 164(2):425.

Kuochen, H., Wu, Y.-M., Chen, Y.-G., and Chen, R.-Y. (2007). 2003 Mw6.8 Chengkung earthquake and its related seismogenic structures . *Journal of Asian Earth Sciences*, 31(3):332 – 339.

Küperkoch, L., Meier, T., Brüstle, A., Lee, J., and Friederich, W. (2012). Automated determination of S-phase arrival times using autoregressive prediction: application to local and regional distances. *Geophysical Journal International*, 188(2):687–702.

Küperkoch, L., Meier, T., Lee, J., Friederich, W., and Working Group, E. (2010). Automated determination of P-phase arrival times at regional and local distances using higher order statistics. *Geophysical Journal International*.

Kurzon, I., Vernon, F. L., Rosenberger, A., and Ben-Zion, Y. (2014). Real-Time Automatic Detectors of P and S Waves Using Singular Value Decomposition. *Bulletin of the Seismological Society of America*, 104(4):1696–1708.

Lahr, J., Chouet, B., Stephens, C., Power, J., and Page, R. (1994). Earthquake classification, location, and error analysis in a volcanic environment: implications for the magmatic system of the 1989-1990 eruptions at redoubt volcano, Alaska. *Journal of Volcanology and Geothermal Research*, 62(1):137 – 151.

Lahr, J. C. (1999). *HYPOELLIPSE: A computer program for determining local earthquake hypocentral parameters, magnitude, and first motion pattern*. US Department of the Interior, US Geological Survey.

Larroque, J. and Laurent, P. (1988). Evolution of the stress field pattern in the south of the Rhine Graben from the Eocene to the present. *Tectonophysics*, 148(1):41 – 58.

Lashof, D. A. and Ahuja, D. R. (1990). Relative contributions of greenhouse gas emissions to global warming. *Nature*, 344(6266):529–531.

Lee, W., Bennett, R., and Meagher, L. (1972). A method for estimating magnitude of local earthquakes from signal duration. Open file report, US Geological Survey.

Leonard, M. and Kennett, B. L. N. (1999). Multi-component autoregressive techniques for the analysis of seismograms. *Physics of the Earth and Planetary Interiors*, 113(1-4):247–263.

Leydecker, G. (2011). Erdbebenkatalog für Deutschland mit Randgebieten für die Jahre 800 bis 2008.

Li, X., Shang, X., Morales-Esteban, A., and Wang, Z. (2017). Identifying P phase arrival of weak events: The Akaike Information Criterion picking application based on the Empirical Mode Decomposition. *Computers and Geosciences*, 100:57–66.

Li, Z. and Peng, Z. (2016). An Automatic Phase Picker for Local Earthquakes with Predetermined Locations: Combining a Signal-to-Noise Ratio Detector with 1D Velocity Model Inversion. *Seismological Research Letters*.

Liang, X., Chen, Y., Tian, X., Chen, Y. J., Ni, J., Gallegos, A., Klemperer, S. L., Wang, M., Xu, T., Sun, C., Si, S., Lan, H., and Teng, J. (2016). 3D imaging of subducting and fragmenting Indian continental lithosphere beneath southern and central Tibet using body-wave finite-frequency tomography . *Earth and Planetary Science Letters*, 443:162–175.

Lomax, A., Michelini, A., and Curtis, A. (2009). *Earthquake Location, Direct, Global-Search Methods*, pages 1–33. Springer New York, New York, NY.

Lomax, A., Virieux, J., Volant, P., and Berge-Thierry, C. (2000). *Probabilistic Earthquake Location in 3D and Layered Models*, pages 101–134. Springer Netherlands, Dordrecht.

Maeda, N. (1985). A Method for Reading and Checking Phase Time in Auto-Processing System of Seismic Wave Data. *Zisin (Journal of the Seismological Society of Japan. 2nd ser.)*, 38(3):365–379.

Majer, E. L., Baria, R., Stark, M., Oates, S., Bommer, J., Smith, B., and Asanuma, H. (2007). Induced seismicity associated with Enhanced Geothermal Systems. *Geothermics*, 36(3):185–222.

Majer, E. L. and Peterson, J. E. (2007). The impact of injection on seismicity at The Geysers, California Geothermal Field. *International Journal of Rock Mechanics and Mining Sciences*, 44(8):1079 – 1090.

Matthews, H. D., Gillett, N. P., Stott, P. A., and Zickfeld, K. (2009). The proportionality of global warming to cumulative carbon emissions. *Nature*, 459(7248):829–832.

Maurer, H. and Deichmann, N. (1995). Microearthquake cluster detection based on waveform similarities, with an application to the western Swiss Alps. *Geophysical Journal International*, 123(2):588–600.

McClure, M. W. (2012). *Modeling and Characterization of Hydraulic Stimulation and Induced Seismicity in Geothermal and Shale Gas Reservoirs*. Phd-thesis, Stanford.

McCrory, P. A., Blair, J. L., Waldhauser, F., and Oppenheimer, D. H. (2012). Juan de Fuca slab geometry and its relation to Wadati-Benioff zone seismicity. *Journal of Geophysical Research: Solid Earth*, 117(B9).

Moeck, I., Kwiatek, G., and Zimmermann, G. (2009). Slip tendency analysis, fault reactivation potential and induced seismicity in a deep geothermal reservoir. *Journal of Structural Geology*, 31(10):1174–1182.

Nakahara, H. (2004). Correlation distance of waveforms for closely located events - I. Implication of the heterogeneous structure around the source region of the 1995 Hyogo-Ken Nanbu, Japan, earthquake (Mw=6.9). *Geophysical Journal International*, 157(3):1255–1268.

Nolet, G. (1987). *Seismic wave propagation and seismic tomography*, pages 1–23. Springer Netherlands, Dordrecht.

Paige, C. C. and Saunders, M. A. (1982). Algorithm 583: LSQR: Sparse Linear Equations and Least Squares Problems. *ACM Trans. Math. Softw.*, 8(2):195–209.

Pavlis, G. L. (1992). Appraising relative earthquake location errors. *Bulletin of the Seismological Society of America*, 82(2):836–859.

Pavlis, G. L. and Booker, J. R. (1980). The mixed discrete-continuous inverse problem: Application to the simultaneous determination of earthquake hypocenters and velocity structure. *Journal of Geophysical Research: Solid Earth*, 85(B9):4801–4810.

Peters, G. and van Balen, R. T. (2007). Tectonic geomorphology of the northern Upper Rhine Graben, Germany . *Global and Planetary Change*, 58(1-4):310 – 334.

Podvin, P. and Lecomte, I. (1991). Finite difference computation of traveltimes in very contrasted velocity models: a massively parallel approach and its associated tools. *Geophysical Journal International*, 105(1):271–284.

Prodehl, C., Mueller, S., Glahn, A., Gutscher, M., and Haak, V. (1992). Lithospheric cross sections of the European Cenozoic rift system. *Tectonophysics*, 208(1):113 – 138.

Rawles, C. and Thurber, C. (2015). A non-parametric method for automatic determination ofP-wave andS-wave arrival times: application to local micro earthquakes. *Geophysical Journal International*, 202(2):1164–1179.

Röhm, A. H. E., Bijwaard, H., Spakman, W., and Trampert, J. (2000). Effects of arrival time errors on traveltime tomography. *Geophysical Journal International*, 142(1):270–276.

Röhm, A. H. E., Trampert, J., Paulssen, H., and Snieder, R. K. (1999). Bias in reported seismic arrival times deduced from the ISC Bulletin. *Geophysical Journal International*, 137(1):163–174.

Rutqvist, J., Dobson, P. F., Garcia, J., Hartline, C., Jeanne, P., Oldenburg, C. M., Vasco, D. W., and Walters, M. (2015a). The Northwest Geysers EGS Demonstration Project, California: Pre-stimulation Modeling and Interpretation of the Stimulation. *Mathematical Geosciences*, 47(1):3–29.

Rutqvist, J., Rinaldi, A. P., Cappa, F., and Moridis, G. J. (2015b). Modeling of fault activation and seismicity by injection directly into a fault zone associated with hydraulic fracturing of shale-gas reservoirs. *Journal of Petroleum Science and Engineering*, 127:377 – 386.

Rybach, L. (2003). Geothermal energy: sustainability and the environment. *Geothermics*, 32(4-6):463 – 470. Selected Papers from the European Geothermal Conference 2003.

Sabbione, J. I. and Velis, D. R. (2013). A robust method for microseismic event detection based on automatic phase pickers. *Journal of Applied Geophysics*, 99:42–50.

Saragiotis, C. D., Hadjileontiadis, L. J., and Panas, S. M. (2002). PAI-S/K: A robust automatic seismic P phase arrival identification scheme. *IEEE Transactions on Geoscience and Remote Sensing*, 40(6):1395–1404.

Scafidi, D., Spallarossa, D., Turino, C., Ferretti, G., and A., V. (2016). Automatic P- and S-Wave Local Earthquake Tomography: Testing Performance of the Automatic Phase-Picker Engine "RSNI-Picker". *Bulletin of the Seismological Society of America*, 106(2):526–536.

Scholz, C. H. (1998). Earthquakes and friction laws. *Nature*, 391:37 – 42.

Schumacher, M. E. (2002). Upper Rhine Graben: Role of preexisting structures during rift evolution. *Tectonics*, 21(1):6–1–6–17.

Schweitzer, J. (1997). HYPOSAT - A new routine to locate seismic events. *NORSAR Scientific Report*, 1(98):94–102.

Schweitzer, J. (2001). HYPOSAT - An Enhanced Routine to Locate Seismic Events. *pure and applied geophysics*, 158(1):277–289.

Segall, P. and Fitzgerald, S. D. (1998). A note on induced stress changes in hydrocarbon and geothermal reservoirs. *Tectonophysics*, 289(1-3):117 – 128.

Shearer, P. M. (1997). Improving local earthquake locations using the L1 norm and waveform cross correlation: Application to the Whittier Narrows, California, aftershock sequence. *Journal of Geophysical Research: Solid Earth*, 102(B4):8269–8283.

Shen, Y. (2006). Finite-frequency seismic tomography. *The Journal of the Acoustical Society of America*, 119(5):3307–3308.

Sleeman, R. and van Eck, T. (1999). Robust automatic P-phase picking: an on-line implementation in the analysis of broadband seismogram recordings. *Physics of the Earth and Planetary Interiors*, 113(1-4):265–275.

Soldati, G., Boschi, L., Mora, S. D., and Forte, A. (2015). Tomography of core-mantle boundary and lowermost mantle coupled by geodynamics: joint models of shear and compressional velocity. *Annals of Geophysics*, 57(6).

Spallarossa, D., Ferretti, G., Scafidi, D., Turino, C., and Pasta, M. (2014). Performance of the RSNI-Picker. *Seismological Research Letters*, 85(6):1243–1254.

Stewart, S. W. (1977). Real-time detection and location of local seismic events in central California. *Bulletin of the Seismological Society of America*, 67(2):433–452.

Suchi, E., Dittmann, J., Knopf, S., Mueller, C., and Schulz, R. (2014). Geothermal-Atlas to Visualise potential Conflicts of Interest between CO2-Storage (CCS) and Deep Geothermal Energy in Germany. *Zeitschrift der Deutschen Gesellschaft für Geowissenschaften*, 165(3):439–453.

Takanami, T. and Kitagawa, G. (1988). A new efficient procedure for the estimation of onset times of seismic waves. *Journal of Physics of the Earth*, 36(6):267–290.

Tarantola, A. and Valette, B. (1982). Inverse problems = quest for information. *J. Geophys.*, 50:159–170.

The ObsPy Development Team (2016). ObsPy 1.0.1.

Thurber, C., Zhang, H., Waldhauser, F., Hardebeck, J., Michael, A., and Eberhart-Phillips, D. (2006). Three-Dimensional Compressional Wavespeed Model, Earthquake Relocations, and Focal Mechanisms for the Parkfield, California, Region. *Bulletin of the Seismological Society of America*, 96(4B):S38–S49.

Turino, C., Morasca, P., Ferretti, G., Scafidi, D., and Spallarossa, D. (2010). Reliability of the automatic procedures for locating earthquakes in southwestern Alps and northern Apennines (Italy). *Journal of Seismology*, 14(2):393 – 411.

VanDecar, J. C. and Crosson, R. S. (1990). Determination of teleseismic relative phase arrival times using multi-channel cross-correlation and least squares. *Bulletin of the Seismological Society of America*, 80(1):150–169.

Vasterling, M., Wegler, U., Becker, J., Brüstle, A., and Bischoff, M. (2016). Real-time envelope cross-correlation detector: application to induced seismicity in the Insheim and Landau deep geothermal reservoirs. *Journal of Seismology*, pages 1–16.

Villemin, T., Alvarez, F., and Angelier, J. (1986). The Rhinegraben: Extension, subsidence and shoulder uplift. *Tectonophysics*, 128(1):47 – 59.

Waldhauser, F. and Ellsworth, W. (2000). A double-difference earthquake location algorithm: Method and application to the Northern Hayward Fault, California. *Bulletin of Seismological Society America*, 90(6):1353–1368.

Waldhauser, F., Schaff, D., Richards, P. G., and Kim, W.-Y. (2004). Lop Nor Revisited: Underground Nuclear Explosion Locations, 1976-1996, from Double-Difference Analysis of Regional and Teleseismic Data. *Bulletin of the Seismological Society of America*, 94(5):1879–1889.

Wang, W., Wu, J., Fang, L., and Wang, C. (2013). Relocation of the Yushu M S 7.1 earthquake and its aftershocks in 2010 from HypoDD. *Science China Earth Sciences*, pages 1–10.

Wassing, B., van Wees, J., and Fokker, P. (2014). Coupled continuum modeling of fracture reactivation and induced seismicity during enhanced geothermal operations. *Geothermics*, 52:153 – 164. Analysis of Induced Seismicity in Geothermal Operations.

Weber, J., Ganz, B., Schellschmidt, R., Sanner, B., and Schulz, R. (2015). Geothermal energy use in Germany. In *Proceedings of the World Geothermal Congress*.

Wehling-Benatelli, S., Becker, D., Bischoff, M., Friederich, W., and Meier, T. (2013). Indications for differ-ent types of brittle failure due to active coal mining using waveform similarities of induced seismic events. *Solid Earth*, 4(1):405–422.

Zang, A., Oye, V., Jousset, P., Deichmann, N., Gritto, R., McGarr, A., Majer, E., and Bruhn, D. (2014). Analysis of induced seismicity in geothermal reservoirs - An overview. *Geothermics*, 52:6–21.

Zhang, H., Thurber, C., and Rowe, C. (2003). Automatic P-Wave Arrival Detection and Picking with Multiscale Wavelet Analysis for Single-Component Recordings. *Bulletin of the Seismological Society of America*, 93(5):1904–1912.

Zhang, H., van der Lee, S., Wolin, E., Bollmann, T. A., Revenaugh, J., Wiens, D. A., Frederiksen, A. W., Darbyshire, F. A., Aleqabi, G. I., Wysession, M. E., Stein, S., and Jurdy, D. M. (2016). Distinct crustal structure of the North American Midcontinent Rift from P wave receiver functions. *Journal of Geophysical Research: Solid Earth*, 121(11):8136–8153. 2016JB013244.

Zhang, Haijiang and Thurber, Clifford H. (2003). Double-difference tomography: The method and its application to the hayward fault, california. *Bulletin of the Seismological Society of America*, 93(5):1875–1889.

Ziegler, P. and Dèzes, P. (2006). Crustal evolution of western and central Europe.

Ziegler, P. A. (1992). European Cenozoic rift system. *Tectonophysics*, 208(1):91 – 111.
References

A. Master events for similarity detection

Cluster No.	Source time	Latitude	Longitude	Depth	Ml
1	02.04.2012 07:38:14	49.2038°	8.1160°	4.09	1.8
2	29.09.2011 17:55:21	49.1972°	8.1170°	3.83	2.1
3	25.06.2012 22:11:54	49.1996°	8.1136°	5.28	1.6
4	25.06.2012 21:42:57	49.1930°	8.1128°	4.74	1.5
5	30.10.2010 13:44:08	49.1830°	8.1049°	4.23	1.8
6	04.10.2011 15:05:12	49.1940°	8.1182°	3.96	2.4
7	25.03.2012 16:47:47	49.2014°	8.1161°	4.12	1.6
8	20.11.2011 20:08:37	49.2016°	8.1104°	4.31	1.3
9	21.11.2011 04:48:19	49.2097°	8.0986°	4.09	2.6
10	10.07.2011 20:18:53	49.1973°	8.1158°	3.37	2.1
11	14.03.2010 11:13:48	49.1966°	8.1162°	3.78	2.0
12	15.12.2010 19:33:41	49.1960°	8.1208°	3.87	1.8

Table A.02.: Properties of induced events selected as master events for the Landau reservoir taken from the Bestec catalog (Bestec GmbH). (*) Depths are fixed for location.

Cluster No.	Source time	Latitude	Longitude	Depth	Ml
1	23.11.2013 05:19:32	49.1780°	8.1718°	3.8(*)	1.2
2	11.11.2012 12:58:42	49.0988°	8.1763°	3.8(*)	1.2
3	02.10.2013 01:47:30	49.1622°	8.1572°	3.8(*)	1.4
4	06.08.2013 07:54:09	49.1444°	8.1648°	3.8(*)	1.6
5	08.11.2012 14:51:03	49.1514°	8.1533°	5.2	1.5
6	16.01.2013 08:44:13	49.1446°	8.1572°	5.3	1.3
7	09.12.2012 11:41:46	49.1565°	8.1416°	5.9	1
8	31.10.2012 21:43:25	49.1551°	8.1399°	4.8	1
9	09.11.2013 20:00:27	49.1550°	8.1565°	4.7	0,7
10	04.06.2013 10:15:40	49.1455°	8.1598°	4.1	0.6
11	07.10.2015 13:42:47	49.1466°	8.1557°	5.3	2.1
12	20.05.2015 18:52:17	49.1497°	8.1585°	5.4	1.8
13	03.10.2015 09:27:43	49.1507°	8.1577°	5.5	1.5
14	16.09.2015 13:07:51	49.1493°	8.1533°	5.4	1.5
15	05.09.2015 11:14:26	49.1488°	8.1557°	5.1	1.3
16	11.09.2015 05:12:53	49.1479°	8.1600°	5.7	1.2
17	15.06.2015 18:45:20	49.1502°	8.1577°	5.2	1.2
18	28.03.2015 04:40:49	49.1521°	8.1534°	5.3	1.2
19	17.01.2015 20:09:16	49.1508°	8.1550°	4.2	1.2
20	24.09.2014 08:05:12	49.1501°	8.1546°	5.2	1.1

Table A.01.: Properties of induced events selected as master events for the Insheim reservoir taken from the Bestec catalog (Bestec GmbH). (*) Depths are fixed for location.

B. Cost function parameter optimization

Cost function optimization for P1-phase picking

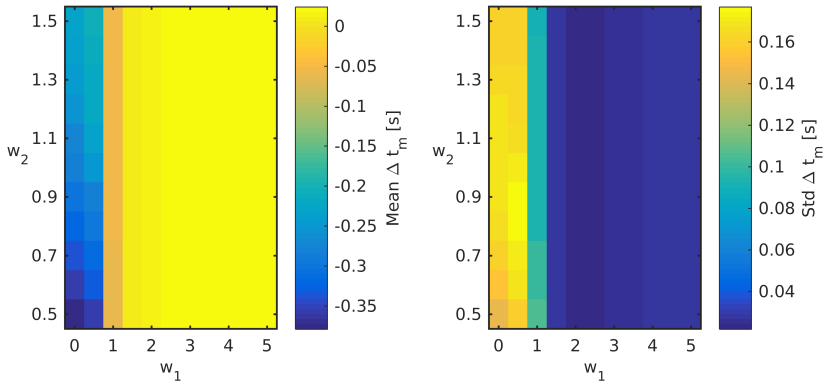

Figure B.01.: Mean and standard deviation of residuals between automatic and manual induced P1-phase arrival times for different cost function weightings w_1 and w_2, $w_3 = 0$. Considered are only good quality automatic P1-phase picks ($Q > 2.5$).

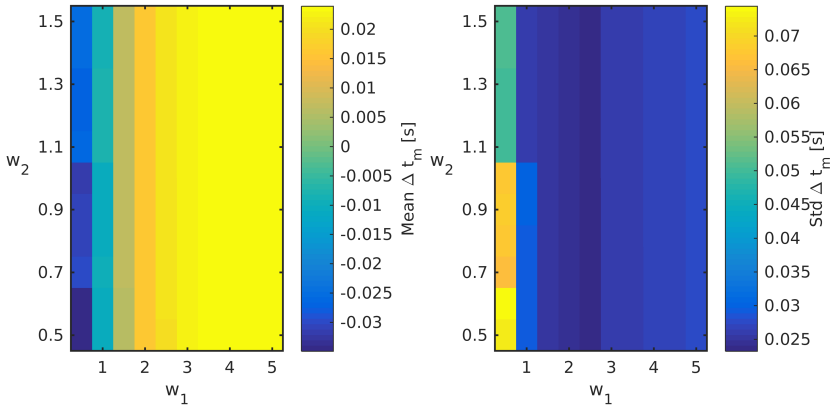

Figure B.02.: Mean and standard deviation of residuals between automatic and manual induced P1-phase arrival times for different cost function weightings w_1 and w_2, $w_3 = 1$. Considered are only good quality automatic P1-phase picks ($Q > 2.5$).

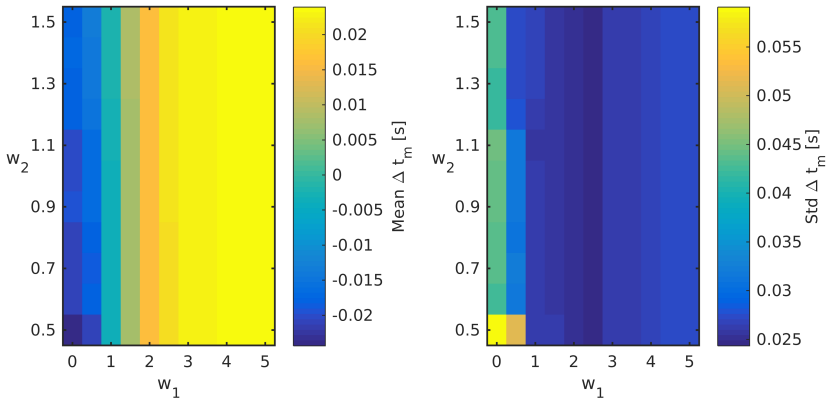

Figure B.03.: Mean and standard deviation of residuals between automatic and manual induced P1-phase arrival times for different cost function weightings w_1 and w_2, $w_3 = 1.5$. Considered are only good quality automatic P1-phase picks ($Q > 2.5$).

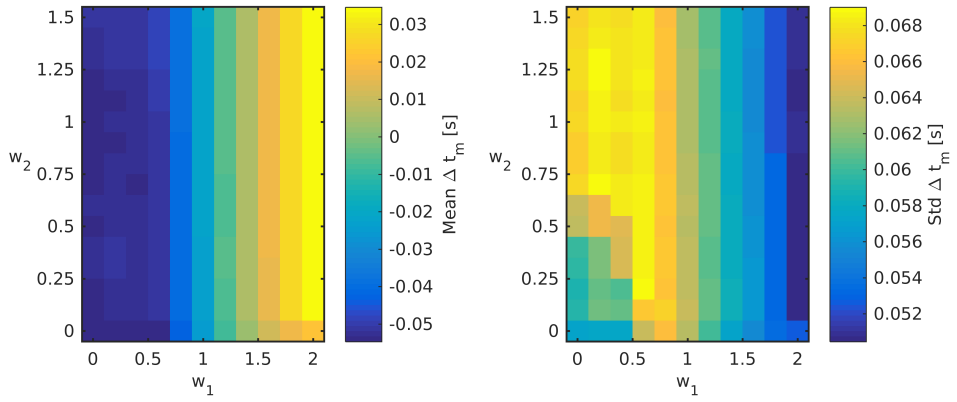

Figure B.04.: Mean and standard deviation of residuals between automatic and manual induced S1-phase arrival times for different cost function weightings w_1 and w_2, $w_3 = 0.5$. Considered are only good quality automatic S1-phase picks ($Q > 2.5$).

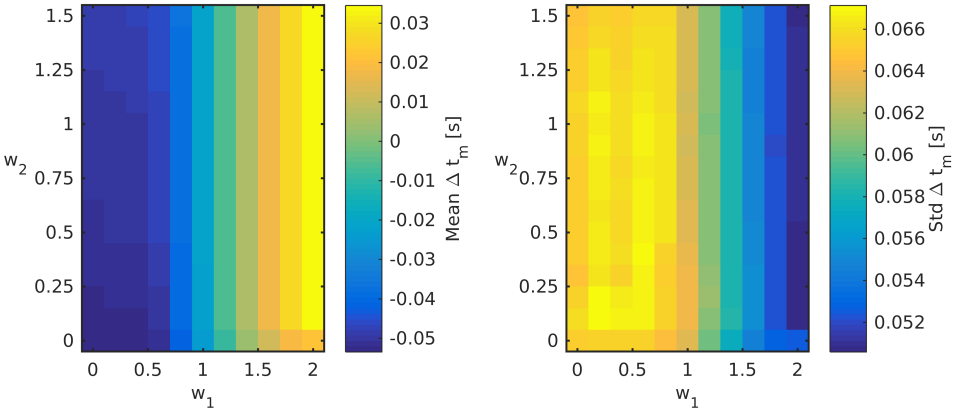

Figure B.05.: Mean and standard deviation of residuals between automatic and manual induced S1-phase arrival times for different cost function weightings w_1 and w_2, $w_3 = 1$. Considered are only good quality automatic S1-phase picks ($Q > 2.5$).

C. List of seismic stations

Network Code	Station Code	Latitude	Longitude	Elevation
GR	LDAU	49.1820° N	8.1270° E	151m
GR	INS1	49.1482° N	8.0463° E	196m
GR	INS2	49.1201° N	8.1337° E	135m
GR	INS3	49.0966° N	8.0821° E	141m
GR	INS4	49.1946° N	8.1109° E	148m
GR	IN4B	49.1928° N	8.1115° E	149m
GR	INS5	49.1290° N	8.2034° E	129m
GR	INS6	49.0869° N	8.1932° E	130m
GR	IN6B	49.0852° N	8.1939° E	134m
GR	INS7	49.1599° N	8.2122° E	155m
GR	INS8	49.2628° N	8.1251° E	162m
GR*	TMO20	49.1843° N	8.0551° E	208m
GR*	TMO22	49.2192° N	8.1847° E	135m
GR*	TMO50	49.1822° N	8.1268° E	155m
GR*	TMO51	49.1543° N	8.1851° E	134m
GR*	TMO52	49.1292° N	8.1847° E	130m
GR*	TMO53	49.1663° N	8.1197° E	173m
GR*	TMO54	49.1396° N	8.1286° E	139m
GR*	TMO55	49.2276° N	8.1099° E	197m
GR*	TMO57	49.1734° N	8.2772° E	137m
GR*	TMO58	49.1867° N	8.1922° E	134m
GR*	TMO59	49.1391° N	8.2195° E	109m
GR*	TMO61	49.1900° N	8.1279° E	110m
GR*	TMO65	49.1967° N	7.9781° E	482m
GR*	TMO66	49.2177° N	8.0460° E	194m

Table C.01.: Seismic stations installed by the Federeal Agency for Geosciences and Resources (BGR) in the surrounding of the Landau and Insheim geothermal reservoirs. (*) indicates that these stations were originally part of the Karlsruhe Institute of Technology (KIT) network.

Network Code	Station Code	Latitude	Longitude	Elevation
LED	INSH	49.1472° N	8.1660° E	130m
LED	ROTT	49.1290° N	8.1490° E	-177m

Table C.02.: Seismic stations operated by the State Monitoring Agency Rheinland-Pfalz in the surrounding of the Landau and Insheim geothermal reservoirs.

Network Code	Station Code	Latitude	Longitude	Elevation
LD	SOS2	49.1944° N	8.0784° E	175m
LD	NOS2	49.1943° N	8.0784° E	175m
LD	SOS3	49.2143° N	8.0984° E	185m
LD	SOS5	49.1901° N	8.1717° E	134m
LD	SOS6	49.1532° N	8.1454° E	145m
LD	SOS7	49.1346° N	8.1772° E	128m
LD	SOS8	49.1603° N	8.1779° E	151m
LD	SOS9	49.1430° N	8.1172° E	144m
LD	STS1	49.1717° N	8.0877° E	-114m
LD	STS4	49.2224° N	8.1478° E	-85m

Table C.03.: Seismic stations installed by the company Bestec GmbH in the surrounding of the Landau and Insheim geothermal reservoirs.

Network Code	Station Code	Latitude	Longitude	Elevation
DMT	AH11	49.1494° N	8.2029° E	145m
DMT	AWL	49.1385° N	8.1940°	121m
DMT	BG15	49.1572° N	8.1414° E	144m
DMT	BH30	49.1383° N	8.1360° E	137m
DMT	BH38	49.1574° N	8.1515° E	147m
DMT	BS4	49.1912° N	8.0929° E	170m
DMT	GHS94	49.2104° N	8.0779° E	152m
DMT	HS5	49.1376° N	8.1256° E	136m
DMT	IVS74	49.1989° N	8.1353° E	139m
DMT	LS9A	49.1986° N	8.1101° E	143m
DMT	OVMS2	49.2111° N	8.1221° E	146m
DMT	SS71	49.2007° N	8.1301° E	143m
DMT	SW27	49.1556° N	8.1478° E	138m
DMT	WHS5	49.1906° N	8.1293° E	142m

Table C.04.: Seismic stations operated by the German Montantechnology (DMT) in the surrounding of the Landau and Insheim geothermal reservoirs.

Erklärung

Hiermit erkläre ich an Eides statt, dass ich die vorliegende Dissertation - abgesehen von der Beratung durch meinen Betreuer Prof. Dr. Thomas Meier - selbstständig und ohne fremde Hilfe angefertigt, keine anderen als die angegebenen Quellen und Hilfsmittel benutzt und die den benutzten Quellen wörtlich oder inhaltlich entnommenen Stellen als solche kenntlich gemacht habe. Diese Arbeit hat in gleicher oder ähnlicher Form noch keiner Prüfungsbehörde vorgelegen. Sie ist unter Einhaltung der Regeln guter wissenschaftlicher Praxis der Deutschen Forschungsgemeinschaft entstanden.

Kiel, 13. Juli 2017

(Kai Friedrich Martin Olbert)